ProQuest Number: 10183199

ProQuest.

ProQuest 10183199

ProQuest LLC.
789 East Eisenhower Parkway
P.O. Box 1346
Ann Arbor, MI 48106 – 1346

LAYER GUIDED SHEAR ACOUSTIC WAVE SENSORS

FABRICE MARTIN

A thesis submitted in partial fulfilment of the requirements of the
Nottingham Trent University
for the degree of Doctor of Philosophy.

November 2002

ABSTRACT

Acoustic wave micro-sensors with pure or dominant shear horizontal polarisation, employed for liquid operations with Love mode devices, are amongst the most promising because they have the highest sensitivity among all known acoustic sensors. In this thesis a model is presented for the mass sensitivity of Love waves on a finite thickness substrate. It is shown that the model includes shear horizontal acoustic plate modes (SH-APM). A relationship is derived between the slope of the dispersion curve and the mass sensitivity. A new type of sensor, a layer guided SH-APM, is proposed and it is shown that significant enhancement of mass sensitivity, compared to a SH-APM, occurs. In addition, the peak mass sensitivity for Love waves on a semi-infinite substrate is shown to scale directly with frequency provided no mode change occurs. Optimisation of guiding layer thickness corresponds to strong dispersion so phase and group velocities can be quite different. A formula relating the difference in group and phase velocities to the mass sensitivity has been derived and can be extended to a wide range of other acoustic wave sensors.

In the work of this thesis Love wave devices have been optimised in terms of mass sensitivity by increasing the wave-guide layer. A polymer wave-guide was created with increasing thickness and higher order modes have been identified. Elastic, visco-elastic and liquid sensing operation at the first, second and third Love wave modes were achieved. Higher order modes were shown to exhibit substantial sensitivity in insertion loss to mass loading. A novel interrogation system based on a pulsed signal technique has been developed to investigate solid-liquid interactions or mass deposition at the interface of a surface acoustic wave sensor. The technique provided essential sensor parameters such as attenuation, phase change and time delay with the advantage of reflection peaks and acoustic modes discrimination, fast response and high sensitivity. The system was successfully operated for the

detection of biological agents in liquid and directly compared to a continuous wave system employing a network analyser. Insertion loss sensitivity to the deposition of evaporated metals, spin-coated polymer and liquid sensing has been directly investigated for the first, second and third Love modes. In analogy to the phase velocity mass sensitivity, the sensitivity in insertion loss to mass deposition has been related to the slope of the insertion loss curve with normalised guiding layer thickness. Phase velocity liquid loading sensitivity by phase measurements was also investigated for the first, second and third Love mode. It has been shown that higher order Love wave modes exhibit substantial sensitivity to mass loading by insertion loss and phase measurements. The effect of dispersion on Love wave sensors has been considered experimentally. Measurements of phase and group velocities, and insertion loss were obtained by systematically increasing the guiding layer thickness and by liquid phase sensing experiments using solutions of poly(ethylene glycol) of varying molecular weight and concentrations. The increase in sensitivity with guiding layer thickness is significant and the data confirms the theoretical prediction that group velocity is a more sensitive parameter than the phase velocity to visco-elastic and liquid loading.

"The process of scientific discovery is, in effect, a continual flight from wonder".

ALBERT EINSTEIN (1879-1955)

"If I have been able to see further, it was only because I stood on the shoulders of giants".

SIR ISAAC NEWTON (1643-1727)

"Science sans conscience n'est que ruine de l'âme".

RABELAIS (1494-1553)

ACKNOWLEDGEMENTS

TABLE OF CONTENTS

CHAPTER 3 EXPERIMENTAL DEVELOPMENTS   3.1

CHAPTER 4 LOVE WAVE MASS SENSITIVITY   4.1

CHAPTER 1

INTRODUCTION

CHAPTER 1

INTRODUCTION

1.1 Introduction

Research on surface acoustic wave (SAW) devices began just over 30 years ago. The growth of interest in the subject has been enormous with a large number of publications and an extensive range of topics and devices studied. Starting from basic physical phenomena and principles, the subject has developed to a point where many sophisticated devices are available. Current devices, operating at frequencies in the range 10 MHz-1GHz, are designed using mathematical models implemented by computer-aided design, enabling custom specifications to be met with impressive accuracy. SAW delay lines, band-pass filters, matched filters and oscillators are making a significant impact on various electronic systems, particularly radar and spread-spectrum communications.

The subject can be said to originate in the 19th century, when Lord Rayleigh discovered the existence of an acoustic wave tightly bound to the free surface of a solid medium [1]. This wave, known as Rayleigh wave, is of importance in seismology and non-destructive testing. The more recent interest in electronic devices coincides with the advent of the interdigital transducer (IDT) [2] for efficient generation and reception of the wave. The transducer, implemented on piezoelectric materials with low propagation loss, enables device insertion loss to be low enough for system requirements up to 1 GHz. A basic attraction is the accessibility of the surface, which enables the wave to be tapped and sampled whilst it is propagating. The substrate used is normally crystalline as well as piezoelectric, and much recent research has clarified the nature of SAWs in such materials.

The most basic interdigital device is a delay line, consisting of two IDTs on a piezoelectric substrate (Fig. 1.1). Band-pass filters, dispersive non-compression filters, and tapped delay-lines are all based on the same principle, but with more sophisticated transducers.

input   output
transducer   transducer

Surface wave

absorber   piezoelectric substrate
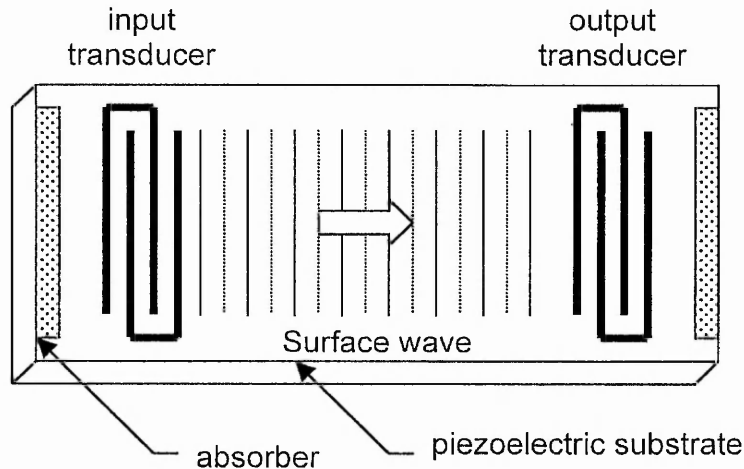
Fig. 1.1   Schematic representation of a surface acoustic wave

Surface wave waveguides have been extensively studied for the last twenty years. Guiding is obtained by locally reducing the SAW velocity by trapping the transmitted surface wave by either mechanical or electrical loading. Geometrical effects are also used in the topography of the waveguides. A related topic is the dispersion due to the deposited film mechanically loading the surface. Initially used for pulse compression filters, so called Love wave devices are now being used for bio (chemical) sensing.

Most current applications of SAWs still concern interdigital devices, though other devices, particularly the reflective array compressor, are also in systems. In this context, the development of planar processing techniques for the manufacture of integrated circuits has also contributed to the present interest in surface waves, since those developments permit the fabrication of transducers, waveguiding structures, and other elements to study, control, and utilize surface elastic waves. The economics of fabrication is naturally important. Interdigital devices are made by photo-etching a deposited metal

film, using a photomask to define the required pattern or by lifting off evaporated metals on top of photo-resolved images. Thus it is possible commercially to fabricate complex surface wave devices for operating frequencies up to 100 GHz.

Applications of surface waves can be divided into three main categories: studies of surface properties, signal generation and bio (chemical) sensing. For many years, surface waves have been studied by geologists in modelling and by engineers in the inspection of the surfaces of manufactured objects. Ultrasonic studies of a surface yields information about velocity and attenuation and hence, dynamic elastic moduli, impedance mismatch and surface roughness. Surface waves are also employed to measure film thickness and density. Determination of the condition of stresses in films and detection of the absorption of foreign materials at a surface have also been recently achieved by using surface waves. Many active and passive devices employing surface waves in signal generation and processing have been reported, as have applications involving optical interactions with surface waves, narrow bandpass filtering, correlation, frequency-modulated signal for pulse-compression radars, high density storage, hybrid couplers, gyrators and couplers.

The first reported use of a surface wave device as a selective analytical device concerned an application as a chromatographic detector [3]. In the early 1980's, SAW devices were able to achieve operations in liquids and were subsequently employed as biosensors in the liquid phase and as chemical sensors in the gas phase [4-7]. Waveguided SAWs obtained by using a dielectric over-layer have attracted much attention in recent years. Love wave sensors have been shown to exhibit one of the highest sensitivities [8] and have been used for a number of applications, including the detection of biological analytes in direct or competitive immuno-sensors [9-15] and in the gas phase [16-20].

1.2 History of SAWs

Surface acoustic wave devices are recognized for their versatility and efficiency in controlling and processing electrical signals. This has resulted in a multitude of device concepts for a wide range of signal processing functions, such as delay lines, filters, resonators, pulse compressors, convolvers, and many more. As SAW technology has found its way into mass market products such as TV receivers, pagers, keyless entry systems and cellular phones, the production volume has risen to millions of devices produced every day. At the other end of the scale, there are specialized high performance signal processing SAW devices for satellite communication and military applications, such as radar and electronic warfare.

1.2.1 Rayleigh waves

Surface acoustic waves were quantitatively described by Lord Rayleigh in 1885 when he showed theoretically that waves can be propagated over the plane boundary between an elastic half-space and a vacuum, or a sufficiently rarefied medium (eg. air), where the amplitude of the waves decay rapidly with depth. These waves are mechanical (acoustic) rather than electromagnetic. Much of an earthquake's destructive force is carried by this type of wave. Surface waves achieved little recognition for their application in r.f communications until just over three decades ago when SAW devices began to be developed for spread spectrum use in military radar equipment. From these beginnings an exciting new technology has evolved for r.f signal processing applications. In its simplest form, a SAW transducer consists of two interdigital arrays of thin metal electrodes deposited on a highly polished piezoelectric substrate such as quartz. In a simple IDT, the electrodes that comprise these arrays alternate polarities so that an r.f signal of the proper frequency applied across them causes strain in the surface of the crystal. This generates the Rayleigh wave, or surface wave, as it is more commonly called. These interdigital electrodes are generally

spaced at 1/4 wavelength of the operating centre frequency. Since the surface wave or acoustic velocity is 10^{-5} of the speed of light, an acoustic wavelength is much smaller than its electromagnetic counterpart. For example, a continuous wave (CW) signal at 100 MHz with a free space wavelength of three metres would have a corresponding acoustic wavelength of about 30 microns. This results in the SAW's unique ability to incorporate an incredible amount of signal processing or delay in a very small volume. As a result of this relationship, physical limitations exist at higher frequencies when the electrodes become too narrow to fabricate with standard photolithographic techniques and at lower frequencies when the devices become impractically large. Hence, at this time, SAW devices are most typically used from 10 MHz to about 3 GHz.

1.2.2 Piezoelectric effect

The piezoelectric effect was discovered by Pierre and Jacques Curie in 1880. It remained a mere curiosity until the 1940s. The property of certain crystals to exhibit electrical charges under mechanical loading was of no practical use until very high input impedance amplifiers enabled engineers to amplify their signals. In the 1950s, electrometer tubes of sufficient quality became available and the piezoelectric effect was commercialised. The charge amplifier principle was patented by W.P. Kistler in 1950 and gained practical significance in the 1960s. The introduction of MOSFET solid state circuitry and the development of highly insulating materials such as Teflon and Kapton greatly improved performance and propelled the use of piezoelectric sensors into virtually all areas of modern technology and industry. Piezoelectric measuring systems are active electrical systems. That is, the crystals produce an electrical output only when they experience a change in load. For this reason, they cannot perform true static measurements. However, it is a misconception that piezoelectric instruments are suitable for only dynamic measurements. Quartz transducers, paired with adequate signal conditioners, offer excellent quasistatic measuring capability. There are countless examples of applications where quartz based

transducers accurately and reliably measure quasistatic phenomena for minutes and even hours. Piezoelectric measuring devices are widely used today in the laboratory, on the production floor and as original equipment. They are used in almost every conceivable application requiring accurate measurement and recording of dynamic changes in mechanical variables such as pressure, force and acceleration.

1.2.3 Piezoelectric substrates

Among the piezoelectic substrate materials that can be used for acoustic wave sensors and devices, the most common are quartz (SiO_2), lithium tantalate ($LiTaO_3$), and, to a lesser degree, lithium niobate ($LiNbO_3$). Each has specific advantages and disadvantages, which include cost, temperature dependence, attenuation, and propagation velocity. Table 1.1 lists some relevant specifications for each material, including the most popular cuts and orientations [55]. An interesting property of quartz is that it is possible to select the temperature dependence of the material by the cut angle and the wave propagation direction. With proper selection, the first order temperature effect can be minimized. An acoustic wave temperature sensor may be designed by maximizing this effect. This is not true of lithium niobate or lithium tantalate, where a linear temperature dependence always exists for all material cuts and propagation directions. Other materials are used commercially include gallium arsenide (GaAs), silicon carbide (SiC), langasite (LGS), zinc oxide (ZnO), aluminum nitride (AlN), lead zirconium titanate (PZT), and polyvinylidene fluoride (PVdF).

1.2.4 Interdigital transducers (IDTs)

Surface acoustic waves can be generated by many ingenious ways, but the IDT has proved to be ideally adapted to SAW device and signal processing applications. The principle of two neighbouring electrodes (finger pairs) of an IDT is derived simply from the BAW thickness mode resonance configuration. For the SAW device, the electrodes are now two metallic strips

positioned on the surface of a piezoelectric substrate separated by a distance l and so creating an electric field in the surface region. A surface acoustic wave is then generated by the piezoelectric effect. For a single pair the Q is small, and the response is broadband. The resonance can be sharpened by adding many finger pairs in interdigital fashion with alternating polarity. If the frequency is off resonance then the different contributions are no longer in phase and the response is small. Thus, with many finger pairs, the resonance is sharp and the Q is high.

Substrate	Cut	Propagation	Mode	Speed (m.s^{-1})	K^2
LiNbO$_3$	128 Y-cut	X-axis	SAW	3980	0.055
	Y-cut	Z-axis	SAW	3488	0.049
	41 Y-cut	X-axis	L-SAW	4792	0.172
	37 rotated		SSBW	4802	0.167
LiTaO$_3$	36 Y-cut	X-axis	SSBW	4160	0.05
	36 Y-cut	X-axis, metal	L-SAW	4112	0.047
	X-cut	112.2 Y-dim	SAW	3290	0.007
	42° Y-cut	X-axis	SSBW	4022	0.076
Quartz	ST	X-axis	SAW	3158	0.001
	Y-cut	X-axis	SAW	3159	0.001
	Y-cut ST	132.75°	SSBW	4990	0.018
	35.5 AT	0	SSBW	5100	0.014
	AT	90	SSBW	5060	

Table 1.1   Several piezoelectric materials with their characteristics.

Since interdigital transducers for piezoelectric excitation of elastic waves were first reported [2], several authors [25]-[28] have studied the coupling efficiency of such structures. Coquin and Tiersten [25] analysed the detection and excitation of surface waves on quartz by such transducers. They gave the coupling efficiency factor as a function of the line-width-to-wavelength ratio for the fundamental frequency. Ingebrigtsen [26] has calculated the excitation from an impressed electric current of given Fourier components in time and space. White [27] and Tseng [28] have considered the coupling efficiency at various spatial harmonics of the fundamental transducer period. These harmonics provide the excitation of surface waves at frequencies, where the transducer period is an odd multiple of the acoustic wavelength, depend critically upon the transducer geometry. The acoustic wave amplitudes of the various spatial harmonics are proportional to the corresponding Fourier components of the electric field distribution and have been derived by Engan [29]. The use of split fingers have been shown to cancel reflections and scattering into bulk waves and to couple to both the fundamental and third harmonic modes with essentially equal strength for Rayleigh waves [30]. Bristol [31] provided techniques for realizing a wide variety of useful nondispersive bandpass functions by using periodic unapodized transducers and more recently Vigil [32] gave an overview of the apodization technique for defining the impulse response of SAW filters. Harmonic filters offer easy fabrication, but inferior electrical data. Rather high insertion loss is an important disadvantage of harmonic devices. Some of the reasons are bulk wave radiation, low coupling of certain harmonics and viscous and ohmic losses at high frequencies. Moreover, harmonic devices cannot be perfectly matched when unidirectional transducers are employed. Harmonic unidirectional transducers solve some of the above problems and make these filters more attractive [33].

In recent years, SAW device application has been extended towards a higher frequency range. At high frequencies, resistivity of finger electrodes of IDT's and propagation loss exert a great influence on device characteristics. The coupling-of-modes (COM) theory is well known for analysing surface waves in periodic structures [34]. Nanometer lithography technology utilising

very thin anodic oxidation films has been used to extend the frequency range of SAW filters to around 10GHz [35]. Finally, An alternative method to produce high frequency SAW transducers on the insulating substrate as well as on a conductive substrate based on imprint lithography has been recently developed by Takagaki [36].

1.2.5 Delay lines

A delay line is a two-port system in which the output signal is time delayed with respect to the input. In the classic BAW or SAW delay line configuration, the delay can be controlled by "time of flight" by simply adjusting the path length between generating and receiving transducers. Regarding loss, there is an intrinsic loss of 6 dB for a bidirectional SAW transducer even if it is perfectly matched as it generates waves in forward and backward directions and there is a 3 dB loss for perfectly matched unidirectional generation. Loss in itself is not a problem for short delay lines of less than 10 or 20 μsec, and it can usually be reduced or compensated in such cases [55]. Of more importance is the presence of spurious signals, which can degrade the dynamic range. For SAW delay lines these include "triple transit echoes" and spurious bulk waves. The former can be suppressed by a variety of design techniques, including use of unidirectional transducers and multistrip couplers. The latter can be avoided by careful choice of crystal propagation direction and the judicious use of absorbing materials.

1.2.6 Multiple frequency operation

Ricco *et al* [37] have shown that monitoring only the frequency change resulting from a SAW sensor perturbation yields incomplete information as the various perturbations that can affect acoustic wave propagation characteristics depend differently upon frequency. In chemical sensing and materials characterization, making velocity and attenuation measurements at several frequencies make it possible to separate unambiguously from one

another some of the many and varied perturbations that can affect acoustic wave propagation. Ricco *et al* [37] designed and tested several multi-frequency SAW devices that can function as selective chemical sensors without the need for selective coating chemistry.

The fabrication of fundamental mode surface-acoustic-wave (SAW) filters for GHz frequencies requires an elaborate photolithography process. In order to reduce process demands or to increase the possible frequency range, interdigital transducers can be designed to work on spatial harmonics (section 2.1.3). But harmonic filters are known to be unattractive because of their high insertion loss. Huegli [38] showed that harmonic GHz filters made with unidirectional transducers can have moderate insertion loss. Low insertion loss is obtained if the signal transit time is short, the film thickness optimum and the filters are made with harmonic unidirectional transducers. The insertion loss of these filters is only 5 dB higher than the insertion loss of comparable fundamental mode devices. The production of a harmonic filter, however, is easier, resulting in better yield and lower cost. More recently, Newton *et al* [39] reported simultaneous operation of a Love wave biosensor at the fundamental and third harmonic for a sequence of deposition and removal of a model mass layer of lipids. Harmonic operation of STW filters have also been reported and the effect of grating metallization height reported [40]. Similarly, a study of the effect of the transducers metallization height on the generation of third harmonic resonating frequency of a SSBW on ST-quartz has been recently presented [41].

1.2.7 Alternative acoustic wave modes

Acoustic wave devices are described by the mode of wave propagation through or on a piezoelectric substrate. Acoustic waves are distinguished primarily by their velocities and displacement directions; many combinations are possible, depending on the material and boundary conditions. The IDT of each sensor provides the electric field necessary to displace the substrate and thus form an acoustic wave. The wave propagates through or along the substrate, where it is converted back to an electric field at the IDT at the end

of the propagation path. Transverse, or shear, waves have particle displacements that are normal to the direction of wave propagation and which can be polarized so that the particle displacements are either parallel to, or normal to, the sensing surface. Shear horizontal wave motion signifies transverse displacements polarized parallel to the sensing surface; shear vertical motion indicates transverse displacements normal to the surface. A wave propagating through the substrate is called a bulk wave. The most commonly used bulk acoustic wave (BAW) devices are the thickness shear mode (TSM) resonator and the shear-horizontal acoustic plate mode (SH-APM) sensor. If the wave propagates on the surface of the substrate it is known as a surface wave. The most widely used surface wave devices are the Rayleigh-type surface acoustic wave sensor and the shear-horizontal surface acoustic wave (SH-SAW) sensor.

All acoustic wave devices are sensors in that they are sensitive to perturbations of many different physical parameters. Any change in the characteristics of the path over which the acoustic wave propagates will result in a change in output. All the sensors will function in gaseous or vacuum environments, but only a subset of them will operate efficiently when they are in contact with liquids. The TSM, SH-APM, and SH-SAW all generate waves that propagate with mechanical displacements primarily in the shear horizontal mode. The shear horizontal wave does not radiate appreciable energy into liquids and can therefore be used for liquid operation without excessive damping. Conversely, the SAW sensor has a substantial surface-normal displacement that radiates compressional waves into the liquid, thus causing excessive damping. An exception to this rule occurs for devices using waves that propagate at a velocity lower than the sound velocity in the liquid. Regardless of the displacement components, such modes do not radiate coherently and are thus relatively undamped by liquids. Other acoustic waves that are promising for sensors include the flexural plate wave (FPW), Love wave, surface-skimming bulk wave (SSBW) and Lamb wave.

Shear horizontally polarised acoustic plate mode

These devices use a thin piezoelectric substrate, or plate, functioning as an acoustic waveguide that confines the energy between the upper and lower surfaces of the plate (fig. 1.2). As a result, both surfaces undergo displacement, so detection can occur on either side. This is an important advantage, as one side contains the interdigital transducers that must be isolated from conducting fluids or gases, while the other side can be used as the sensor.
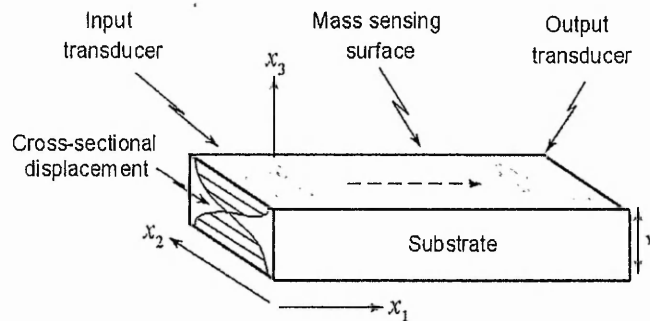
Fig. 1.2   Shear acoustic plate mode sensor configuration

As with the TSM resonator, the relative absence of a surface normal component of wave displacement allows the sensor to come into contact with liquid for biosensor applications. Although more sensitive to mass loading than the TSM resonator, SH-APM sensors are less sensitive than surface wave sensors. There are two reasons. The first is that the sensitivity to mass loading and other perturbations depends on the thickness of the substrate, with sensitivity increasing as the device is thinned. The minimum thickness is constrained by manufacturing processes. Second, the energy of the wave is not maximized at the surface, and this reduces sensitivity. Acoustic plate mode sensors were extensively studied in the late eighties by White [42] and Martin *et al* [43,44] as a viscosity sensor, examined for their potential as chemical sensor by Hou *et al* [45] and more recently as biosensors by Andle *et al* [46]. The theoretical and experimental mass sensitivity of the SH-APM have been examined by Toda *et al* for liquid sensing [47], and by Josse *et al*

[48], Liew *et al* [49], Dahint *et al* [50], Bender *et al* [51] and Schumacher *et al* [52] for identification of ion solutions and CVD thin film evaporation.

Surface acoustic wave

Rayleigh waves have both a longitudinal and a vertical shear component that can couple to a medium in contact with the device surface. Such coupling strongly affects the amplitude and velocity of the wave. This feature enables SAW sensors to directly sense mass and mechanical properties. The surface motion also allows the devices to be used as micro-actuators. The earliest reported uses of SAW devices as microsensors were by Wohltjen in 1979 [57] to measure thin film properties (chemical) and Das *et al* in 1978 [56] to measure pressure. Film properties that affect the SAW device include, mass, density, conductivity, permittivity, stress and viscoelasticity [53-58]. An additional important feature of SAW sensors is their ease of use in wireless applications. Examples include use in both the active mode, as the frequency control element in an oscillator [56], and passive mode, as wireless temperature [59] and stress [60] sensors. A major application of SAW sensors has been as highly sensitive mass detectors [53,58]. Wohltjen [7] suggested that SAW sensors have a mass sensitivity 200 times greater than the better known quartz crystal microbalance due to their higher operating frequency (up to 1GHz compared to about 10MHz for the quartz microbalance). A recent book by Ballantine *et al* provides a comprehensive description of SAW microsensor theory, design and applications [58].

Shear horizontally polarised surface acoustic wave

If the cut of the piezoelectric crystal material is rotated appropriately, the wave propagation mode changes from a vertical shear SAW to a shear-horizontal SAW. This dramatically reduces loss when liquids come into contact with the propagating medium, allowing the SH-SAW sensor to operate as a bio (chemical) sensor. Gulyaev gave an extensive review of shear

surface acoustic waves in solids [61] and theoretical calculations by Kovacs *et al* [8] showed that the sensitivity of SH-SAW devices is related to the ratio of group-to-phase velocity. Kondoh *et al* used a lithium tantalate substrate for simultaneous detection of density and viscosity [62], the identification of fruit juices [63] and pH changes [64]. They also used the transient response of the SH-SAW sensor to estimate components and concentration of ions in aqueous solutions without the need of selective coatings [65]. Nomura also examined the use of SH-SAW in liquids to detect variations in conductivity [66] and more recently, Weiss *et al* studied the influence of multiple layer of antibodies on a SH-SAW device [14].

Love wave

Acoustic wave devices based on surface skimming bulk waves (SSBW) propagating perpendicular to the x-axis of Y-rotated α-quartz plates (Y rot-quartz) have attracted much attention for high frequency filter as well as liquid sensor applications [67,68]. They show high phase velocities V and pure shear-horizontal polarization. By employing a dielectric layer d with a significantly lower shear speed V_l as an acoustic waveguide on top of the propagation surface, a SSBW can be converted into low loss Love modes [69] (Fig. 1.3). Table 1.2 summarizes the shear acoustic velocities and densities of various materials.
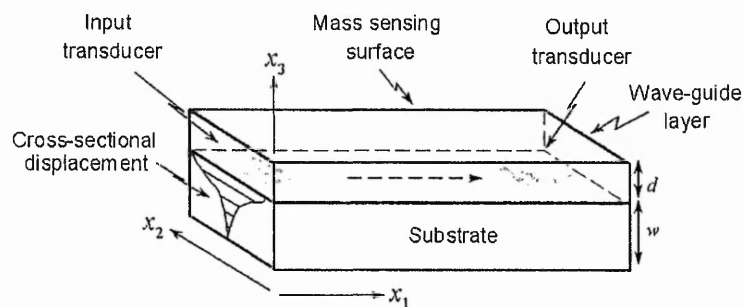
Fig. 1.3   Love wave sensor configuration.

Material	Shear acoustic velocity (m s^{-1})	Density (g cm^{-3})
Beryllium	8880	1.87
Quartz	4990	2.65
Silica (fused)	3764	2.20
Copper	2325	8.93
Silver	1698	10.4
Gold	1200	19.7
Polystyrene	1120	10.6
PMMA	1100	11.8
Lead	700	11.4
Polyethylene	540	0.90

Table. 1.2   Shear acoustic velocities and densities of various materials [55].

Dependent on the relative thickness d/λ of the guiding layer, Love modes show an increased coupling factor and improved sensitivity to viscous and gravimetric interactions compared to SSBW's. Generally, oscillation frequency as well as attenuation changes of delay line oscillators can be used as the measurand. Theoretical calculations by Kovacs *et al* [40], Enderlein *et al* [70] and Wang *et al* [71] have shown that the thickness of the guiding layer determines the sensitivity of the Love mode and its coupling into the layer. Fused Silica (SiO_2) has been proved successful as a guiding layer [72,73] since it is a standard material in semiconductor industry, featuring low damping along with a sufficiently low phase velocity [74].

Love waves are very promising as sensors in gaseous and liquid environments because of their high sensitivity. Polymethylmethacrylate (PMMA) based Love wave sensors exhibit a sensitivity approaching that of optimum SiO_2 based Love wave sensors. Preliminary work on a new hybrid Love wave device structure incorporating a PMMA/SiO_2 bilayer indicated that higher sensitivity than the optimum SiO_2 devices can be obtained. A device with slightly higher sensitivity than the optimum for SiO_2 devices has been reported to operate successfully in water and buffer [75]. Gizeli *et al* [11] utilized PMMA layers spun onto Y-cut quartz with interdigital transducers (IDT's) of periodicity 45 μm at the quartz-PMMA interface. Kovacs *et al* [73] utilized SiO_2 layers on ST-cut quartz and Jakoby and Vellekoop [76] used plasma enhanced CVD SiO_2. Harding and Du [77,78] have investigated hybrid devices incorporating guiding layers consisting of sputtered SiO_2 overlaid by spun PMMA or spun polystyrene. The mass sensitivity of Love-wave devices incorporating silicon dioxide guiding layers have been determined experimentally in some detail using a technique based on mass loading by ultra thin gold films by Harding [77]. Significant variations have been observed in the relative sensitivities of the IDT and the "sweet spot" (between the IDT's) areas for devices of different guiding layer thickness. Measurements made on devices incorporating a novel developed silicon-oxy-fluorine guiding layers show that the deposition conditions strongly influence the shear velocity, allowing high sensitivity to be achieved for relatively small layer thickness. To improve the performances of Love wave devices, new cuts resulting in the fabrication of zero temperature coefficient for the oscillating frequency were used by Jakoby *et al* [79].

1.3 Quartz Crystal Microbalance (QCM)

The Thickness Shear Mode resonator (TSM), widely referred to as a quartz crystal microbalance (QCM), is the best-known, oldest, and simplest acoustic wave device. As shown in fig. 1.4, the TSM typically consists of a thin disk of AT-cut quartz with parallel circular electrodes patterned on both sides.

The application of a voltage between these electrodes results in a shear deformation of the crystal. This device is known as a resonator because the crystal resonates as electromechanical standing waves are created. The displacement is maximized at the crystal faces, making the device sensitive to surface interactions. The TSM resonator was originally used to measure metal deposition rates in vacuum systems where it is commonly used in an oscillator circuit. The oscillation frequency tracks the crystal resonance and indicates mass accumulation on the device surface. In the late 1960s, the TSM resonator was shown to operate as a vapor sensor. The TSM features simplicity of manufacture, ability to withstand harsh environments, temperature stability, and good sensitivity to additional mass deposited on the crystal surface. Because of its shear wave propagation component, the TSM resonator is also capable of detecting and measuring liquid properties, making it a good candidate for a biosensor. Unfortunately, these devices have the lowest mass sensitivity of the sensors examined here. Typical TSM resonators operate between 5 and 30 MHz. Making very thin devices that operate at higher frequencies can increase the mass sensitivity (section 2.3), but thinning the sensors beyond the normal range results in fragile devices that are difficult to manufacture and handle. Most of the applications involving sensors based on piezoelectric quartz crystals rely on the monitoring of the oscillator resonant frequency changes, which are correlated with gravimetric changes. The Sauerbrey equation [80] is used to correlate those frequency changes with added rigid mass,

$$\Delta f = \frac{-2f^2}{\sqrt{\mu_Q \rho_Q}} \frac{\Delta m}{A}$$

where f is the operating frequency, Δf is the fractional change in frequency due to the added mass per unit area $\Delta m / A$, A is the area of the disk, μ_Q and ρ_Q are the shear modulus and density of the crystal respectively. However, the acoustic wave sensor, especially when operated in the liquid phase, is affected by other interfacial properties.
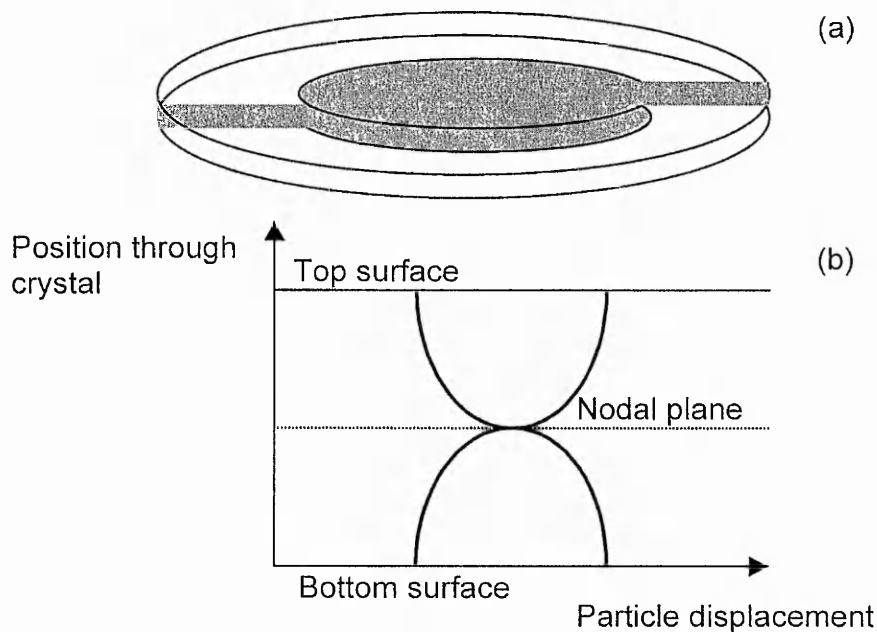
Fig. 1.4   (a) Thickness shear mode (TSM) resonator consisting of a thin disk of quartz with circular gold electrodes on both faces and (b) the fundamental thickness shear resonance condition in a quartz crystal excited by surface electrodes.

Nomura and Minemura [4] were the first to verify that the frequency depended on the density and conductivity of the solution. Nomura and Okuhara [81] suggested that the frequency of a crystal immersed in an organic liquid containing no electrolyte is influenced only by the density (ρ) and the viscosity (η) of the solution,

$$\Delta f = a\rho^{1/2} + b\eta^{1/2}$$

and verified that the crystal did not oscillate in liquids of high density and viscosity. Yao and Zhou [82] verified that for mixtures of water/organic solvent, the frequency depended also on the dielectric constant of the liquid. In 1985, the first physical models of QCM sensors operated in the liquid phase were developed by Bruckenstein and Shay [83], and Kanazawa and

Gordon [84]. Bruckenstein and Shay [83] used dimensional analysis to develop the following equation,

$$\Delta f = 2.26 \times 10^6 \, n f^{3/2} (\eta_l \rho_l)^{1/2}$$

where $n = 1$ or 2 depending on whether one or two faces of the crystal contact the solution. Kanazawa and Gordon [84] treated the quartz as a loss-less elastic solid and the liquid as a purely viscous fluid. The frequency shift arose from coupling the oscillation of the quartz, a standing shear wave, with a damped propagating shear wave in the liquid; the fractional change in frequency is derived by taking in account the shear wave viscous penetration depth, δ, defined as, $\delta = \sqrt{2\eta_l / \rho_l \omega}$, where η_l and ρ_l are the viscosity and density of the liquid respectively, ω is the oscillation angular frequency. The derived expression for the frequency shift:

$$\Delta f = f^{3/2} \left(\frac{\eta_l \rho_l}{\pi \mu_Q \rho_Q} \right)^{1/2}$$

was similar to the one of Bruckenstein and Shay, and both predict that density and viscosity are relevant parameters for the operation of a quartz crystal in a liquid. Kurosawa *et al* [85] showed that the circuit influenced the frequency changes measured in solutions and that the equation of Bruckenstein and Shay and Kanazawa and Gordon did not hold for electrolytes or polymer solutions. Schumacher *et al* [86-88] introduced a new factor, surface roughness, in the parameters that affect the oscillation frequency. Frequency became a function of Δm_l, the mass per unit area of the liquid confined in the cavities of the roughness surface, a function of ε, the mean diameter of the hemicylinders with liquid entrapment,

$$\Delta f_s = \frac{-2 f_o^2 \Delta m_l}{\sqrt{\mu_Q \rho_Q}}, \qquad \Delta m_l = \frac{1}{2} \rho_l \varepsilon$$

Heusler *et al* [89] studied surface stress influence on the resonant frequency. Hager and Verge [90], and Hager [91] developed a model based on hydrodynamic coupling between the oscillating crystal and adjacent liquid. Liquid dielectric constant is considered, and the empirical equation contains constants dependent on the crystal equivalent circuit and the working conditions,

$$\Delta f = k_l \Delta (\rho_l \eta_l)^{1/2} + f(\Delta \varepsilon_l)$$

Shana *et al* [92] presented an equation for thin films of viscous liquid of height h, where k_2 is the wave number in the crystal in the y-direction.

$$\Delta f = f^{3/2} \left[\frac{\eta_l \rho_l}{d_Q C_{66} \pi} \right]^{1/2} \left| \tanh(k_2 h) \right|$$

If h is sufficiently large, the equation is similar to the one of Kanazawa and Gordon if the piezoelectric effect is neglected. Thompson *et al* [93] proposed that the changes in interfacial surface structure and interfacial properties such as free energy and slippage were related to the resonance frequency of a crystal in contact with a liquid, and reviewed the theoretical aspects of operation of a thickness shear mode acoustic wave sensor in contact with a liquid [94]. Many of the current sensor concepts used with the other acoustic wave devices arise from the understanding of the models that apply to the QCM.

1.4 Applications of acoustic wave sensors

Bulk and surface acoustic wave sensors have been used extensively in the design of multifunctional physical and chemical sensors, including microbalances [95-97], viscosity sensors [43], humidity sensors [98], immuno-

detectors [99-100], gas sensors [101], ion-intercalation monitors [102] and magnetic- and electric-field sensors [103]. Acoustic wave sensors become pressure, torque, shock, and force detectors under an applied stress that changes the dynamics of the propagating medium. They become mass, or gravimetric, sensors when particles are allowed to contact the propagation medium, changing the stress on it. They become vapor sensors when a coating is applied that absorbs only specific chemical vapors. These devices work by effectively measuring the mass of the absorbed vapor. If the coating absorbs specific biological chemicals in liquids, the detector becomes a biosensor. Chemical sensors based on crystal BAW and SAW resonators have been reported for both the gas and the liquid state [18,104-108].

Because the coating material of an acousto-electronic gas sensing platform is rarely exclusively selective for a single component, the resonating crystal sensor, as with most chemical sensors, is susceptible to interfering analytes. An alternate approach is the use of individual sensors for an analysis in which interferents may be present is the multivariate approach with an array of sensors, each coated with a different, partially selective, coating material. Biosensors are similar to chemo-sensors, but they utilize biological molecules as selective coating. Extreme selectivity is obtained by the antibody-antigen reaction and such sensors are called immuno-sensors. Immuno-sensors work only in the liquid phase with most successful work based on thickness shear AT-crystals [109]. One example of SAW-based biosensor is a desoxyribo-nucleic acid (DNA) hybridisation detector [110]. A major problem associated with biosensors is that they usually work non-reversibly, and the crystals can be reused only after repeating the sophisticated preparation procedure each new measurement.

The Love mode acoustic sensor has recently been used in biosensing applications. In 1992, Gizeli *et al* [13] developed a direct immunosensor using an acoustic wave device as a transducer. The device was based on an acoustic waveguide geometry that supports a Love wave. Gizeli *et al* [13] demonstrated the detection of microgram levels of immunoglobulin-G (IgG) per milliliter of buffer and Harding *et al* [111] the detection of ng ml^{-1} of sheep immunoglobulin. More recently, Weiss *et al* [14] used multilayers of antibody

films as selective coating and waveguide, Josse *et al* [112] demonstrated the detection of pg mm^{-2} of goat immunoglobulin by using such devices and also used Love wave sensors for sensing organic compounds traces down to 200 ppb. Zimmerman *et al* [20] utilized a Love wave sensor as a gas sensor to detect organophosphorous compounds. Principles of pulsed acoustic waves operations for sensing was first reported by McHale *et al* [21] and pulse mode operation of a Love wave bio (chemical) sensor was simultaneously demonstrated by Stevenson *et al* [22] and Newton *et al* [23].

1.5 Project Overview

For biochemists, it is of major significance to understand the interactions of a small ligand with a cell membrane. Bio-molecular recognition mechanisms involving binding, incorporation and formation of ion channels, are complex and existing systems cannot provide such information as elastic and electric properties of the biological system and, thus, cannot provide a full picture of biological interactions. Surface acoustic wave devices have been proposed as tools to provide this information [8,11,14,20,22,72,73,112]. Shear waves in solids have been reviewed by a number of authors [54,55,58,61]. A certain class of guided shear waves, the so-called Love wave sensors were shown to be of particular interest for their high sensitivities and their capability to work in liquids. Although many authors have reported the use of Love wave sensors for bio (chemical) sensing, few have provided an understanding of the propagation mechanisms. Pulsed wave techniques, providing essentially short-lived continuous waves, were proposed in the 1950s [113], used to measure grain orientation of metal samples [114] and to probe elastic properties of protein films [115]. This type of technique was shown to provide a different perspective on the acoustic modes generated and their influence on device efficiency. This type of system has the advantage of being able to identify the precise mode of wave by its transit time and is capable of detecting very low-level signals. The aim of this thesis is to provide a comprehensive understanding of the mechanisms of propagation of layer

guided shear-horizontally polarized acoustic waves, assess the mass sensitivity of Love wave sensors and to develop high frequency instrumentation for using Love wave sensors for liquid and bio-sensing.

Harmonic signals and surface acoustic wave device design are resented in chapter two, followed by the basic theory of elastic wave propagation in solids and a review of shear horizontal polarised waves. A new generalized dispersion equation for layer guided SH-SAW sensors is presented, a new class of guided acoustic wave sensors is identified and the mass sensitivity of layer guided SH-SAWs is predicted. In the last section, a novel approach to phase and group velocities provide a new derivation of mass sensitivity of acoustic wave sensors. An account of the experimental techniques is presented in Chapter three. Acoustic wave sensor fabrication techniques, instrumentation of vacuum evaporated metals, spin-coating of polymer layers and the flow cell arrangement for acoustic sensing are detailed. Chapter three is also concerned with the development of a novel pulse mode interrogation system, whose principle, capabilities and applications will be discussed. Experimental results and discussion of major findings are presented in Chapters four and five. Chapter four covers the Love wave acoustic sensor sensitivity to elastic, visco-elastic and liquid loading. Harmonic signals and frequency impact on Love wave operations will be described. Love wave higher order modes will be identified, their sensitivity investigated and their relevance discussed. Pulse mode operation of guided SH-SAW sensors is presented in Chapter five and the method is applied to a model biosensing experiment. Finally, mass sensitivity of Love wave devices from phase and group velocities measurements will be presented and the relevance of the group velocity as a new and highly sensitive parameter will be discussed. An overview and possible directions of further developments of the project are provided in Chapter six.

References

[1] Lord Rayleigh, Proc. Lond. Math. Soc., **17** (1885).

[2] R. M. White, F. W. Voltmer, Appl. Phys. Lett., **7** (1965), 314.

[3] W. H. King, Anal.Chem, **36** (1964), 1735.

[4] T. Nomura, A. Minemura, Nippon Kahaku Kaishi, (1980), 1621.

[5] P. L. Konash, G. J. Bastiaans, Anal. Chem., **52** (1980), 1929.

[6] J. E. Roederer, G. J. Bastiaans, Anal. Chem., **55** (1983), 2333.

[7] W. Wohltjen, Sens. Act., **5** (1984), 307-325

[8] G. Kovacs, A. Venema, Appl. Phys. Lett, **61** (1992), 639.

[9] L. Tessier, F. Patat, N. Schmitt, L. Pourcelot, Y. Frangin, D. Guilloteau, Proc. Ultrason. Int.'93 Vienna Austria, (1993), 627.

[10] F. Aberl, H. Wolf, C. Koblinger, S. Drost, P. Woias, S. Koch, Sensors and Actuators B, **18-19** (1994), 271.

[11] E. Gizeli, N. Goddard, C. Lowe, Sensors and Actuators B, **6** (1992) 131.

[12] R. L Baer, C. A Flory, proc. 1992 IEEE ultrasonics Symp., Tucson, AZ, USA, (1992).

[13] E. Gizeli, M Liley, C. R. Lowe and H Vogel, Anal. Chem, 69 (1997), 4808.

[14] M. Weiss, Anal.Chem, **70** (1998), 2881.

[15] M. Penza, L. Vasanelli, Sensors and Actuators B, **41** (1997), 31.

[16] F. L. Dickert, M. E. Zenkel, W. E. Bulst, G. Fischer, J. Fresenius, Anal. Chem., **357** (1997), 27.

[17] Y. J. Lee, H. B. Kim, Y. R. Roh, H. M. Cho, S. Baik, Sensors and Actuators A, **64** (1998), 173.

[18] D. Enguang, F. Guanping, H. Zenhua, C. Dafu, IEEE Trans. Ultrason. Ferroelectr., Freq. Contr., **44** (1997), 309.

[19] B. Jakoby, G. M. Ismael, M. P. Byfield, M. J. Vellekoop, Sensors and Actuators A, **76** (1999), 93.

[20] C. Zimmermann, D. Rebiere, C. Dejous, J. Pistre, E. Chastaing, R. Planade, Sensors and Actuators B, **3735** (2001), 1-9.

[21] G. McHale, M. I. Newton, M. K. Banerjee, S. M. Rowan, Faraday Discuss., **107** (1997), 15.

[22] A. C. Stevenson, H. M. Mehta, R. S. Sethi, L. E. Cheran, M. Thompson, I. Davies, C. R. Lowe, The Analyst, **126** (2001), 1619.

[23] R. Chung, R. A. McGill, IEEE Inter. Freq. Contr. Symp., (1998), 634.

[24] M. I. Newton, G. McHale, F. Martin, E. Gizeli, K. A. Melzak, The Analyst, **126** (2001), 2107.

[25] G. A. Coquin, H. F. Tiersen, J. Acoust. Soc. Am., **41** (1967), 921.

[26] K. A. Ingebrigtsen, J. Appl. Phys, **40** (1969), 2681.

[27] R. M. White, IEEE Trans. Electron. Dev., **14** (1967), 181.

[28] C. C. Tseng, IEEE Trans. Electron. Dev., **15** (1968), 586.

[29] H. Engan, IEEE Trans. Electron. Dev., **16** (1969), 1014.

[30] T. W. Bristol, IEEE Trans. Sonics. Ultrasonics., **19** (1972), 343.

[31] T. W. Bristol, IEEE Trans. Sonics. Ultrasonics., **19** (1972), 377.

[32] A. J. Vigil, B. P. Abbott, D. C. Malocha, Proc. IEEE, (1987), 139.

[33] R. Huegli, Ultrasonics Symp., (1987), 183.

[34] K. Hirota, K. Nakamura, Jpn. J. Appl. Phys, **33** (1994), 2972.

[35] K. Yamanouchi, T. Meguro, Y. Wagatsuma, H. Odawaga, K. Yamamoto, Jpn. J. Appl. Phys., **33** (1994), 3018.

[36] Y Takagaki, E. Wiebicke, H. Kostial, K. H. Ploog, IOP Publishing nanotechnology, **13** (2002), 15.

[37] A. J. Ricco, S. J. Martin, Sensors and Actuators B, **10** (1993), 123.

[38] R. Huegli, Trans. Ultrason. Ferrolectr. Freq. Control, **40** (1993).

[39] M. I. Newton, F. Martin, K. A. Melzak, E. Gizeli, G. McHale, Electr. Lett., **37** (2001), 340.

[40] R. L. Baer, C. A. Flory, Ultras. Symp., (1988), 53.

[41] F. Martin, Electr. Lett., **38** (2002), 941.

[42] R. W. White, P. J. Wicher, S. W. Wenzel, E. T. Zellers, IEEE Trans. Ultrason. Ferro. Freq. Contr , **34** (1987), 162.

[43] A. J. Ricco, S. J Martin, Appl. Phys. Lett, **50** (1987), 1474.

[44] S. J. Martin, A. J. Ricco, Sensors and Actuators A, **20** (1989), 253.

[45] J. Hou, H. Van der Vaart, Ultrason. Symp., (1987), 573.

[46] J. C. Andle, J. T. Weaver, J. F. Vetelino, D. C. McAllister, F. Josse, Ultrason. Symp., (1993), 331.

[47] K. Toda, A. Sawaguchi, Jpn. J. Appl. Phys., **33** (1994), 2949.

[48] F. Josse, J. C. Andle, J. F. Vetelino, R. Dahint, M. Grunze, IEEE Trans. Ultrason. Ferro. Freq. Contr., **42** (1995), 517.

[49] S. Liew, F. Josse, D. T. Haworth, Z. A. Shana, U. R. Kelkar, M. Grunze, Ultrason, Symp., (1990), 285.

[50] R. Dahint, Z. A. Shana, F. Josse, S. A. Riedel, M. Grunze, IEEE Trans. Ultrason. Ferro. Freq. Contr, **40** (1993), 114.

[51] F. Bender, R. Dahint, F. Josse, M. Grunze, M. v. Schickfus, J. Acoust. Soc. Am., **95** (1994), 1386.

[52] J. Schumacher, R. Dahint, F. Josse, M. Grunze, Ultrason, Symp., (1994), 629.

[53] S. M. Sze, Semiconductor sensors, New York (Wiley), (1994).

[54] C. Campbell, Boston Academie, (1989).

[55] D. P. Morgan, Amsterdam (Elsevier), (1991).

[56] P. Das, C. Lanzl, D. Barone, IEEE Ultrason. Symp., (1978).

[57] H. Wohltjen, Anal. Chem., **51** (1979), 1458.

[58] D. S. Ballantine, R. M. White, S. J. Ricco, A. J. Martin, E. T. Zellers, G. C. Frye, H. Wohltjen, San diego, CA: Academic, (1997).

[59] X. Q. Bao, W. Burkhard, V. V. Varadan, V. K. Varadan, IEEE Ultrason. Symp. (Denver, CO), (1987), 583.

[60] V. K. Varadan, V. V. Varadan, X. Q. Bao, Proc. SPIE, Int. Soc. Opt. Eng. (San Diego, CA), (1996), 95.

[61] Y. V. Gulyaev, IEEE Trans. Ultrason. Ferroelectr. Freq. Contr., **45** (1998), 935.

[62] J. Kondoh, S. Hayashi, S. Shiokawa, Jpn. J. Appl. Phys., **40** (2001), 3713.

[63] J. Kondoh, S. Shiokawa, Jpn. J. Appl. Phys, **33** (1994), 3095.

[64] J. Kondoh, S. Shiokawa, Sensors and Actuators B, **13-14** (1993), 429.

[65] T. Yamazaki, J. Kondoh, Y. Matsui, S. Shiokawa, Sensors and Actuators A, **83** (2000), 34.

[66] T. Nomura, A. Saitoh, Y. Horikoshi, Sensors and Actuators B, **3732** (2001), 1-5.

[67] J. Y Duquesnoy, Proc.IEEE Ultrason. Symp., **57** (1982).

[68] H. Drobe, A. Leidl, Sensors and Actuators, **141** (1193), 37-38.

[69] B. A Auld, Acoustic fields in solids, **vol II**, R E Krieger PC, Malabar (1990).

[70] J. Enderlien, E. Chilla, H. J. Frohlich, Sensors and Actuators A, **41-42** (1994), 472.

[71] Z. Wang, J. D. N. Cheeke, C. K. Jen, Appl. Phys. Lett., **64** (1994), 2940.

[72] J. Du, G L Harding, Sensors and Actuators A, **56** (1996), 211.

[73] G. Kovacs, Proc. IEEE Ultrasonics Symp. Tucson, AZ, USA (1992).

[74] F. Herrmann, S. Buttenbach, Physica status solidi, pss/RRN-98-045, (2000).

[75] G. L Harding, Smart. Mater. Struct., **6** (1997).

[76] B. Jakoby, M J Vellekoop, Sensors and Actuators A, **678** (1998).

[77] G. L Harding, Sensors and Actuators A, **88** (2001).

[78] J. Du, G. L Harding, Sensors and Actuators A, **65** (1998)

[79] B. Jakoby, J. Bastemeijer, M. J. Vellekoop, Sensors and Actuators A, **82**, (2000).

[80] G. Sauerbrey, Z. Phys, **155** (1959), 206.

[81] T. Nomura, M. Okuhara, Anal. Chim. Acta., **142** (1982), 281.

[82] S. Z. Yao, T. A. Zhou, Anal. Chim Acta., **212** (1988), 61.

[83] S. Bruckenstein, M. Shay, Electrochem. Acta, **30** (1985), 1295.

[84] K. K. Kanasawa, J. G. Gordon II, Anal. Chim. Acta., **175** (1985), 99.

[85] S. Kurosawa, E. Tawara, N. Kama, Y. Kobakate, Anal. Chim. Acta., **230** (1990), 41.

[86] R. Schumacher, G. Borges, K. K. Kanazawa, Surf. Sci., **163** (1985), L621.

[87] W. Stockel, R. Schumacher, Ber. Bunsenges. Phys. Chem., **91** (1987), 345.

[88] R. Schumacher, Angewandte, **29** (1990), 329.

[89] K. E. Heusler, A. Grzegorzewski, L. Jackel, J. Pitrucha, Ber. Bunsenges Phys. Chem., **92** (1988), 1218.

[90] H. E. Hager, P. D. Verge, Sensors and Actuators, **7** (1985), 271.

[91] H. E. Hager, Chem. Eng. Commun., **43** (1986), 25.

[92] Z. A. Shana, D. E. RadkteTawara, U. R. Kelkar, F. Josse, Anal. Chim. Acta, **231** (1990), 317.

[93] M. Thompson, C. L. Arthur, G. K. Dhaliwal, Anal. Chem., **58** (1986), 1206.

[94] M. Thompson, A. L. Kipling, W. C. Duncan-Hewitt, L. V. Rajakovic. B. A. Cavic-Vlasak, A Review Analyst, **116** (1991), 881.

[95] C. Wei and K. Rajeshwar, J. Electrochem. Soc., **140** (1993), L128.

[96] R. Oltra and I. O. Efimof, J. Electrochem. Soc., **141** (1994), 1838.

[97] D. Ivanov A. Yelon, J. Electrochem. Soc., **143** (1996), 2835.

[98] G. Gerlach, K. Sager, Sensors and Actuators A, **43** (1994), 181.

[99] M. Rapp et al., The 7th Int. Conf. Sensors and Actuators (1997), 538.

[100] J. Kondoh, Y. Matsui, S. Shiokawa, The 7th Int. Conf. Sensors and Actuators (1997), 534.

[101] J. Vetelino, R.K. Lade, R.S. Falconer, IEEE Trans. Ultrason., Ferroelect., and Freq. Contr., UFFC-34 (Piscataway, NJ:IEEE, 1987), 156.

[102] K. Takeshita, W. Wernet, N. Oyama, J. Electrochem. Soc.141 (1994), 2004.

[103] S.M. Hanna, IEEE Trans. Ultrason., Ferroelect., and Freq. Contr., UFFC-34 (Piscataway, NJ: IEEE, 1987), 191.

[104] R. Lucklum, B. Hanning, P. Jauptmann, K. D. Schierbaum, S. Vaihinger, W. Gopel, Sensors and Actuators A, **25-27** (1991), 705.

[105] H. Muramatsu, M. Suda, T. Ataka, A. Seki, E. Tamiya, I. Karube, Sensors and Actuators A, **21-23** (1990), 362.

[106] M. Penza, L. Vasanelli, Sensors and Actuators B, **41** (1997), 31.

[107] F. L. Dickert, M. E. Zenkel, W. E. Bulst, G. Fischerauer, J. Fresenius, Anal. Chem., **357** (1997), 27.

[108] Y. J. Lee, H. B. Kim, Y. R. Roh, H. M. Cho, S. Baik, Sensors and Actuators A, **64** (1998), 173.

[109] L. Tessier, F. Patat, N. Schmitt, L. Pourcelot, Y. Frangin, D. Guilloteau, Proc. Ultrason. Int.'93 Vienna Austria, (1993), 627.

[110] F. Aberl, H. Wolf, C. Koblinger, S. Drost, P. Woias, S. Koch, Sensors and Actuators B, **18-19** (1994), 271.

[111] G. L. Harding, J. Du, P. R. Dencher, D. Barnett, E. Howe, Sensors and Actuators A, **61** (1997), 279.

[112] F. Josse, F. Bender, R. Cernosek, Anal. Chem., **73** (2001), 5937.

[113] W.P. Mason, Van Nostrand, N. Y., (1950).

[114] B. W. Maxfield, A. Kuramoto, J. K. Hulbert, Mater. Eval., **45** (1990), 1166.

[115] M. Rodahl, F. Hook, C. Frederiksson, C. A. Keller, A. Krozer, P. Brzezinski, M. Voivona, B. Kasemo, Faraday discuss., **107** (1197), 229.

CHAPTER 2
THEORY

CHAPTER 2

THEORY

2.1 Design of IDT's

2.1.1 IDTs for Rayleigh-SAW devices

In applications of the surface acoustic wave phenomenon to electronic devices, piezoelectric materials are required to convert the incoming signal to an acoustic one, and vice-versa. In its simplest form, a transversal SAW filter consists of two transducers with interdigital arrays of thin metal electrodes deposited on a highly-polished piezoelectric substrate such as quartz or lithium niobate (Fig. 2.1). The electrodes that comprise these arrays alternate polarities so that an RF signal voltage of the proper frequency applied across them causes the surface of the crystal to expand and contract. This generates the Rayleigh wave. These interdigital electrodes are generally spaced at 1/4 wavelength of the operating centre frequency. Since the surface wave or acoustic velocity is 10^{-5} slower than the speed of light, an acoustic wavelength is much smaller than its electromagnetic counterpart. As a result of this relationship, physical limitations exist at higher frequencies when the electrodes become too narrow to fabricate with standard photolithographic techniques and at lower frequencies when the devices become impractically large. Hence, at this time, SAW devices are most typically used from 10 MHz to about 3 GHz. The basic SAW transducer is a bi-directional radiator. That is, half of the power is directed toward the output transducer while the other half is radiated toward the end of the crystal and is lost. By reciprocity, only half of the intercepted acoustic energy at the output is reconverted to electrical energy; hence, the inherent 6 dB loss associated with this structure. Numerous second-order effects, such as coupling efficiency, resistive losses, and impedance mismatch, raise the insertion loss of practical filters to 15 - 30 dB.
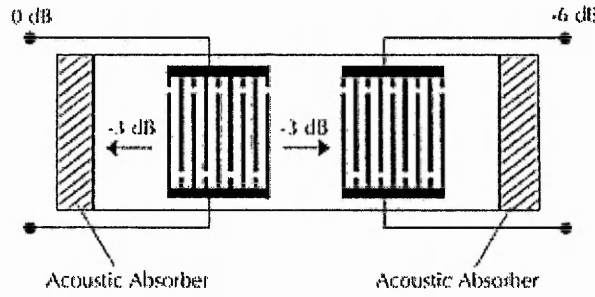
Fig. 2.1   Simple transversal SAW filter configuration.

2.1.2 Transducer impedance and bandwidth considerations

The equivalent circuit for a basic single-single IDT for a Rayleigh-SAW can be either a parallel combination of an acoustic conductance $G_a(\omega)$, an acoustic susceptance $B_a(\omega)$ and a capacitance C_t (Fig. 2.2), or a series combination of an acoustic radiation $R_a(\omega)$, an acoustic reactance $X_a(\omega)$ and a capacitance C_t (Fig. 2.3). The frequency response of such a simple device is a (sin x/x) function and the IDT admittance is complex and has the form,

$$Y_t(\omega) = j\omega C_t + G_a(\omega_\circ)\left[\left(\frac{\sin x}{x}\right)^2 + j\left(\frac{\sin 2x - 2x}{2x^2}\right)\right] \tag{1}$$

where $\omega = 2\pi f$ is the angular frequency, x contains a frequency dependence through, $x = N_p \pi(\omega - \omega_\circ)/\omega_\circ$, where N_p is the number of electrical periods in the IDT. From equation (1), the number of electrical periods in the IDT determines the frequency bandwidth, i.e the 4 dB width of the resonance is 1/time it takes for the SAW to pass along its length.
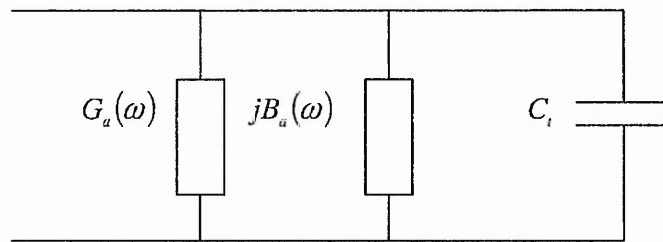
Fig. 2.2　　　Parallel combination of the equivalent circuit for a basic single-single IDT for a Rayleigh-SAW.
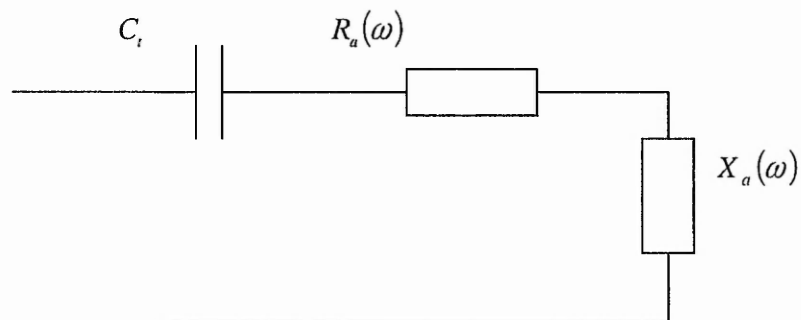
Fig. 2.3　　　Series combination of the equivalent circuit for a basic single-single IDT for a Rayleigh-SAW.

In order to deliver the maximum power into the SAW, the IDT must look like a 50 Ω load when driven at the resonant frequency. The key parameter is the radiation resistance which is,

$$R_a(\omega) = \frac{G_a(\omega)}{G_a^2(\omega) + \left[B_a(\omega) + \omega C_t\right]^2} \tag{2}$$

Resonance $R_a(\omega)$ can be approximated to,

$$R_a(\omega_\circ) = \hat{R}_a \equiv \frac{G_a(\omega_\circ)}{(\omega_\circ C_t)^2} \tag{3}$$

2.4

For a single-single equal mark-and-space ratio transducer design and by using the formula, $V = f_o \lambda_{IDT}$, Eq. (3) can be re-written as,

$$R_a(\omega_o) \approx \hat{R}_a = \frac{2.871\left(\dfrac{K^2}{2}\right)}{2\pi M V (\varepsilon_o + \varepsilon_p^T)} \propto \frac{1}{M} \tag{4}$$

where $\dfrac{K^2}{2} = \left|\dfrac{\Delta V}{V}\right|$, $W = M\lambda_{IDT}$ is the aperture. The radiation resistance determines how well a device is matched to the 50 Ω source for a given resonant frequency and is set by the aperture, W. Eq. (4) is valid for Rayleigh-SAWs only. In the case of a surface skimming bulk wave (SSBW), the following replacement must be used: $2.871\left(\dfrac{K^2}{2}\right) \rightarrow 0.7K$.

2.1.3 Harmonic design

Generally, the maximum centre frequency obtainable is about 1.5 GHz, since this requires 0.5 μm line widths when single-electrode transducers are used. Narrower line widths can be obtained by electron beam lithography. However, some special techniques enable higher frequencies to be obtained without requiring narrower line widths. A simple approach is to use a harmonic response of a transducer, for example, the third harmonic of a double-double transducer. If the presence of the fundamental response is undesirable, it may be virtually eliminated in a two-transducer device by using transducers operated at different harmonics, as shown by Engan [1]. For example, the device may have 3 fingers in each transducer wavelength section (S_e=3) and operate at the second harmonic and a S_e=4 (i.e 4 fingers in each transducer wavelength section, Fig. 2.4) transducer operated at the third harmonic. In this case there is little overlap of the fundamental responses of the transducers. An additional advantage is that electrode interaction effects are minimised. Generally, only the first few harmonics are useful for high-

frequency operation, because for harmonic numbers greater than S_e the coupling efficiency of the transducer is found to be quite sensitive to the metallisation ratio a/p, where a is the width of a finger and p is the width of a finger+space, which is difficult to control accurately for narrow electrodes. The sensitivity to a/p is due to rapid variations of the elemental charge density with a/p. To overcome this difficulty, modified types of transducer have been proposed [2] using electrodes with different widths in each period. These transducers give harmonic responses less sensitive to errors in the electrode widths, though the coupling strength is rather weak.
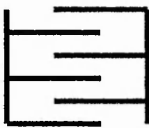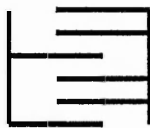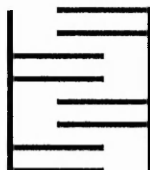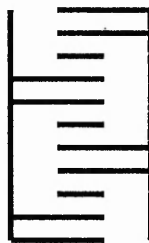
2-finger	3-finger	4-finger	6-finger
$S_e=2$ single-single f_0	$S_e=3$ single-double $f_0, 2f_0$	$S_e=4$ double-double split $f_0, 3f_0$	$S_e=6$ $f_0, 5f_0$

Fig. 2.4   Relationship between design of transducers and the number of operating harmonics

2.3.4 SSBW

In the device considered here, interdigital transducers are used to generate bulk waves deliberately. The device structure is essentially the same as that of a surface wave device, with two interdigital transducers on a plane surface; the bulk wave travels close to the surface between the transducers, and is therefore called a "surface skimming bulk wave", or SSBW. The configuration is as in fig. 2.5. For practical devices, the substrate material and orientation are chosen such that there is no electrically-coupled surface wave mode, so that no surface wave is excited. It is also necessary that the bulk wave should not be significantly disturbed by the boundary conditions at the surface. For an isotropic material a shear horizontal bulk wave propagating parallel to the surface is not affected by the surface boundary conditions. A similar solution can sometimes be found for anisotropic piezoelectric materials, and it is found that some orientations give this solution and also give no electrical coupling to surface waves, and are thus suitable for SSBW devices. For example, there are several suitable orientations of quartz. SSBW devices have many features in common with surface wave devices, including in particular the considerable flexibility obtainable by apodising the transducers. With a suitable choice of substrate the velocity can be 60% higher than that of surface waves, giving the advantage of a higher operating frequency for a given electrode periodicity. Alternatively, for other orientations, very good temperature stability can be obtained, much better than the stability for surface waves on ST x-cut quartz. In addition, the SSBW is found to be less affected by surface contamination. Consequently, these waves are particularly suitable for oscillators and for narrow-band bandpass filters. However, the design of these devices is complicated by the fact that the bulk wave is not guided along the surface; thus, the wave diffracts into the bulk of the material, and the disturbance at the surface decays with distance.

At large distances a wave generated at $x=0$ can be expected to have an amplitude proportional to $x^{-1/2}$, as deduced from power conservation. For a device using short uniform transducer and a long apodised transducer, the attenuation is readily compensated by modifying the apodisation. In practice,

the form of the attenuation may be modified by the presence of an additional acoustic mode.
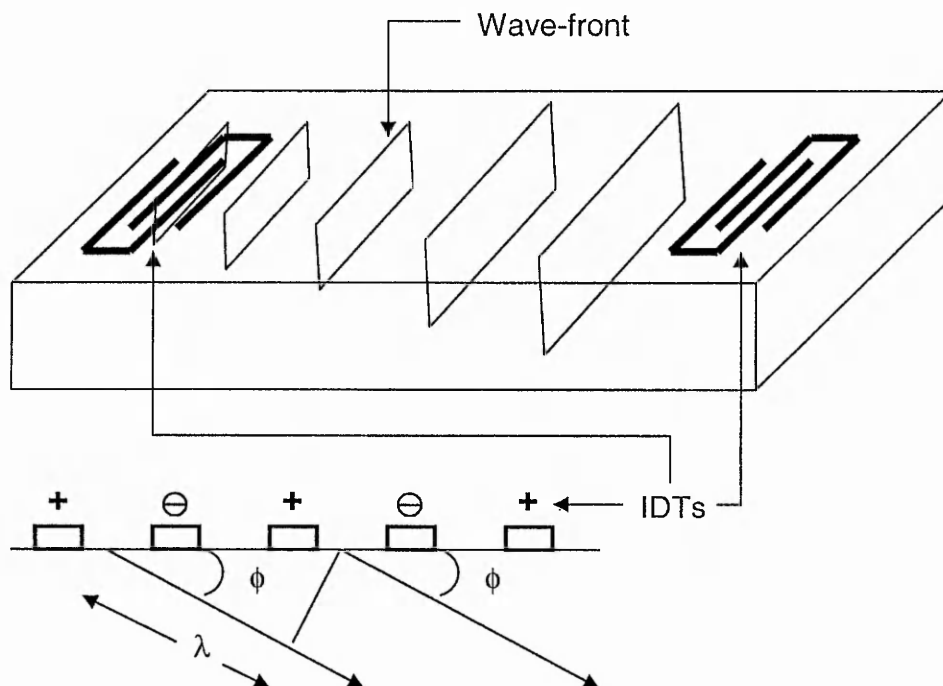
Fig. 2.5   Schematic view of SSBW devices. In such devices, the acoustic wave is launched at an angle ϕ to the surface.

2.2 Piezoelectricity

There are several different methods for exciting ultrasonic waves, including piezoelectricity, electrostriction, magnetostriction, electromagnetic laser generation, etc. Of these, the piezoelectric effect is by far the most widely used. Piezoelectricity means that we can apply a stress to a crystal and not only is a strain produced but also a difference of potential between opposing faces of the crystal. This is called the direct piezoelectric effect. Conversely, the indirect effect corresponds to applying a difference of potential, which induces a strain in the crystal. Since the process is known to work at extremely high frequency (up to 10^{12} Hz), piezoelectric crystals can be used to generate (inverse effect) and detect (direct effect) ultrasonic waves.

The key to the phenomenon lies in the absence of a centre of symmetry in piezoelectric crystals. This is, in fact, a necessary but not a sufficient condition for piezoelectricity; of the 21 crystal systems lacking a centre of symmetry, 20 are piezoelectric. The physics of the piezoelectricity effect can be understood by referring to the case of quartz, using a simple one-dimensional model. Suppose that $\pm q$ are the charges of positive and negative ions, and a is the charge dimension of the unit cell. The induced polarization can be expressed as qa/unit cell volume $= eS$, where e is the piezoelectric stress constant and S is the strain. Then the usual relation for dielectric media can be written,

$$D = \varepsilon_{\circ_o} E + P = \varepsilon^S E + eS \tag{5}$$

where D and E are the electric displacement and electric field, respectively. The superscript S is standard in the literature for such relations and corresponds to permitivity at constant or zero strain. In a similar way, it can be shown that,

$$T = c^E S - eE \tag{6}$$

Where c is the stiffness and e the piezoelectric coupling coefficient. These relations are known as the piezoelectric constitutive relations.

2.3 Elastic waves in non piezoelectric solids

2.3.1 Equations of motion

Applying a force to a solid puts the solid under stress results in strain. An elastic wave propagating in a solid displaces an infinitesimal small element of elastic solid defined by the cartesian co-ordinates (x_1, x_2, x_3) from its equilibrium position due to the exerted force. The displacement caused by the exerted force can be defined by a vector U (U_1, U_2, U_3) and has three

components, U_1, U_2 and U_3, representing the particle displacements, parallel to the Cartesian axes. Strain and stress tensors are given respectively by,

$$S_{ij}(\underline{x}) = \frac{1}{2}(\frac{\partial U_i}{\partial x_j} + \frac{\partial U_j}{\partial x_i}) \tag{7}$$

$$T_{ij}(\underline{x}) = \sum_{kl} C_{ijkl} S_{kl} \tag{8}$$

where i, j, k, separately take the value of 1, 2, 3, which correspond to the three axis (x_1, x_2, x_3), k, l are summed when repeated, U_l are the components of displacements and C_{ijkl} is the elasticity tensor. By ignoring the piezoelectric effect (described in section 2.2), Newton's third law gives the equation of motion generalized to the three co-ordinates,

$$\rho\frac{\partial^2 U_i}{\partial t^2} = \sum_{j=1}^{3}\frac{\partial T_{ij}}{\partial x_j} \tag{9}$$

Where ρ is the mass density of the solid and with i=1, 2, 3, corresponding to the Cartesian co-ordinates x_1, x_2, x_3. Consider the elasticity tensor in an isotropic and non-piezoelectric material of Lamé constants λ and μ,

$$C_{ijkl} = \lambda\delta_{ij}\delta_{kl} + \mu(\delta_{ik}\delta_{jl} + \delta_{il}\delta_{jk}) \tag{10}$$

where λ, μ>0. Substituting equation (10) in equation (8) gives,

$$T_{ij} = \lambda\delta_{ij}\sum_{k=1}^{3}S_{kk} + 2\mu S_{ij} \tag{11}$$

Substituting the new stress tensor equation (11) into the equations of motion (9) gives the basic equation of motion for an isotropic material neglecting piezoelectricity,

$$\rho \frac{\partial^2 U_j}{\partial t^2} = (\lambda + \mu) \frac{\partial}{\partial x_j} \sum_{k=1}^{3} S_{kk} + \mu \nabla^2 U_j \qquad (12)$$

The plane–wave form of the equation of motion for an isotropic solid, neglecting piezoelectricity can then be deduced from (12),

$$\omega^2 \rho \underline{U}^\circ = (\lambda + \mu)(\underline{k}.\underline{U}^\circ)\underline{k} + \mu \underline{k}^2 \underline{U}^\circ \qquad (13a)$$

where $\underline{U} = \underline{U}^\circ e^{i(\omega t \mp \underline{k} \cdot \underline{x})}$ (13b)

2.3.2 Shear and longitudinal waves

In isotropic solids, shear waves propagating with the vector $\underline{k}$, has a displacement $\underline{U}^\circ$ perpendicular to $\underline{k}$, whilst longitudinal waves have the displacement vector $\underline{U}^\circ$ parallel to the propagation vector $\underline{k}$.

Shear waves in isotropic solids

The transverse propagation direction vector is defined as $\underline{k}_t = \underline{k}$ and the equation of motion (13 a)) becomes,

$$\omega^2 \rho = \mu \underline{k}_t^2 \qquad (14)$$

If we then consider the transverse (shear) speed as $V_t = \sqrt{\dfrac{\omega^2}{\underline{k}_t^2}}$ (15), the transverse wave velocity can be simply expressed as a function of the mass density and rigidity of the solid,

$$V_t = \sqrt{\frac{\mu}{\rho}} \qquad (16)$$

The transverse wave velocity is found to be independent of ω and is therefore non-dispersive.

Longitudinal waves in isotropic solids

The longitudinal propagation direction vector is now defined as $\underline{k}_l = \underline{k}$ and the equation of motion (13) becomes,

$$\frac{\omega^2}{\underline{k}_l^2} = \left(\frac{\lambda + 2\mu}{\rho}\right) \tag{17}$$

If we then consider the compression (shear) speed as $V_l = \sqrt{\dfrac{\omega^2}{\underline{k}_l^2}}$ (18), the longitudinal wave velocity can be simply expressed as a function of the mass density and the Lamé constants of the solid,

$$V_l = \sqrt{\frac{\lambda + 2\mu}{\rho}} \tag{19}$$

The longitudinal wave velocity is also found independent of ω, and is also non–dispersive. By comparing equations (16) and (19), we deduce that the longitudinal wave velocity is higher than the transverse wave velocity.

2.3.3 Displacements normal to the sagittal plane

Consider the propagation vector $\underline{k}$ in the x_1-x_3 sagittal plane and the displacement vector $\underline{U}$ is along the x_2 direction. $\underline{k}$ and $\underline{U}$ have the following coordinates,

$\underline{k} = (k_1, 0, k_3)$
$\underline{U} = (0, U, 0)$,
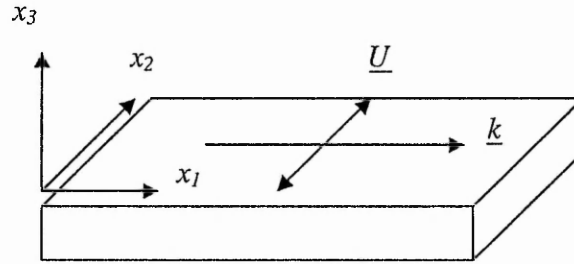
Fig. 2.6   Definition of axes and propagation direction normal to the sagittal plane.

and the phase speed is defined as,

$$V = \frac{\omega}{k_1},$$

The equation of motion (13) together with the definitions of transverse and shear wave velocities (16), (19) becomes,

$$k_3^2 = \omega^2 \left(\frac{1}{V_t^2} - \frac{1}{V^2} \right) \tag{20}$$

Equation (20) is described as the dispersion equation and, by imposing boundary conditions, k_3 can be determined and so determines the phase velocity.

2.3.4 Specific solutions satisfying boundary conditions

Thickness shear mode: the quartz crystal microbalance (QCM) case

Consider now the propagation vector $\underline{k}$ along the x_3 direction and the displacement vector $\underline{U}$ along the x_2 direction, with $\underline{k}$ perpendicular to $\underline{U}$. The vectors $\underline{k}$ and $\underline{U}$ have the following coordinates,

$$\underline{k} = (0,0,k_3)$$

$$\underline{U} = (0,U^\circ,0) \, ,$$
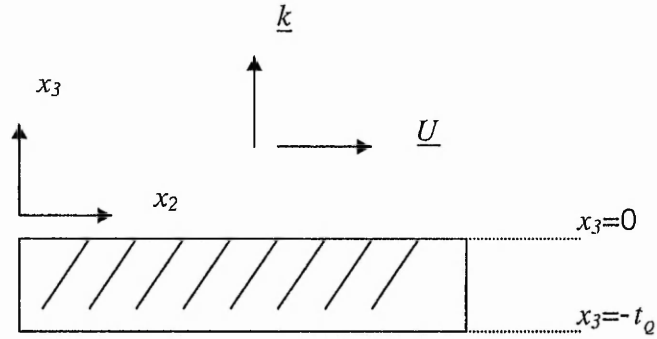
Fig. 2.7   Definition of axes and propagation direction for a thickness shear mode in a system of finite substrate.

and the transverse wave velocity is defined as (16),

$$V_t = \sqrt{\frac{\mu}{\rho}} \, ,$$

The solutions of the shear wave equation of motion are of general form,

$$\underline{U} = (0,1,0)U^\circ e^{j(\omega t \mp k_3 x_3)} \tag{21}$$

and the specific solutions satisfying the boundary conditions are of the form,

$$U_2^{sol} = (Ae^{-jk_3 x_3} + Be^{jk_3 x_3})e^{j\omega t} \tag{22}$$

where the constants A and B can be found from the boundary conditions, i.e vanishing stress at the bottom and top of the plate: $T_{23} = 0$ at $x_3=0$ and $x_3=-t_Q$ (see fig. 2.7). Together with equation (11), the stress tensor can be extracted and the specific solution derived,

$$U_2^{sol} = 2A\cos(k_3 x_3)e^{j\omega t} \tag{23}$$

and, from the boundary conditions, the oscillation frequency can also be derived,

$$f = \frac{nV_t}{2t_Q} \qquad (24)$$

where $n=0,1,2,3...$ and describes the number of modes of oscillation inside the crystal. Hence, the fundamental frequency is defined as $n=1$,

$$f_o = \frac{V_t}{2t_Q} \; ,$$

and the harmonic frequencies corresponding to higher order modes are then defined as,

$$f_n = nf_o \qquad (25)$$

Shear horizontal acoustic plate mode

Consider the propagation vector $\underline{k}$ is in the x_1-x_3 sagittal plane and the displacement vector $\underline{U}$ is along the x_2 direction, with $\underline{k}$ perpendicular to $\underline{U}$. The vectors $\underline{k}$ and $\underline{U}$ have the following coordinates,

$$\underline{k} = (k_1, 0, k_3)$$
$$\underline{U} = (0, U, 0) \, ,$$

The general form of solutions for the propagation of a plane wave along the x_1 direction is,

$$\underline{U} = (0,1,0)U^o e^{j(\omega t - k_1 x_1)} e^{\pm jk_3 x_3} \qquad (26)$$
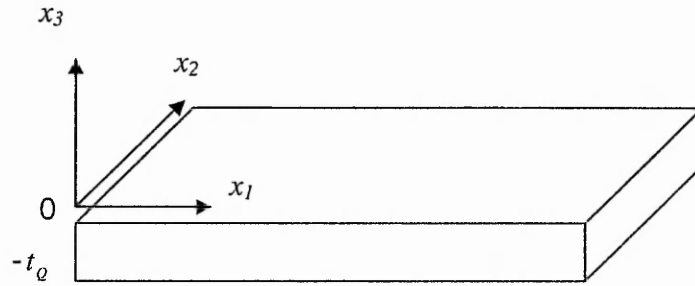
Fig. 2.8   Definition of axes and propagation direction in a system of finite substrate.

The specific solution is now a combination of the general form, similar to equation (22), but with an extra contribution of the k_1 component.

Deriving the specific solution similarly to the thickness shear mode case, the harmonic oscillation frequency of the shear acoustic plate mode can be presented as,

$$f = \frac{n}{2} \cdot \frac{1}{t_Q} \frac{1}{\sqrt{\left(\frac{1}{V_t^2} - \frac{1}{V^2} \right)}} \qquad (27)$$

Equation (27) can be re arranged and the velocity expressed as a function of the transverse velocity,

$$V = \frac{V_t}{\sqrt{1 - \left(\frac{nV_t}{2ft_Q} \right)^2}} \qquad (28)$$

where n is the number of modes and $n=0,1,2,3..$ Equation (28) describes the set of shear acoustic plate mode velocities linked to a given frequency of operation.

Shear horizontal surface acoustic waves

The shear acoustic wave case can be treated similarly to the shear acoustic plate mode case, but with an infinite substrate. The boundary requires the wave to decay in depth. The vectors $\underline{k}$ and $\underline{U}$ have the following coordinates,

$$\underline{k} = (k_1, 0, k_3)$$

$$\underline{U} = (0, U, 0),$$

The general form of the solutions for propagation of plane wave along the x_1 axis is identical to the shear acoustic plate mode. However, only positive values of the k_3 component are now allowed as solutions must decay with depth. With stress free boundary conditions at both upper lower face of the substrate, the phase velocity of the shear acoustic wave is deduced and found to be equal to the transverse wave velocity.
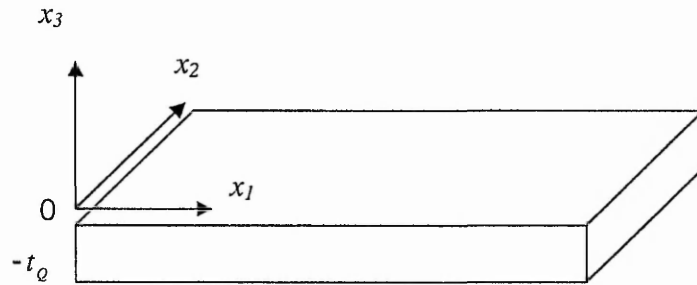
Fig. 2.9   Definition of axes and propagation direction for a shear horizontal surface acoustic wave in a system of infinite substrate.

The displacement vector is now defined as,

$$\underline{U} = (0,1,0)Ae^{j(\omega t - k_1 x_1)} \tag{29}$$

Equation (29) describes a plane shear wave propagating parallel to the surface with a phase velocity $V = V_t$.

Love wave

An infinite substrate of density ρ_s, phase velocity V_s and with Lamé constants λ_s and μ_s is now considered with an overlayer of finite thickness d, density ρ_l, phase velocity V_l and with Lamé constants λ_l and μ_l. Displacements are then described by the equation of motion (13) where $\underline{k} = \Gamma_l$ in the layer and $\underline{k} = i\Gamma_s$ for the substrate, and solutions describing love wave displacements can be derived as,

$$\Gamma_s^2 = \omega^2 \left(\frac{1}{V^2} - \frac{1}{V_s^2} \right) \tag{30a}$$

$$\Gamma_l^2 = \omega^2 \left(\frac{1}{V_l^2} - \frac{1}{V^2} \right) \tag{30b}$$
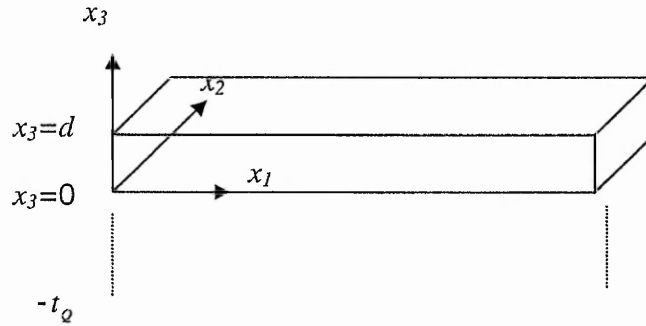
Fig. 2.10   Definition of axes and propagation direction of a Love wave in a system of infinite substrate and finite thickness layer.

The boundary conditions are continuity of stress at each interface and continuity of displacements at $x_3=0$, the constants defined and a dispersion equation derived,

$$\tan(\Gamma_l d) = \xi \tag{31a}$$

where $\xi = \dfrac{\mu_s \Gamma_s}{\mu_l \Gamma_l}$ \hfill (31b)

The dispersion equation (31a) is highly non-linear but can be solved numerically and the phase speed obtained for the various modes (section 2.4.2.2).

2.3.5 Thickness shear mode response to solids and liquids

Models to predict the fractional change in frequency for an added solid mass and in liquid medium have been proposed by Sauerbrey [3], and Kanazawa and Gordon [4], respectively.

Sauerbrey equation

Equation (24) describes the operation frequency in TSM system, i.e $f = \dfrac{nV_t}{2t_Q}$.

The simplest view of mass sensitivity is to consider the added solid mass as an extension to the crystal thickness itself. Then the fractional change in frequency can be developed,

$$\frac{\Delta f_n}{f_n} = -\frac{2nf_\circ}{V_t} \Delta t_Q \tag{32}$$

where Δt_Q is the fractional change in thickness towards the crystal due to the added solid mass. Similarly, equation (32) can be expressed as a function the change in mass per unit area, defined as Δm_Q,

$$\frac{\Delta f_n}{f_n} = -\frac{2nf_\circ}{\sqrt{\mu_Q \rho_Q}} \Delta m_Q \tag{33}$$

Defining the sensitivity as the fractional change in frequency for a change in mass per unit area towards quartz mass as,

$$S_m = \lim_{\Delta m_Q \to 0} \left(\frac{\Delta f_n}{f_\circ} \right) \frac{1}{\Delta m_Q} = -\frac{2nf_\circ}{\sqrt{\mu_Q \rho_Q}}, \tag{34}$$

Fig. 2.11 Definition of the layer and the substrate thicknesses for a thickness shear wave in a system of finite substrate and finite added solid layer.

Equation (34) gives the mass sensitivity function, S_m, and can be approximated and generalised to any kind of layer as following,

$$\left(\frac{\Delta f_n}{f_\circ} \right) = S_m \Delta m_Q \approx S_m \Delta m \tag{35}$$

Kanazawa and Gordon equation

For a Newtonian liquid, the penetration depth can be defined as,

$$\delta = \sqrt{\frac{2\eta_l}{\omega \rho_l}} \tag{36}$$

where η_l and ρ_l are the viscosity and density of the fluid, respectively. Equation (33) can be re-written for liquid medium,

$$\frac{\Delta f_n}{f_n} = -\frac{2nf_\circ}{\sqrt{\mu_Q \rho_Q}} \Delta m_l \tag{37}$$

$x_3=0$

$x_3=-t_Q$

Fig. 2.12   Definition of the substrate thickness and liquid media penetration depth for a thickness shear wave in a system of finite substrate and infinite liquid layer.

Δm_l is the mass of the liquid, and can expressed as a function of the penetration depth,

$$\Delta m_l = \delta . \rho_l = \sqrt{\frac{\eta_l \rho_l}{\pi f_n}} \tag{38}$$

Together with equation (37), the fractional change in frequency for an added mass of liquid is derived and approximated to,

$$\Delta f_n \propto f^{3/2} \sqrt{\rho_l \eta_l} \tag{39}$$

The above derivation of equation (39) has the advantage of being in analogy to mass loading but does not quite give a correct overall numerical factor. It also neglects the energy losses that occur in a liquid.

Rigorous view for solids

An improved approach towards QCM response to surface mass loading would consist in considering the thickness shear mode solutions to the equation of motion in the layer and in the substrate. Those solutions are identical to equations (22),

$$U_2^{sub} = (Ae^{-jk_3x_3} + Be^{jk_3x_3})e^{j\omega t} \tag{40a}$$

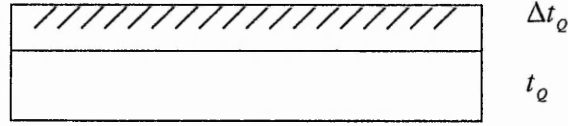$$U_2^{layer} = (Ae^{-jk_3x_3} + Be^{jk_3x_3})e^{j\omega t} \tag{40b}$$
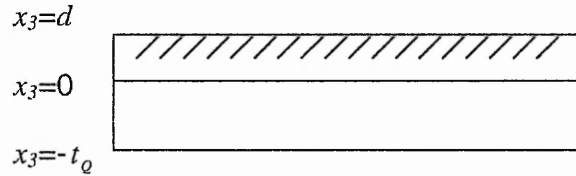
Fig. 2.13   Definition of axis and definition of the layer and the substrate for a thickness shear wave in a system of finite substrate and finite added solid layer.

Phase velocities in the substrate and in the layer are then derived as a function of ω,

$$V_l = \frac{\omega}{k_3^l} = \sqrt{\frac{\mu_l}{\rho_l}} \tag{41a}$$

$$V_s = \frac{\omega}{k_3^s} = \sqrt{\frac{\mu_s}{\rho_s}} \tag{41b}$$

Because the boundary conditions impose free stress at the interfaces and continuity of displacements at the interface substrate/solid, $T_{23} = 0$ and $U_2^{sub} = U_2^{layer}$. Those equations can be solved for very small solid layer and the change in the oscillation frequency ω can be determined.

Rigourous view for liquids

The liquid motion is governed by the Navier-Stokes equation for one-dimensional plane –parallel flow,

$$\eta \frac{\partial^2 V_2}{\partial x_3^2} = \rho \frac{\partial V_2}{\partial t} \tag{42a}$$

and stress tensor is,

$$T_{23} = -\eta \frac{\partial V_2}{\partial x_3} \tag{42b}$$

where V_2 is the speed and is defined as,

$$V_2 = \frac{\partial U_2}{\partial t},$$

The solution for the one-dimensional plane-parallel flow is of general form:

$$V_2(x_3,t) = A' e^{-x_3/\delta} \cos\left(\frac{x_3}{\delta} - \omega t\right),$$
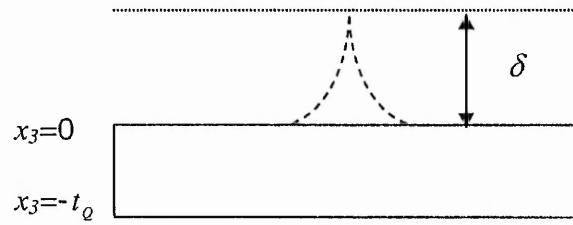

$x_3=0$

$x_3=-t_Q$
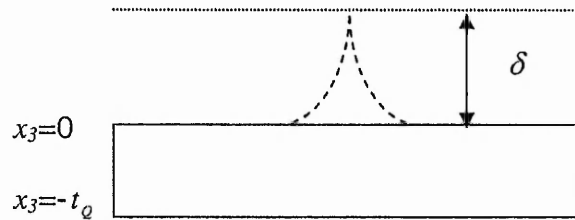
Fig. 2.14 Definition of the substrate thickness and liquid media penetration depth for a thickness shear wave in a system of finite substrate and infinite liquid layer.

and, similarly, the solution for the liquid displacement is,

$$U_2(x_3,t) = A e^{-x_3/\delta} \sin\left(\frac{x_3}{\delta} - \omega t\right),$$

The substrate is still governed by the thickness shear mode equation of motion (21) and fractional change in frequency can be determined by imposing boundary conditions at the interface solid/liquid and free stress at the boundaries.

2.4 Love wave and layer guided shear horizontal acoustic plate mode sensors

2.4.1 Operation limits of QCM

For aqueous phase sensors the requirement for simple, robust devices has led to a focus on shear horizontally polarized acoustic waves, which in their idealised theory, do not suffer from significant compressional wave generation. The simplest of these devices is the quartz crystal microbalance (QCM), which operates at typical frequencies of 5-10 MHz. In liquid applications, the oscillation of the crystal induces a shear oscillation in the liquid which decays within a frequency dependent penetration depth of $\delta = (2\eta_f/\omega\rho_f)^{1/2}$, where η_f and ρ_f are the viscosity and density of the fluid and $\omega = 2\pi f$ is the angular frequency. This viscous entrainment means the QCM only senses the mass of liquid within an interfacial layer and as a consequence the frequency shift is proportional to the viscosity-density product and a lower power of the frequency, i.e. $\Delta f/f = C(\eta_f\rho_f f)^{1/2}$, where C is a material constant [5,6]. In liquid phase operation the quartz crystal also has a dissipation. The quartz crystal can be used in electrochemical applications [7], biochemical applications [8] and with polymer layers [9], although in this latter case the response of the crystal is more complicated than when operated solely in a liquid [10,11]. To avoid compressional wave problems and gain higher sensitivity, shear horizontally polarised acoustic wave are more suitable. Gas phase acoustic sensors have also sought higher sensitivity by increasing the operating frequency. Nonetheless, the most successful application of QCM sensors has been in the measurement of the deposition of thin metal films in vacuum systems [12]. The measured frequency shift is proportional to the mass of the film. If the film density and acoustic impedance are known, then the film thickness can be obtained. The method is accurate providing the film is thin, stiff and adheres well to the surface. QCMs use a thickness shear mode vibration and increasing frequency requires thinner, and hence more fragile, crystals. An alternative approach is to use surface

acoustic waves generated by interdigital transducers (IDTs) [13]. Relatively thick piezoelectric substrates can then be used and the operating frequency is determined by the finger spacing of the IDTs, which determines the wavelength. Surface acoustic wave device types with a dominant shear horizontal polarization include surface transverse waves (STWs) [14], leaky SAWs [15], surface skimming bulk waves (SSBWs) [16] and Love waves [17,18] The Love wave configuration has been reported as having one of the highest mass sensitivities [19]. However, in aqueous phase sensing, these devices need to have an IDT on the same face of the substrate as the liquid and this is a disadvantage. Shear acoustic plate modes (SH-APM) are excited and detected by IDTs on the opposite face of the substrate but exhibit a poor mass sensitivity [20,21].

In principle, a Love wave is a shear horizontally polarized acoustic wave that is localized to the surface of a semi-infinite half space and guided by a layer, which has a shear acoustic speed less than that of the half space material [18]. In practice, the substrate is finite. The phase velocity of the Love wave is intermediate between that of the substrate and the layer and is determined by the layer thickness. In comparison, an acoustic plate mode occurs when a finite thickness substrate is excited at a natural resonant frequency of the substrate [22,23]. In practical application, SH-APMs will also have a surface coating layer when operated as mass sensors and this mass layer is likely to possess a shear acoustic speed lower than that of the substrate. In theory, both the Love wave and the lowest order, $n=0$, SH-APM mode correspond to a plane wave. In Love wave theory, multiple modes can occur with the lowest order mode containing a node in the displacement at infinite depth into the substrate and an antinode at the free surface at the top of the guiding layer. In SH-APM theory, both the top face and lower face of the substrate are anti-nodes so that multiple modes occur with SH-APM modes corresponding to resonances of the plate matching a multiple of a half-wavelength condition. In a Love wave the phase speed is less than that of the shear acoustic speed of the substrate, whereas, in a SH-APM the phase speed is higher than that of the shear acoustic speed of the substrate. From a theoretical point of view, as operated, both Love waves and SH-APMs use

finite substrates, both may have finite thickness mass layers with lower shear acoustic speeds than the substrate and both use a propagation parallel to the substrate with a surface transverse displacement. The primary difference is that a Love wave requires a decaying displacement with depth into the substrate whilst a SH-APM uses a resonating solution. It is therefore possible to describe both Love waves and mass coated SH-APMs using a single theoretical approach.

2.4.2 Love waves and acoustic plate modes

2.4.2.1 Comparison of modes

In section 2.3, a dispersion equation was derived for shear horizontally polarised acoustic waves propagating in a system composed of a finite thickness substrate and a finite thickness guiding layer where the shear acoustic speed of the layer, V_l, is less than that of the substrate, V_s. For small thickness guiding layers, calculations show that these solutions correspond to traditional Love waves (for $V<V_s$) and to acoustic plate modes (APM) (for $V>V_s$). As the thickness of the waveguide is increased, multiple Love wave modes can occur and each of these Love wave mode has an associated set of acoustic plate modes (for $V>V_s$); Those plate modes associated to the Love wave modes are identified as layer guided acoustic plate modes. Similarly to the Love wave, the phase speed of the acoustic plate mode will decrease as the thickness of the waveguide is increased. When the waveguide is further increased, the phase velocity of the plate mode eventually reaches the value of the lower shear acoustic speed of the lower acoustic plate mode and, if the value of the shear speed in the substrate, namely Vs, is reached, the acoustic plate mode transforms into the associated mode of the Love wave. The sensitivity to mass deposition of those modes is related to the slope of the dispersion curves and, by choosing an appropriate substrate thickness, it can be shown that the layer guided acoustic plate mode can have an enhanced mass sensitivity, similar or even higher than the mass sensitivity of the traditional Love wave. In practise, both sensors exhibit a horizontally polarised

displacement, use a substrate of finite thickness, propagate in a delay line and are excited by interdigital transducers (IDTs). In mass sensing operations, both modes will have a mass layer, whether it is the wave-guiding layer or the mass layer being sensed. The major difference is whether the displacement decays with depth into the substrate or whether the substrate acts as a resonator.

2.4.2.2 Dispersion curves

The response of a two-layer system (i.e of a substrate and a wave-guide) to the deposition of rigid mass can be considered as solving the propagation of shear horizontal acoustic waves in a three-layer system. For the finite substrate Love wave and layer guided SH-APM sensors, we consider a substrate of thickness, w, with a density ρ_s and Lamé constants λ_s and μ_s overlayed by a uniform mass layer of thickness, d, and with a density ρ_l and Lamé constants λ_l and μ_l, referred to as the guiding layer and the love wave sensor consisting of a finite substrate plus the guiding layer will be referred to as the bare device.

In section 2.3, the derivation of a dispersion equation was outlined for such a system. The third layer has a thickness, h, with a density ρ_p and Lamé constants λ_p and μ_p and is referred to as a perturbing mass layer. To derive a dispersion equation, a wave motion in an isotropic and non-piezoelectric material of density ρ and with Lamé constants λ and μ needs to be considered. The displacements, U_j are then described by the equation of motion of the form,

$$\rho \frac{\partial^2 U_j}{\partial t^2} = (\lambda + \mu) \frac{\partial S_{ii}}{\partial x_j} + \mu \underline{\nabla}^2 U_j \qquad (43)$$

and boundary conditions are applied to each of the interfaces.

(a)
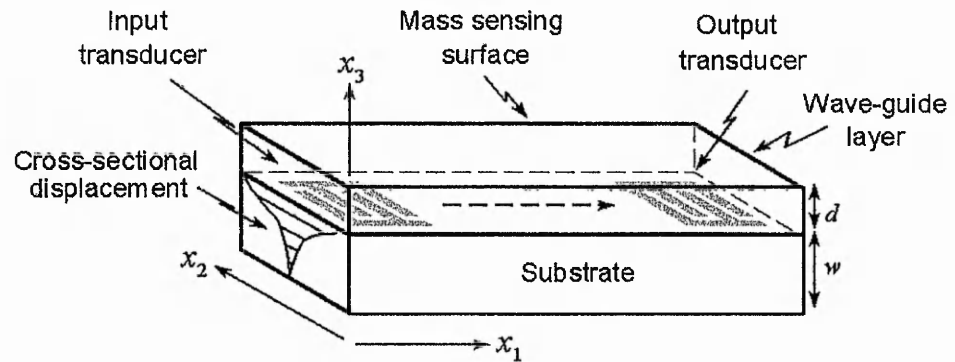
(b)
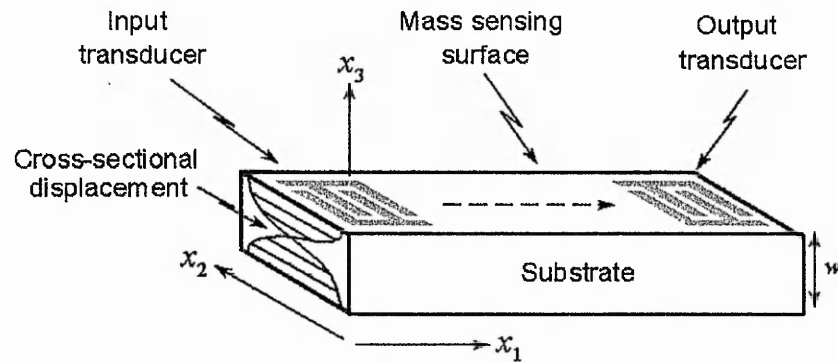
Fig. 2.15 (a) Love wave and (b) SH-APM sensor configurations. In each case mode propagation is parallel to the x_1-axis with displacements in the x_2 direction. The Love wave decays with depth whilst the SH-APM uses a substrate resonance; the lowest order mode is indicated schematically in both cases.

The solutions of the equations of motion are chosen to have a propagation along the x_1 axis with displacements in the x_2 direction of the sagittal plane (x_2-x_3). They must also satisfy the boundary conditions on the displacements $\underline{U}$ and the T_{i3} component of the stress tensors. The imposed boundary conditions are continuity of stress at each interface (substrate/guiding layer, guiding layer/perturbing mass layer), and continuity of displacements at $x_3=-w$ and $x_3= (d+h)$. The T_{i3} component of the stress tensors must vanish at the free

surfaces of the substrate and the perturbing mass layer at $x_3 = -w$ and $x_3 = (d+h)$, respectively. Using this approach McHale et al [24] derived,

$$\tan(\Gamma_l d) = \xi \tanh(\Gamma_s w) - \xi_p \tan(\Gamma_p h)[1 + \xi \tan(\Gamma_l d) \tanh(\Gamma_s w)] \tag{44}$$

where the defining equations for the wave vectors Γ_s, Γ_l, and Γ_p, are,

$$\Gamma_s^2 = \omega^2 \left(\frac{1}{V^2} - \frac{1}{V_s^2} \right), \ \Gamma_l^2 = \omega^2 \left(\frac{1}{V_l^2} - \frac{1}{V^2} \right), \Gamma_p^2 = \omega^2 \left(\frac{1}{V_p^2} - \frac{1}{V^2} \right) \tag{45}$$

and the intrinsic speed of the layers are given by $V_s = (\mu_s/\rho_s)^{1/2}$, $V_l = (\mu_l/\rho_l)^{1/2}$ and $V_p = (\mu_p/\rho_p)^{1/2}$. The ξ and ξ_p have been defined as,

$$\xi = \frac{\mu_s \Gamma_s}{\mu_l \Gamma_l}, \text{ and}$$

$$\xi_p = \frac{\mu_p \Gamma_p}{\mu_l \Gamma_l} \tag{46}$$

The second term on the right hand side of Eq. (44), which involves $\xi_p \tan(\Gamma_p h)$, is due to the third, perturbing mass layer. The dispersion equation for a two-layer system can be recovered by setting h to zero. When the substrate thickness $w \rightarrow \infty$ with Γ_s real, so that the $\tanh(\Gamma_s w) \rightarrow 1$, Eq. (44) gives the limit of a traditional Love wave perturbed by an arbitrary thickness perturbing mass layer; the Love wave solutions have $V < V_s$. Setting both the wave-guiding layer and perturbing layer thickness to zero and taking $\Gamma_s = i k_s$, where k_s is real, gives rise to the traditional SH-APM solutions which have $V > V_s$. However, by setting the third layer thickness to zero and taking $\Gamma_s = i k_s$, where k_s is real, but retaining a finite thickness wave-guiding layer it is possible to obtain solutions with $V > V_s$, thus indicating that layer guided SH-APMs can exist.

By setting a finite thickness substrate and a finite thickness wave-guiding layer, analytical results for the acoustic modes can be provided. At the start of each successive Love wave mode the phase speed of the Love wave

is $V=V_s$ and the speeds of the associated plate modes are $V_m=V_s/(1-(m\pi V_s/w\omega)^2)^{1/2}$ where ω is the angular frequency. The thickness, d_{nm}, at which a new mode appears is,

$$\frac{d_{nm}}{\lambda_l} = \frac{n}{2\sqrt{1-\left(\dfrac{V_l}{V_s}\right)^2\left[1-\left(\dfrac{m\lambda_s}{2w}\right)^2\right]}} \tag{47}$$

where $n=0,1,2,3,$ .... labels the successive Love wave modes and $m=1,2,3, ...$ labels the acoustic plate modes associated with each Love wave mode. According to equation (47), the thickness of the substrate, w, determines the number of Love wave modes and the spacing of the associated acoustic plate modes. Setting $m=0$ gives the traditional Love waves whilst acoustic plate modes correspond to $m>0$. The $n=0$ Love wave corresponds to a displacement with a single node located within the substrate and an antinode at the surface of the guiding layer. Each higher order Love wave introduces an additional node within the layered system. In the case of a Love wave, the fractional change of phase speed by increasing guiding layer thickness by an amount Δd was found to be proportional to $\omega^2\Delta d^2$, assuming the substrate is sufficiently thick compared to the perturbation, whereas for the lower order associated acoustic plate modes, it was found to be proportional to $\Delta d/w$.

Numerical results for the phase speed obtained from the dispersion equation for the two-layer system using parameters of $w=100$ μm $f=100$ MHz, $V_l=1100$ ms^{-1}, $V_s=5100$ ms^{-1}, $\rho_l=1000$ kgm^{-3} and $\rho_s=2655$ kgm^{-3} are given in fig. 2.16. The horizontal-axis has been plotted using a dimensionless parameter of the wave-guiding layer thickness scaled by $\lambda_l=V_l/f$. The guiding layer on quartz is chosen to be poly(methylmethacrylate) . The substrate thickness was chosen to enable the acoustic plate modes to be resolved in fig. 2.16. The points shown in fig. 2.16 are the start of each mode calculated using the analytical results. In fig. 2.16, each higher order Love wave mode, labelled by $n=N$ and $m=0$, arises as a continuation of the acoustic plate mode, labelled by $n=N-1$ and $m=1$, associated with the previous Love wave mode.
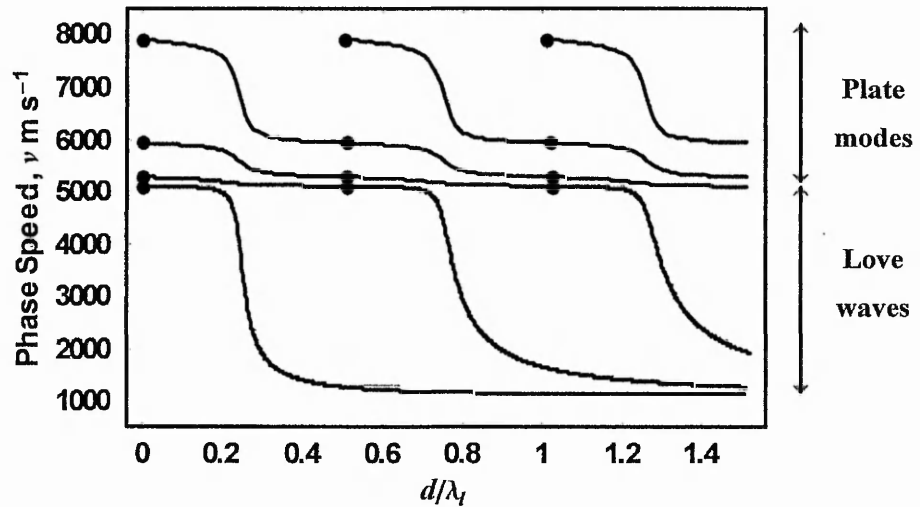
Fig. 2.16   Phase speed calculated numerically from the dispersion equation for a two-layer system of substrate and wave-guiding layer. The points are values known from analytical results. Curves with $V<V_s$ correspond to Love waves and curves with $V>V_s$ correspond to layer guided SH-APMs.

This has been confirmed by computing the displacement functions. The mass sensitivity of a Love wave device arises from the sharp change in phase speed, V, from a value equal to V_s to a value close to V_l that occurs at a wave-guiding layer thickness $d \sim (2n+1)\lambda_l/4$, where n is the integer labelling the Love wave mode. Ideally, the wave-guiding layer thickness will be chosen to place the device operating point at the transition point, $d \sim \lambda_l/4$, of the first Love wave mode, in order to operate the sensor at the maximum sensitivity point. In practise, the sensor will suffer from high signal loss, unacceptable for sensing operations. At $d \sim \lambda_l/4$, any perturbation of this wave-guiding mass layer will cause the maximum change in phase speed. In a similar manner, The form of the dispersion curve suggests the possibility that the sensitivity of a SH-APM sensor can be significantly enhanced by the use of a wave-guide layer and by choosing to place the device operating point at the transition point, $d \sim \lambda_l/4$, the SH-APM should exhibit a substantially enhanced mass sensitivity compared to a device with no wave-guiding layer.

2.4.3 Mass sensitivity

The simplest view of the effect of mass deposition on a Love wave or layer guided SH-APM sensor is by perturbing about the solution for the two–layer system. Defining the combination, $\rho_p h$, of the density and thickness of the perturbing mass layer gives the mass per unit surface area, Δm, and this allows the fractional change in phase speed, from the speed, V_o, at the operating point of the dispersion curve, to be derived as,

$$\frac{\Delta V}{V_o} \approx \left(1 - \frac{V_p^2}{V_o^2}\right) g\left(\omega, V_s, \rho_l, V_l, w, d\right) \Delta m \tag{48}$$

where the function g, is known analytically and depends only upon the substrate, guiding layer and operating frequency. From Eq (48), the sensitivity function, g, is experimentally quite significant as if determined for any perturbing layer, then it is the same function for any other perturbing mass layer. If we now consider a small extension of the perturbing mass layer as a small extension of the wave-guiding layer, a direct interpretation is that the sensitivity is intrinsically related to the slope of the dispersion curve. Defining a mass sensitivity function, S_m, we find,

$$S_m = \lim_{\Delta m \to 0} \frac{1}{\Delta m}\left(\frac{\Delta V}{V_o}\right) = \frac{1}{\rho_l}\left[\frac{1 - V_p^2/V_o^2}{1 - V_l^2/V_o^2}\right]\left(\frac{d\log_e V}{dx}\right)_{x=d} \tag{49}$$

where the mass sensitivity function, S_m, is in units of $m^2\ kg^{-1}$. The conclusion is that the sensitivity of a Love wave or a layer-guided shear horizontally polarised acoustic plate mode device to mass deposition can be determined numerically from the experimentally or numerically determined dispersion curve.

From Eq (49), the modulus of the mass sensitivity, $|S_m|$, is calculated and plotted in fig. 2.17 for the first three Love wave modes shown in fig. 2.16. In fig. 2.18 the corresponding curves for the layer-guided SH-APM modes are

shown. As predicted by Eq (49), the maximum sensitivity corresponds to the steepest slope of each mode of the dispersion curves in fig. 2.16, which, for the parameter values used for the calculations, is at a guiding layer thickness of $d \sim (2n+1)\lambda_l/4$.
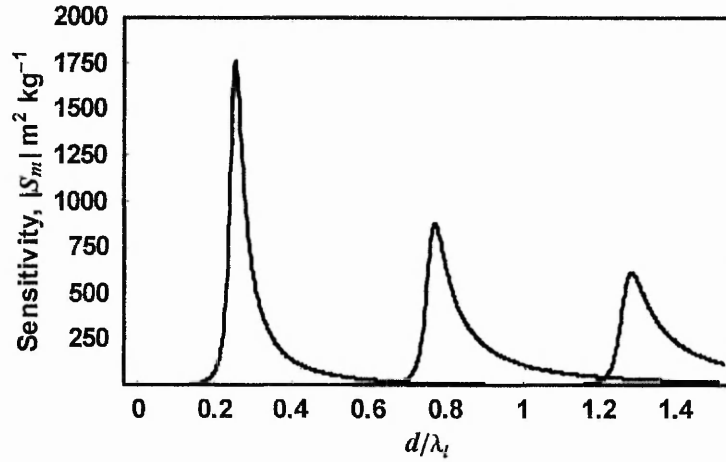
Fig. 2.17   Modulus of mass sensitivity, $|S_m|$, for the first three Love wave modes in Fig. 2.16.
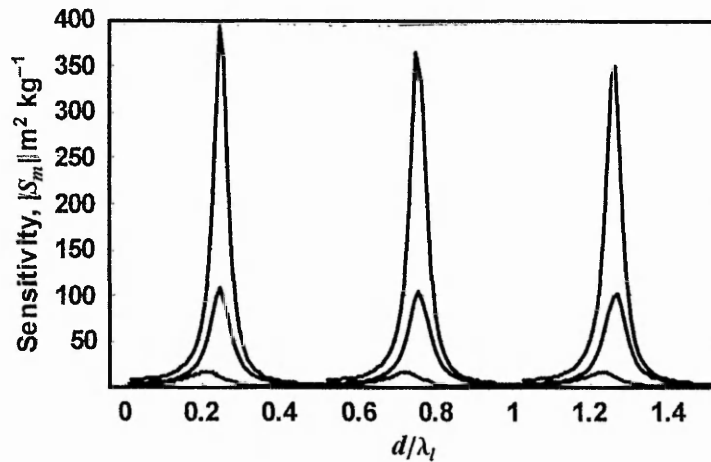
Fig. 2.18   Modulus of mass sensitivity, $|S_m|$, for the layer guided SH-APMs associated with the three Love wave modes in Fig. 2.17.

An evaluation of the analytical results for the mass sensitivities of non-layer guided SH-APM sensors gives $|S_m|$ = 3.85, 4.92 and 8.91 m^2 kg^{-1}, respectively,

for the three $m>0$ SH-APM modes (in agreement with the numerical values in fig. 2.18 in the limit $d\rightarrow0$). From fig. 2.18, it is apparent that the wave-guiding effect substantially increases the mass sensitivity of the SH-APM by more than an order of magnitude, the highest amplification in mass sensitivity corresponding to the highest order SH-APM mode and, with the parameters chosen to plot in fig. 2.16, the mass sensitivity of the layer-guided SH-APMs becomes comparable to, to within an order of magnitude, the mass sensitivity of the Love wave modes. Extensively studied in the 1980's for liquid sensing applications, SH-APM devices have since then been discounted because of their poor sensitivity compared to Love wave devices. However, the disadvantage of the Love wave sensors is that they require the transducers to be on the same face as the sensing face, which causes problems in protecting the transducers from the liquid media and sealing the sensing area. On the other hand, SH-APM sensors use the substrate as a resonator and both faces can be used separately. On one face to excite and receive the acoustic wave, on the other face to wave-guide and use for biosensing operations. This use of opposing faces would considerably simplify sealing and packaging problems.

2.4.4 Frequency Dependence of Love Wave Sensitivity

2.4.4.1 Mass sensitivity on semi-infinite substrate

From the Sauerbrey equation and the Kanazawa and Gordon equations (section 2.3.5), the sensitivity function S_m to solid and liquid for QCM sensors is proportional to the frequency for the solid and for Newtonian liquids, such as water, proportional to the square root of frequency, and, as a consequence, increasing the frequency of operation suggests an increase in the sensitivity function.

This general and simple rule is not directly applicable to Love wave sensors as the frequency dependence will depend on the chosen operating point on the dispersion curve. In the case of a finite thickness substrate and finite thickness wave-guiding layer, the frequency enters the calculation of the

wave-speed, V, through the two dimensionless combinations $d/\lambda_l = df/V_l$ and $w/\lambda_s = wf/V_s$. When the substrate is infinitely thick the layer guided SH-APMs can no longer exist and only Love waves are possible. As the phase speed for a Love wave depends on frequency only through the dimensionless combination of $z = d/\lambda_l = df/V_l$, a change in guiding-layer thickness, d, becomes equivalent to a change in operating frequency, f. Thus, Eq. (49) can be used to probe the change in sensitivity that will occur through a change in operating frequency, for a given mass perturbation, Δm, on a particular device. Dispersion curves in fig. 2.16 can then be plotted using the dimensionless variable, z, and, through z, the slope on this dispersion curve can be directly related to the slope in the dispersion curve when plotted against guiding layer thickness. In dimensionless units of guiding layer thickness, the mass sensitivity function, Eq. (49), becomes,

$$S_m = \frac{1}{\rho_l}\left[\frac{1-V_p^2/V_o^2}{1-V_l^2/V_o^2}\right]\frac{f_o}{V_l}\left(\frac{d\log_e V}{dz}\right)_{z=z_o} \tag{50}$$

Eq (50) can then be simplified by considering $V_p \ll V_o$ to,

$$S_m \approx \frac{1}{\rho_l}\frac{f_o}{V_l}\left(\frac{d\log_e V}{dz}\right)_{z=z_o} \tag{51}$$

2.4.4.2 Frequency hopping

In practise, the guiding layer thickness must be adapted to the increase in operation frequency. If the guiding layer thickness is not changed then increasing the frequency would either move the operating point down the same Love wave mode or may result in a change of mode. The sensitivity function is related to the slope of the dispersion curve. A change of mode or moving the operating point down the curve can have a dramatic impact on the sensitivity of the sensor. In fig. 2.19, the change indicated by a) which uses a change of $z_o \rightarrow z_1$ due to increasing the frequency whilst retaining the same

thickness guiding layer results in an increased sensitivity. However, the change indicated by b) which uses a change of $z_1 \rightarrow z_2$, due to increasing the frequency whilst retaining the same thickness guiding layer results in a decreased sensitivity. Changes a) and b) both involve the device to operate on the first Love mode. However, experimentally, as the wave-guiding layer thickness is increased the signal of the first Love mode becomes damped while the second Love mode dominates.

In practise, the first mode Love wave will not be available and, in this case, increasing the frequency while retaining a constant d giving the change of $z_1 \rightarrow z_2$ would produce the transition indicated by c), and so working on the second mode of the Love wave. As a consequence, this would result in a lower mass sensitivity than at the initial, lower, frequency. However, the change indicated by d) which uses a change of $z_2 \rightarrow z_3$ (and a change of mode) due to increasing the frequency whilst retaining the same thickness guiding layer results in an increased sensitivity.
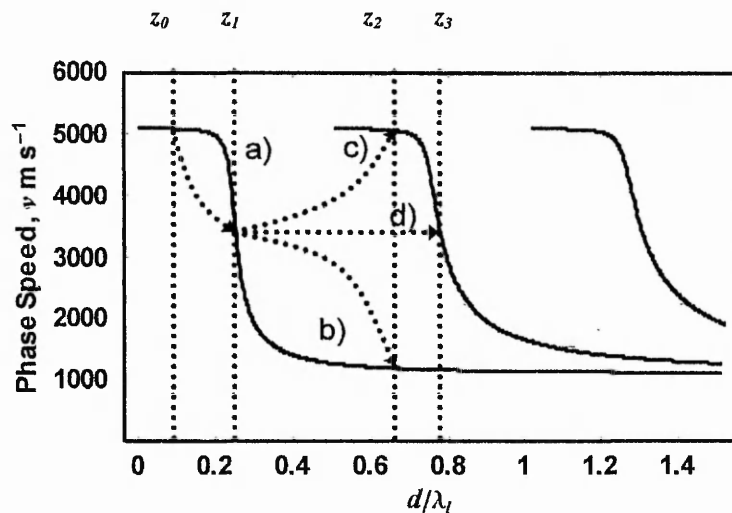
Fig. 2.19   Possible changes of Love wave operating points due to change of frequency.

As a result, the maximum mass sensitivity obtainable by changing the operation frequency while having the operating point at the maximum slope of the first mode is, by retaining the same wave-guide thickness, jumping to the

second mode of the Love wave. Thus, for the data in fig. 2.16, an increase in frequency by a factor of 3.04 gives an increase in the peak sensitivity of 1.51 rather than by a factor of 3.04, and is a direct consequence of change of modes. Similarly, a change in frequency of a given optimised device by a factor of 5.08 will move the peak sensitivity of the first mode to the peak sensitivity of the third mode and give an increase in sensitivity of only 1.77.

2.4.4.3 Optimised high frequency devices

The previous section described the possibilities to work at different frequencies by using a unique device. In practise, this is possible by using devices capable of operating at the nth frequency harmonic, the nth order of the harmonic depending on the transducers design (section 2.1).

Another possibility is to fabricate two devices operating at two different frequencies. It is then possible to adapt the wave-guide thickness to each device such that both sensors operate at the steepest slope of the first mode of the Love wave, and, as a consequence, at the same operating point on the dispersion curve. In this manner, the mass sensitivity from Eq. (51) is then predicted to increase linearly with frequency, in analogy to the QCM case. Thus, in this case, the frequency dependence of the sensitivity function S_m is proportional to the frequency for a uniform layer of mass provided the wave-guiding thickness is chosen for the optimum operating point and the same mode.

This analogy can also be rigorously extended to Love wave sensors operating in liquids, i.e. the frequency dependence of the sensitivity function S_m is proportional to the square root of frequency for a Newtonian liquid provided the wave-guiding thickness is chosen for the optimum operating point and the same mode.

2.5 Mass sensitivity of acoustic wave devices from group and phase velocity measurements

Love wave sensors involve a system with dispersion so that the phase velocity is not equal to the group velocity. Previous work established the difference between group and phase velocity on acoustic plate mode sensors [25,26], in which a relationship between group and phase velocity was derived, $\Delta f/f = (V_g/V)(\Delta V/V)$, relating the fractional frequency shift to the fractional change in phase speed due to mass deposition. Maximum sensitivity occurs at the maximum slope of the dispersion curve. High dispersion has consequences for the relationship between fractional changes in frequencies and fractional changes in phase velocity. The phase velocity, V, can be defined using the frequency and the wavelength or by using the angular frequency and the wavevector k as, $V = \omega/k$ where $k = 2\pi/\lambda$. The group velocity, $V_g = d\omega/dk$, is the slope of the (ω, k) dispersion curve. This dispersion has a significant effect when pulses are used rather than a continuous wave with a single frequency.

Physically, the phase velocity is the speed at which a particular sinusoidal wave travels. When a pulse is made by combining a number of sinusoidal waves each wave will travel with its own phase speed. In the dispersionless case, these phase speeds are all constant, independent of frequency, and the pulse therefore travels at a constant speed without altering its shape. This is the case for the Love wave when z is either small, corresponding to a thin guiding layer when the speed of the Love wave is close to the shear speed in the substrate - or large, when the speed of the Love wave is close to the speed in the layer. Between those two limits, corresponding to a region of maximum mass sensitivity, strong dispersion occurs and the pulse spreads out as it travels.

For a given guiding layer thickness, the pulse contains a spectrum of frequencies, each travelling at a phase speed of its own. In a region of strong dispersion, each frequency component sees a slightly different effective thickness $z = df/V_l$ of guiding layer, which means that the pulse effectively samples the local slope of the curve of phase speed with z. As the mass sensitivity is related to the slope of the dispersion curve, it is possible to anticipate that mass sensitivity can be probed by group velocity measurements.
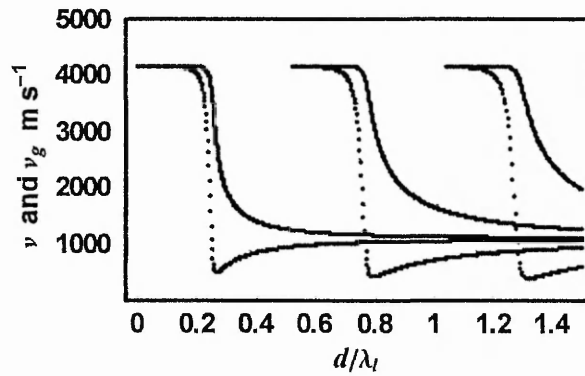
Fig. 2.20   Calculated Love wave (first, second and third modes) phase speed curves (solid lines) for an infinitely thick substrate with shear speed and density of V_s=4160 m s^{-1} and ρ_s =7456 kg m^{-3} covered by a guiding layer with shear speed and densities of V_l=1100 m s^{-1} and ρ_l =1000 kg m^{-3}. The dotted curves shows the corresponding group speeds calculated using a 0.25 μm thick guiding layer.

2.5.1 Dispersion curve

The solid curve in fig. 2.20 shows calculation of the Love wave speed, V, for the first three love modes supported by an infinitely thick isotropic substrate. The substrate shear speed and density corresponds to those of Lithium Tantalate (V_s, ρ_s), the shear speed and density of the wave-guide layer corresponds to those of PMMA (V_l, ρ_l).

Dotted lines represent calculations of the corresponding group velocity. Fig 2.20 shows the limit cases: on the first Love mode, when the operating point z is small or large, both phase and group velocities are the same. The (ω, k) dispersion curve can be calculated from the (V, z) curve using $\omega=2\pi z V_l/d$ and $k=\omega/V = 2\pi z V_l/(Vd)$ provided the ratio V_l/d of the layer shear speed to the layer thickness is known. The dotted curves in fig. 2.20 giving the group velocities are calculated for a specific layer speed of V_l = 1100 ms^{-1} and so the ratio V_l/d corresponds to a specific choice of the layer thickness, d.

2.39
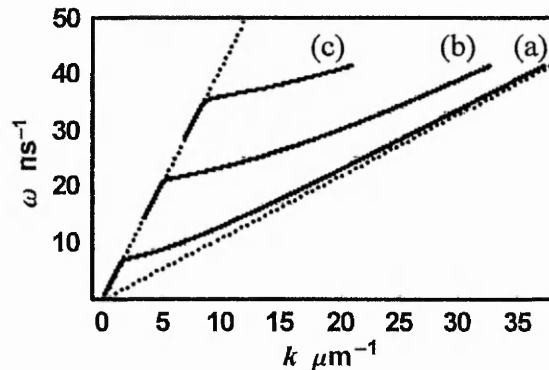
Fig. 2.21   Dispersion curves deduced from the Love mode phase speed curves in figure 2.20 using a 0.25 μm thickness guiding layer; a) first mode, b) second mode and c) third mode. The upper dotted line corresponds to the substrate shear speed of 4160 m s^{-1} and the lower dotted line corresponds to the layer shear speed of 1100 m s^{-1}.

Fig. 2.21 shows the (ω, k) dispersion curve calculated from the solid curves fig. 2.20 using d=0.25 μm, so that V_l/d=4.4×10^9 s^{-1}. The solid curves show the first three Love wave modes and the upper dotted line corresponds to the substrate phase speed of 4160 m s^{-1} and the lower dotted line corresponds to the layer speed of 1100 m s^{-1}. Fig. 2.21 confirms the relationship for a constant group speed equal to that of the substrate phase speed for small z before deviating and joining the lower dotted line representing a constant group speed equal to that of the substrate phase speed. This pattern is repeated for the second (curve b in fig. 2.21) and third (curve c in fig. 2.21) Love wave modes. As seen in fig 2.20 and 2.21, the group velocity is always less that the speed velocity, which defines a system with normal dispersion.

2.5.2 Mass sensitivity

In section 2.4, the mass sensitivity of an acoustic wave sensor has been derived (Eq 49), defined by the change in phase speed at fixed frequency,

$$S_m = \lim_{\Delta m \to 0} \frac{1}{\Delta m} \left(\frac{\Delta V}{V_o} \right),$$

where Δm is the deposited mass per unit area, V_p is the phase speed at the device operating frequency f_o and the mass sensitivity function is in units of $m^2 \ kg^{-1}$. The following relationship has been used by number of authors,

$$S_m = \frac{1}{V_o} \left(\frac{dV}{dm} \right) \qquad (52)$$

where m is the mass per unit area on the APM device surface. Eq (52) can then be re arranged by changing variables using $m = \rho_l d = \rho_l V_l z / f$ so that Eq. (52) becomes,

$$S_m = \frac{f}{\rho_l V_l} \left(\frac{d \log_e V}{dz} \right) \qquad (53)$$

By re-considering the definition of the group velocity and writing it in terms of the z-parameter assuming a constant guiding layer thickness, d, the inverse group velocity becomes $V_g^{-1} = dk/d\omega$ and since $k = \omega / V$ and $\omega = 2\pi z V_l / d$ we find,

$$\frac{V}{V_g} = 1 - z \left(\frac{d \log_e V}{dz} \right) \qquad (54)$$

Together with Eq. (53), and using the approximation that $V_p \approx V_l$, Eq. (54) becomes,

$$\frac{V}{V_g} \approx 1 - \rho_l d S_m = 1 + \rho_l d |S_m| \qquad (55)$$

Since the sensitivity function, S_m, for the Love wave is negative, Eq. (55) predicts that the group velocity will always be less than the phase velocity. This equation can also be re-arranged to give the mass sensitivity as a function of the phase and group velocities and the guiding layer thickness and density,

$$S_m \approx \frac{1}{\rho_l d}\left(1 - \frac{V}{V_g}\right) = \frac{1}{\rho_l d}\frac{\left(V_g - V\right)}{V_g}$$

(56)

Eq. (56) shows that the mass sensitivity can be expressed as a fractional deviation of the phase velocity from the group velocity divided by the mass per unit area due to the guiding layer. Fig. 2.22 shows the modulus of the mass sensitivity evaluated using Eq. (56) and the data for the three Love wave modes in fig. 2.20; a frequency of 100 MHz has been used in the calculation of fig. 2.22.
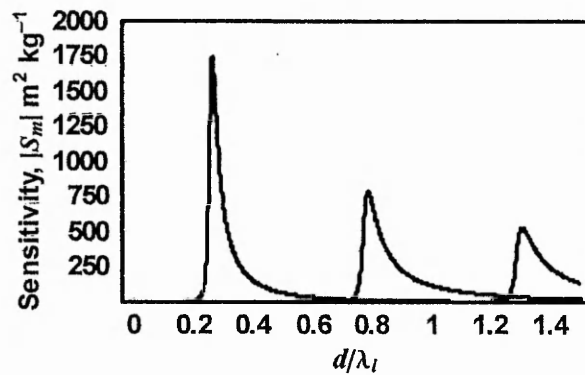
Fig. 2.22   Magnitude of mass sensitivity, $|S_m|$, evaluated from the group and phase velocities for the data in fig. 2.20 using a frequency of 100 MHz.

An interesting point is that Eq. (56) predicts that the mass sensitivity of a Love wave device can be directly evaluated by making measurements of the group and phase velocities, and can be also applied to any non-layer

guided acoustic wave sensor, including acoustic plate mode, surface transverse wave, shear horizontal surface acoustic wave and Rayleigh-SAW devices, simply by taking $\Delta m = \rho_l d$ to be the deposited mass per unit area and examining the limit $\Delta m \to 0$. Furthermore, the slope of the group velocity in figure 2.20 appears to be steeper than that of the phase velocity and one can expect the mass sensitivity based on the group velocity to be higher than that of the phase velocity. Hence, by analogy to Eq. (53) and (54), it is useful to derive a formula giving the group velocity mass sensitivity,

$$S_m^g = \left(\frac{d \log_e V_g}{d m_l} \right)_{d=d_o} = \frac{f_o}{\rho_l V_l} \left(\frac{d \log_e V_g}{dz} \right)_{z=z_o} \tag{57}$$

Teston *et al*, in their work on the mass sensitivity of acoustic plate modes [27], defined a frequency mass sensitivity, S_m^f, in a similar manner to Eq. (52) and related it to the phase velocity mass sensitivity by $S_m^f = S_m V_g/V$. Applying this formula to Eq. (57) gives,

$$S_m^f = \lim_{\Delta m \to 0} \frac{1}{\Delta m} \left(\frac{\Delta f}{f_o} \right) \approx \frac{1}{\rho_l d} \frac{(V_g - V)}{V} \tag{58}$$

From Eq. (57) and (58), the frequency mass sensitivity differs from the phase velocity mass sensitivity by whether the difference between group and phase velocities is expressed as a fraction with respect to the phase or group velocity. Since the phase velocity is always larger than the group velocity, S_m^f will be smaller than S_m, possibly by an order of magnitude depending upon the operating point. To illustrate this point, fig. 2.23 shows the ratio of group to phase velocity calculated for the data in fig. 2.20.
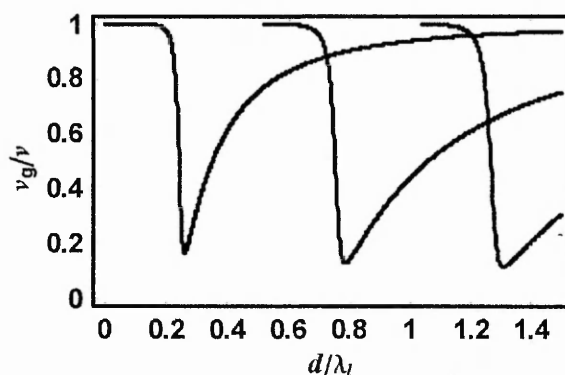
Fig. 2.23   The ratio of group to phase velocities evaluated for the data in fig. 2.20.

Section 2.4 has reviewed a new theoretical treatment of the Love wave sensors. Propagation characteristics of two separate types of sensors, Love wave and SH-APM have been described and a model has been outlined to unify those two modes. Moreover, new theoretical evidences show that the traditional SH-APM can be wave-guided similarly to the Love wave. The model shows that higher Love wave modes can be regarded as continuations of those layer guided SH-APM and, as a result, the layer guided SH-APM exhibits an enhanced mass sensitivity compared to the traditional SH-APM, whilst retaining all the advantages of operating via liquid sensing on the face which is opposite to the face with the transducers. The frequency dependence of the mass sensitivity of traditional Love wave sensors has also been examined. The relationship between the slope of the dispersion curve and the mass sensitivity has been made explicit and general rules for operating higher frequency sensors obtained. A difference in sensitivity obtainable by increasing the frequency of a given device and by optimising the wave-guiding layer of a higher frequency device has been identified. It has been shown that the peak sensitivity of a given Love wave mode obtained by optimising the wave-guiding layer thickness increases linearly with frequency when sensing uniform mass layers. Appendices A and B review in depth the mathematical developments of section 2.4.

In this section 2.5, we showed that dispersion in acoustic wave sensors is an intrinsic and important property when they are used for mass sensing.

2.44

Dispersion is particularly strong in Love wave sensors, which use this characteristic to produce high mass sensitivity. A formula relating the difference in group and phase velocities to the mass sensitivity has been derived and this formula is applicable to both Love wave and other acoustic wave sensors. Those derivations suggest that the group velocity may be a good sensor parameter.

References

[1] H. Engan, Electr. Lett., **10** (1974), 395.

[2] R. Almar, B. Lewis, E. G. S. Paige, IEEE Trans., **30** (1983), 51.

[3] G. Sauerbrey, Z. Phys, **155** (1959), 206

[4] K. K. Kanasawa, J. G. Gordon II, Anal. Chim. Acta., **175** (1985), 99.

[5] S. Bruckenstein, M. Shay, Electroch. Acta., **30** (1985), 1295.

[6] E. M. Pater, S. Bruckenstein, A. R. Hillman, J. Chem. Soc., Faraday Trans., **94** (1998), 1097.

[7] B. A. Cavic, G. L. Hayward and M. Thompson, The Analyst, **124** (1999), 1405.

[8] S. Rösler, R. Lücklum, R. Borngraber, J. Hartmann, P. Hauptmann, Sensors and Actuators B, **48** (1998), 415.

[9] G. McHale, M. K. Banerjee, M. I. Newton, V. V. Krylov, Phys. Rev. B, **59** (1999), 8262.

[10] R. W. Cernosek, S. J. Martin, A. R. Hillman, H. L. Bandey, IEEE Trans. Ultrason. Ferroelectr. Freq. Control, **45** (1998), 1399.

[11] G. McHale, R. Lücklum, M. I. Newton, J. A. Cowen, J. Appl. Phys., **88** (2000), 7304.

[12] S. Lu, A. W. Czanderna, Elsevier, N.Y 1984.

[13] R. M. White, F. Voltmer, Appl. Phys. Lett., **7** (1965), 314.

[14] B. A. Auld, J. J. Gagnepain, M. Tan, Electr. Lett., **12** (1976), 650.

[15] H. Engan, K. A. Ingebritsen, A. Tonning, Appl. Phys. Lett., **10** (1967), 311.

[16] T. I. Browning, M. F. Lewis, Electr. Lett. **13** (1977), 128.

[17] A. E. H. Love, Some problems of Geodynamics, Cambridge Univ. Press, Cambridge, (1911); New York Dover, (1967).

[18] D. P. Morgan, Surface-wave devices for signal processing, Elsevier, New York, (1991).

[19] E. Gizeli , A. C. Stevenson, N. J. Goddard, C. R. Lowe , IEEE Trans. Ultrason. Ferroelec. Freq. Control., **39** (1992), 657.

[20] M. F. Lewis, Electr. Lett. **17** (1981), 819.

[21] A. J. Ricco, S. J. Martin, Appl. Phys. Lett., **50** (1987), 1474.

[22] D. S. Ballantine, R. M. White, S. J. Martin, A. J. Ricco, E. T. Zellers, G. C. Frye, H. Wohltjen, Acoustic wave sensors, Academic Press, New York, (1997).

[23] S. J. Martin, A. J. Ricco, T. M. Niemczyk, G. C. Frye, Sensors and Actuators, **20** (1989), 253.

[24] G. McHale, M.I. Newton, F. Martin, J. Appl. Phys., Accepted Oct 2002.

[25] R.M. White, P.J. Wicher, S.M. Wenzel, E.T. Zellers, Freq. Control, UUFFC-**34** (1987), 172.

[26] S. Liew, F. Josse, D.T. Haworth, Z.A. Shana, U.R. Kelkar, M. Grunze, IEEE Ultrasonics Symposium Proceedings, **1-3** (1990), 285.

[27] F. Teston, G. Feuillard, L. Tessier, M. Lethiecq, IEEE Trans. Ultrason. Ferroelec. Freq. Control, **45** (1996), 2666.

CHAPTER 3

EXPERIMENTAL DEVELOPMENT

CHAPTER 3
EXPERIMENTAL DEVELOPMENT

3.1 Introduction

One major theme in this thesis is the development of experimental techniques and the application of those techniques to the study of the solid or liquid environment of the surface acoustic wave propagation path. This chapter reviews the photolithographic process used to fabricate shear mode surface acoustic wave devices, the methods of deposition of solid and polymer layers onto devices, the flow cell configuration and proving procedures and the development of complementary pulse and continuous signal methods for performing measurements of amplitude and phase.

3.2 Fabrication of SAW devices

3.2.1 Photolithography

Photolithography is the most critical and time-consuming process step in manufacturing integrated circuits. The primary goal of photolithography is to replicate a pattern representing an integrated circuit component on the wafer surface. This is accomplished by projecting an image of the pattern onto a photosensitive polymer layer. When developed, the latent pattern is revealed, exposing selected regions in the underlying wafer surface. With regions selectively exposed and protected, the wafer is ready for permanent production of the pattern. As the demand for more complex processors in smaller packages increases, the industry is challenging the limits of photolithography to produce smaller features without compromising image quality. The process is partially illustrated in fig. 3.1.
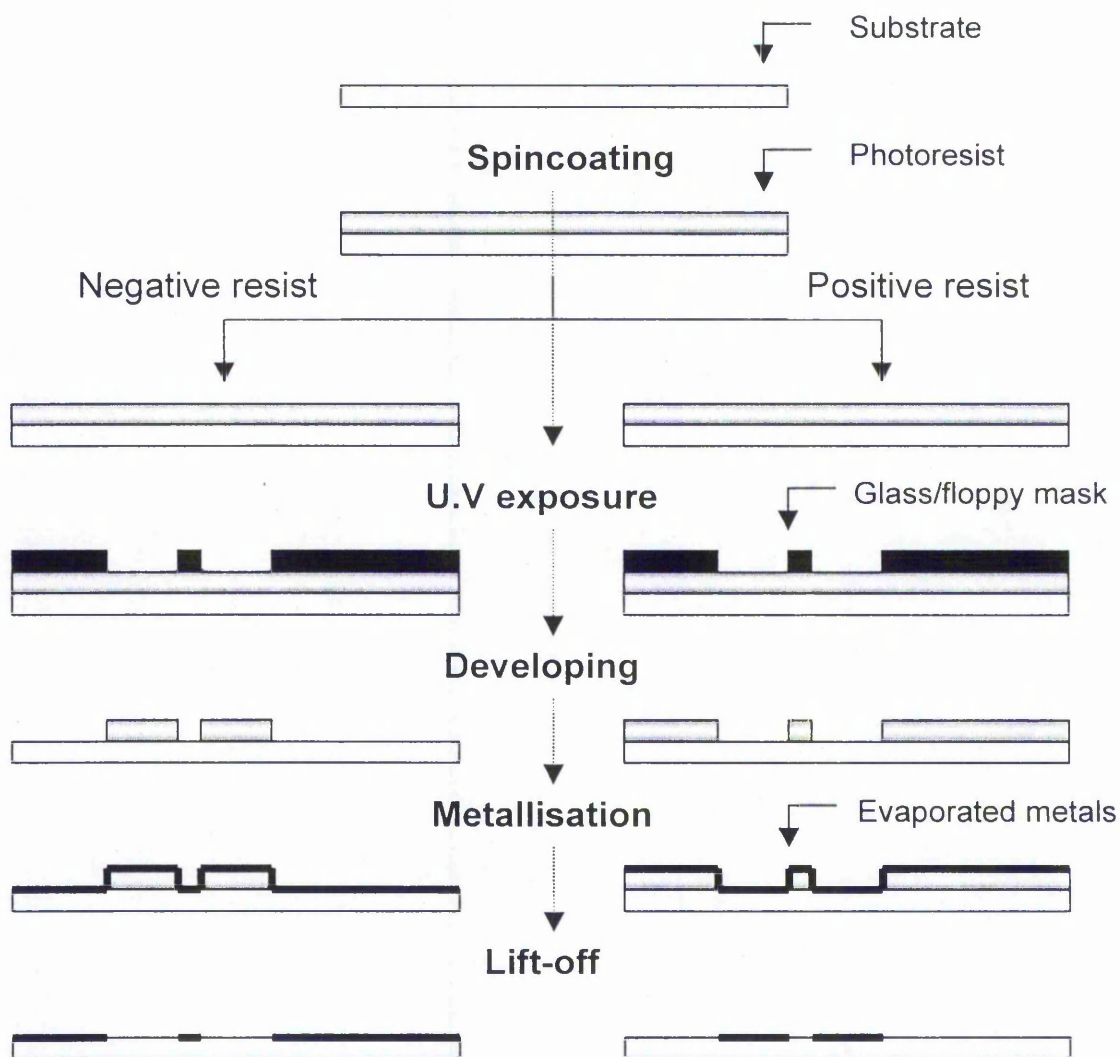
Fig. 3.1   The photolithography process with negative and positive resist.

Wafer cleaning and photoresist application

In the first step, the wafers are chemically cleaned to remove particulate matter on the surface as well as any traces of organic, ionic, and metallic impurities. After cleaning, photoresist is applied to the surface of the wafer. High-speed centrifugal whirling of silicon wafers is the standard method

for applying photoresist coatings in integrated circuits manufacturing. This technique, known as "Spin coating," produces a thin uniform layer of photoresist on the wafer surface.

Spin coating

There are four distinct stages to the spin coating process. Stage 3 (flow controlled) and Stage 4 (evaporation controlled) are the two stages that have the most impact on final coating thickness. The first stage is the deposition of the coating fluid onto the wafer or substrate. The second stage is when the substrate is accelerated up to its final, desired, rotation speed. This stage is usually characterized by aggressive fluid expulsion from the wafer surface by the rotational motion. Because of the initial depth of fluid on the wafer surface, spiral vortices may briefly be present during this stage. Eventually, the fluid is thin enough to be completely co-rotating with the wafer and any evidence of fluid thickness differences is gone. Ultimately, the wafer reaches its desired speed and the fluid is thin enough that the viscous shear drag exactly balances the rotational accelerations. The third stage is when the substrate is spinning at a constant rate and fluid viscous forces dominate fluid thinning behaviour. This stage is characterized by gradual fluid thinning. The fourth stage is when the substrate is spinning at a constant rate and solvent evaporation dominates the coating thinning behaviour. After spinning is stopped many applications require that heat treatment or "firing" of the coating be performed (as for "spin-on-glass" or sol-gel coatings). On the other hand, photoresists usually undergo other processes, depending on the desired application/use.

Positive and negative photoresist

There are two types of photoresist: positive and negative. For positive resists, the resist is exposed with UV light wherever the underlying material is to be removed. In these resists, exposure to the UV light changes the chemical structure of the resist so that it becomes more soluble in the developer. The exposed resist is then washed away by the developer

solution, leaving windows of the bare underlying material. The mask, therefore, contains an exact copy of the pattern, which is to remain on the wafer. Negative resists behave in just the opposite manner. Exposure to the UV light causes the negative resist to become polymerized, and more difficult to dissolve. Therefore, the negative resist remains on the surface wherever it is exposed, and the developer solution removes only the unexposed portions. Masks used for negative photoresists, therefore, contain the inverse (or photographic "negative") of the pattern to be transferred. The resist used during the fabrication of the devices in chapter 5 and 6 was the S1813 (Shipley Microelectr. Europe). The S1813 is a positive resist, which provides uniform defect-free coatings over a wide range of film thicknesses (500-3500 nm).

Soft-baking

Soft-baking is the step during which almost all of the solvents are removed from the photoresist coating. Soft-baking plays a very critical role in photo-imaging. The photoresist coatings become photosensitive, or imageable, only after soft-baking. Oversoft-baking will degrade the photosensitivity of resists by either reducing the developer solubility or actually destroying a portion of the sensitizer. Undersoft-baking will prevent light from reaching the sensitizer. Positive resists are incompletely exposed if considerable solvent remains in the coating. This undersoft-baked positive resists is then readily attacked by the developer in both exposed and unexposed areas, causing less etching resistance.

Mask alignment and exposure

One of the most important steps in the photolithography process is mask alignment. A mask or "photomask" is a square glass plate with a patterned metal film on one side. The mask is aligned with the wafer, so that the pattern can be transferred onto the wafer surface. Each mask after the first one must be aligned to the previous pattern. Once the mask has been

accurately aligned with the pattern on the wafer's surface, the photoresist is exposed through the pattern on the mask with a high intensity ultraviolet light.

Contact printing

In contact printing, the resist-coated silicon wafer is brought into physical contact with the glass photomask. The wafer is held on a vacuum chuck, and the whole assembly rises until the wafer and mask contact each other. The photoresist is exposed with UV light while the wafer is in contact position with the mask. Because of the contact between the resist and mask, very high resolution is possible in contact printing (e.g. 1-micron features in 0.5 microns of positive resist). The problem with contact printing is that debris, trapped between the resist and the mask, can damage the mask and cause defects in the pattern.

Development

One of the last steps in the photolithographic process is development. At low-exposure energies, the negative resist remains completely soluble in the developer solution. As the exposure is increased above a threshold energy, more of the resist film remains after development. At exposures two or three times the threshold energy, very little of the resist film is dissolved. For positive resists, the resist solubility in its developer is finite even at zero-exposure energy. The solubility gradually increases until, at some threshold, it becomes completely soluble. These curves are affected by all the resist processing variables: initial resist thickness, prebake conditions, developer chemistry, developing time, and others. The Microposit developer for S1800 series photo resists from Shipley MicroElectr. Europe was used to develop the S1813 resist. Developing rate was controlled by diluting the developer into deionised water.

Metallization of SAW devices and lift off

The Emitech K-575 is a high-resolution sputter coater, which can utilize either noble or oxidizing (such as chromium) targets. This unit utilizes a turbo

molecular pump, which is backed up by a rotary pump. The chamber size is 165 mm in diameter x 125 mm in height. Titanium and gold targets were used for the deposition of the adhesion and the ohmic layers, respectively, on the wafer covered with the imaged photoresist. The titanium target was automatically cleaned by the plasma before sputtering the devices. No break in vaccum seal was required by the process with the Emitech unit. The photoresist was subsequently removed by dipping the device into acetone and lift off in an ultrasound tank.

3.2.2 IDT designs

The starting IDT design was reproduced from a mask (glass mask with chromium patterns from RAL) in use at the Institute of Biotechnology of the University of Cambridge; this was to allow consistency with previous work. It utilised a double-double design with split fingers in order to avoid reflections and triple-transit echoes. Several variations on the design where also created to examine the effect of different frequencies and operating devices at harmonic frequencies. Table 3.1 summarizes the different designs used to fabricate the acoustic wave sensors.

The split finger design (device 1) allows devices to operate at the fundamental frequency (f_0) and the third harmonic $(3f_0)$ whereas the joined finger design has a single resonating frequency (f_0) (device 2). The surface acoustic wave delay lines were fabricated on ST-cut quartz with propagation orthogonal to the crystalline x direction, which is known to support a surface skimming bulk wave (SSBW). The first type of devices (device 1) was designed to resonate at a fundamental frequency of 110 MHz. Each IDT was of length 40λ and aperture 65λ, where the wavelength $\lambda=45$ μm. Fingers widths were 6.75 μm and spacings were 4.5 μm. The centre-to-centre distance between IDT's was 7 mm. The second type of devices (device 2), utilising the joined fingers design, was designed to resonate at a fundamental frequency of 110 MHz only. Devices 3 were designed to resonate at 309 MHz. Each IDT was of length 120λ and aperture 75λ, where the wavelength was

λ=16 μm. Finger widths and spacings were 2 μm. The centre- to-centre distance between IDT's was 6 mm. All faces of the devices other than that containing the IDT's were roughened to destroy the coherence of any reflected waves. The Ti/Au electrodes were sputtered under a vacuum of ~ 3.10^{-3} mbar. The design of device 2 was also used in the fabrication of acoustic devices on lithium tantalate (36 YX LiTaO$_3$). SSBW and leaky SH-SAWs both propagate on this crystalline direction and exhibit a very close phase velocities with 4160 m.s^{-1} and 4212 m.s^{-1} for the SSBW and leaky SH-SAW, respectively. On this substrate and crystalline orientation, the devices resonate at ~ 92 MHz.

	W (μm)	IDT Type	N	M	Mk (μm)	Sp (μm)	f_o (MHz)
Device 1	45	double-double joined	40	65	6.75	4.5	110
Device 2	45	double-double split	40	65	6.75	4.5	110/330
Device 3	16	double-double split	40	75	2	2	309/927

Table 3.1   Wavelength (W), transducers geometry, number of finger pairs (N), aperture (M), mark and space (M and Sp) and frequency of operations for the three designs on St-cut quartz.

3.2.3 Conversion from SSBW/SH-SAW to Love wave

To convert a SSBW or SH-SAW device into a Love wave device a polymer wave-guiding layer was deposited on top of the device surface; this layer had a shear acoustic speed less than that of the substrate. Flatness and homogeneity of the wave-guide layer are required. This is achieved by spin coating the liquid polymer on the device. Successive layers of S1813 photoresist (Shipley MicroElec.) and PMMA (Aldrich) photoresist were spun

on SSBW and leaky SH-SAW devices. To obtain thin layers down to a tenth of a micron, the photoresists were diluted in 2-EEA (Aldrich) and subsequently spun at different speeds. The speed of the spin coater was chosen to give optimum flatness and homogeneity to the coating. It then needs to undergo a cross-linking process. Cross-linking is physically linking chains of a polymer molecule by means of a chemical process that inserts molecular links or bonds between points along the chains. The physical interference between the cross-linking molecules and the polymer chains allows less movement of the chains, making the overall substance more solid. It has the side effect of desensitising the polymer to white light and hardening the polymer. This operation is achieved by heating the coated device at 200 °C in an oven during 1 hour.

3.3 Sensing procedures

A range of sensing experiments were carried out covering solids, polymers and liquids. The polymers (photoresists) were deposited using spin-coating in a similar manner as for the conversion of the SSBW and SH-SAWs to Love waves, although in some cases the hard-baking step was omitted. The solid and liquid sensing experiments used thermally evaporated films and a flow cell, respectively.

3.3.1 Evaporation

To obtain a thin-uniform coating of gold and tin, one must spray or evaporate it from a liquid form. Gold melts at 2807 °C and tin at 2270 °C but will not evaporate at atmospheric pressure. Thus, a low pressure is required. Fig. 3.2 shows the schematic diagram of the system used. Evaporation system requirements are a large vacuum chamber (called a bell jar) to hold many wafers, and instrumentation to heat gold and tin and to measure the vacuum and other factors to achieve uniformity. An Edwards 306

evaporation system was used for the deposition of thin films on the SH-SAW devices. The vacuum in the Edwards 306 unit is generated using a rotary pump for the rough vacuum and diffusion pump for the high vacuum.
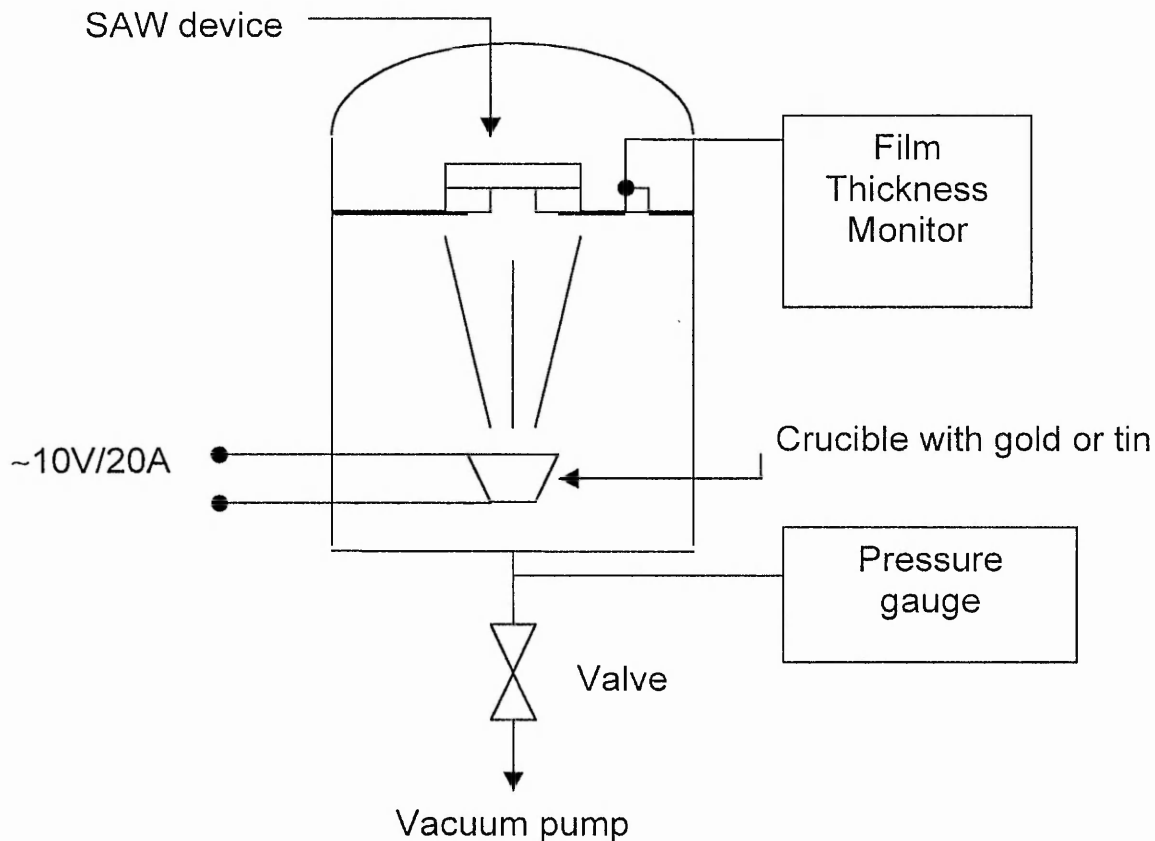
Fig. 3.2   Schematic representation of the metal evaporation system.

For evaporation, the unit was usually operated at a pressure of 10^{-6} Torr. Pressures were monitored for rough and high vacuum with a Pirani and a Penning gauge, respectively. The vacuum chamber consisted of a glass bell jar with feed through's for data cable to the film thickness monitor. For the evaporation of gold and tin, the metals were kept in a crucible held by pods. By applying a power of approximately 10V/20A, the crucible was heated up and resulted in sublimation of gold and tin in the crucible. SAW devices were mounted in a metal holder and affixed with a mask, which protected the

electrodes and allowed the metal in vapour to contact the path length only. The sensor for the film thickness monitor based on microbalance oscillator was positioned next to the substrate at the same height. The Edwards 306 multi-turret evaporator equipped with a FMT 5 thin film monitor mounted on a 5 MHz microbalance oscillator crystal was used to control the film thickness of evaporated gold and tin. The thin film deposition monitor was used to provide continuous rate and thickness data.

3.3.2 Flow cell arrangement

Fig. 3.3 shows a mounting scheme that allows sensing to take place using the propagation path on the transducer side of the SH-SAW devices. The electroded face of each device was mounted on a silicone rubber seal, which serves to accommodate any mismatch in thermal expansion between the cell and the quartz device. The seal also dampens SH-SAW vibrations at the boundaries, thus reducing acoustic reflections from the substrate. Electrical contact was made between the transducer pads and BNC connectors via gold-plated spring-loaded pins attached to the device holder. Liquid is held in contact with the sensing surface by a perspex cell, which is sealed by screws to the rubber. The liquid was drawn through the cell by a peristaltic pump.

3.4 Measurement configurations

Prior to the work in this thesis, researchers at the Institute of Biotechnology had performed biosensing experiments using Love wave devices and a network analyzer to measure phase and amplitude of the signal.

Liquid Inlet — — Liquid outlet
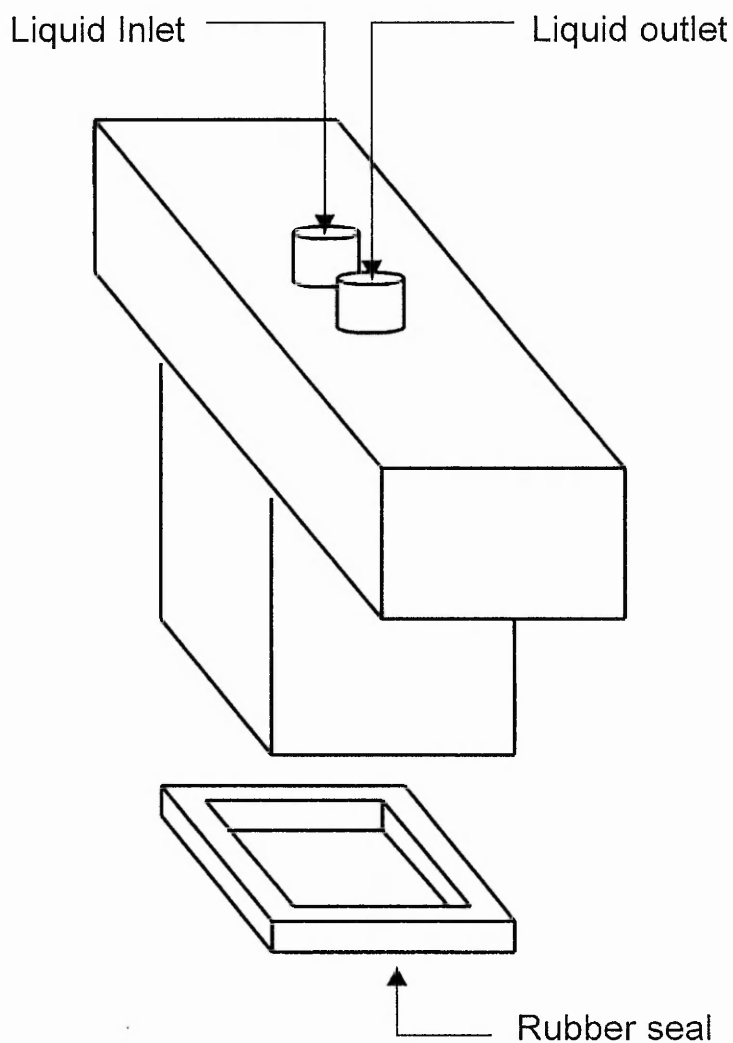
Fig. 3.3   The flow cell and silicon rubber seal which holds the liquid in contact with the sensor.

That measurement system was relatively slow and did not show time resolved information relating to the propagation path. The network analyzer was used as a continuous wave system and measurements contained the single transit signal, triple transit echoes and other unwanted signals from edge reflections. One aim of this thesis was the development of an alternative arrangement for biosensing providing time-of-flight resolved information, which could identify spurious reflections, discriminate between different acoustic modes and which

could be used to improve the sensitivity of devices. In addition, it was hoped that the system would provide rapid interrogation to provide potential for experiments on systems with fast dynamics reactions.

3.4.1 Pulse mode system

The novel system developed in this thesis uses a pulse excitation technique to monitor both amplitude and phase changes due to changes in mass or liquid loading occurring in the propagation path of a device. The system is described in fig. 3.4. A continuous RF signal was power-split and one output fed to two cascaded double balance mixers combined with a pulse generator synchronized to an external clock source.
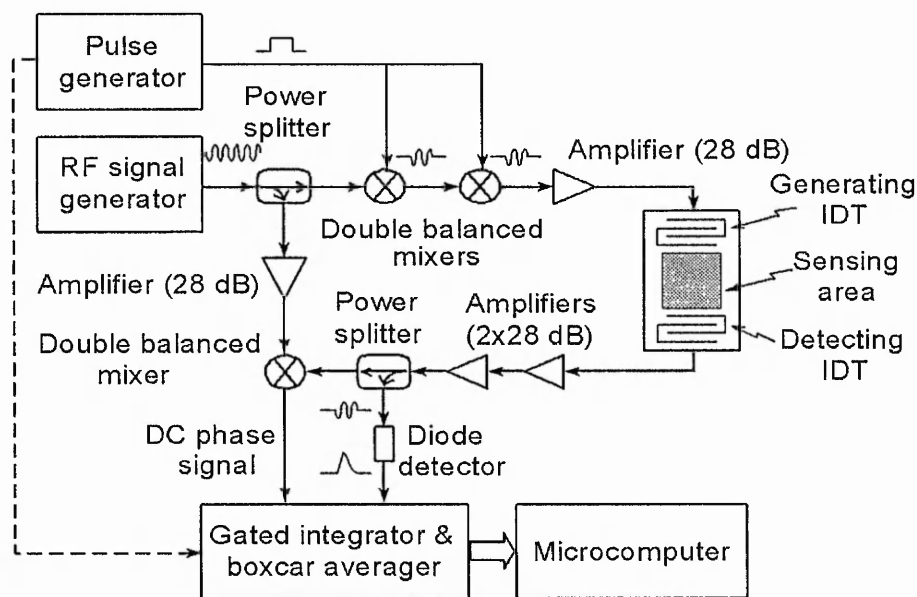
Fig. 3.4   Schematic representation of the pulse mode system.

The input was amplified and used to excite the input port of the SAW device. The output of the SAW was then amplified twice, divided with a second power splitter and one output passed by a HP8471D diode detector. The phase measurement system utilizes the other signals from the two power splitters.

The first signal is a continuous RF signal and the second the acoustic wave device pulsed output. These are fed to a third double balanced mixer set as a phase detector. The output of this phase detector includes a DC component that, for the duration of the pulse, is proportional to the phase difference between the two inputs. The gated integrator and boxcar averager (Stanford Research Systems) provided a continuously varying analogue output. The data capture rate is constrained only by the GPIB interface used to transfer data to the computer.

3.4.2 Description of the electronic components

The system was set up using the following components:

- **Controller unit PC**

- **Lecroy 9362C 1.5 GHz oscilloscope** : this oscilloscope has a frequency range 10 kHz to 1.5 GHz, is an integrated and powerful system providing the capability to capture fast signal events with high resolution and view data. The oscilloscope can zoom and analyse signals and has a powerful processing system and math packages.

- **Double Balanced Mixers (DBM's) ZFM4, Mini Circuit**: the DBM ZFM-4 is a 3 port device operating within a frequency range of 5 MHz to 1250 MHz. The function of a mixer is to convert RF energy at one frequency to a second frequency. The second function of the DBM is phase change detector. If the signals applied to the RF and Lo ports have the same frequency, the resulting voltage has a DC component that is proportional to the phase difference between the two input signals.

- **RF-Amplifiers AMC-182, MA-COM Inc**: these gain amplifiers have a frequency range of 10 kHz to 1 GHz.

- **Diode detector HP 8471D, Agilent**: this consists of a Schottky-barrier microwave diode. The circuit has a microwave input port and a video output port. The function performed by the diode is simple rectification. The frequency range of the detector for rectifying RF-signals is between 100 kHz and 2 GHz.

- **Lecroy 9210 pulse generator**: the 9210 is a high resolution 300 MHz programmable pulse generator with a 12-Bit ADC and timing accuracy to <0.5%, equipped with two 250 MHz variable edge output modules.

- **10 kHz-1 GHz signal generator 20220D, Marconi Instruments**: the Marconi 2022D is a synthetised signal generator having a frequency range of 10 kHz to 1 GHz and providing comprehensive amplitude, frequency and phase modulation facilities with an RF output level of −127 dBm to +13 dBm. Microprocessor control allows programming by the GPIB.

- **Boxcar power supply and display, computer interface, gated integrators and boxcar averagers, Stanford Research Systems Inc**: the SRS Boxcar Averager System SR250 is a modular instrumentation system designed to acquire and analyse fast analog signals. The system consists of a compatible mainframe and modules, which can be selected to tailor a system matched to individual requirements. The system is flexible enough to handle gate widths from 100 ps to 150 ms, repetition rates from a fraction of a Hertz to 50 kHz, and output to computers or chart recorders. The SR250 has low-noise inputs, low-drift outputs, and is flexible and modular. Gated integrators and boxcar averagers are designed to recover fast, repetitive, analog signals with time scales of 100's of picoseconds to 100's of microseconds. In a typical application, a time "gate" is generated characterized by a set delay from an internal or external trigger and a certain width. A gated integrator amplifies and integrates the signal that is present during the time the gate is open,

ignoring noise and interference that may be present at other times. Boxcar Averaging refers to the practice of averaging the output of the gated integrator over many shots of the experiment. Since any signal present during the gate will add linearly, while noise will add in a "random walk" fashion as the square root of the number of shots, averaging N shots will improve the signal-to-noise ratio by a factor of $\sqrt{N}$.

3.4.3 Continuous wave system

This system consists of an RF network analyser (NA) and is described in fig. 3.5.
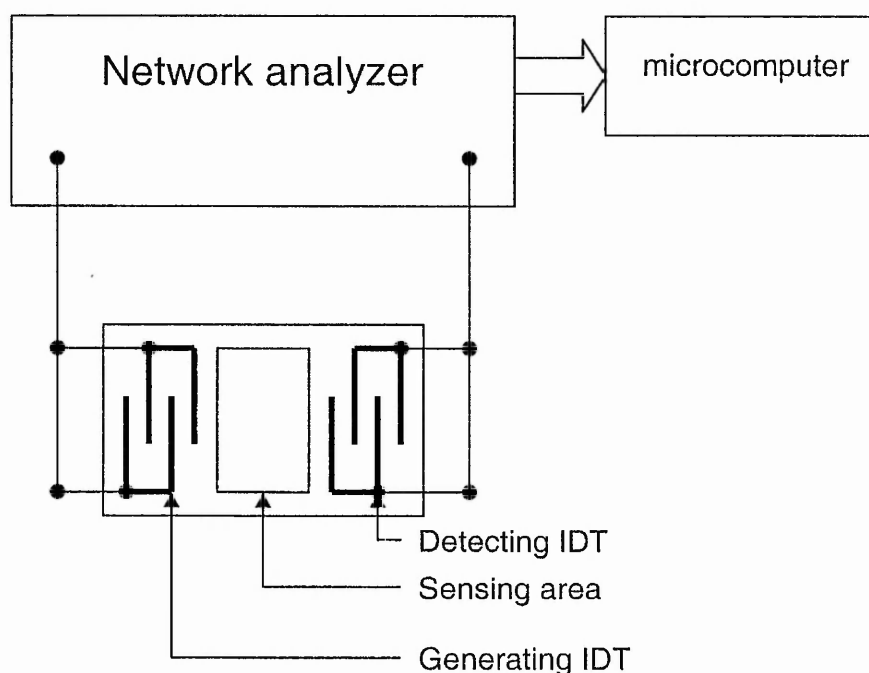
Fig. 3.5   Schematic representation of the continuous wave (CW) system.

The Agilent 8712ET features a built-in transmission/reflection test set with a full range of magnitude and phase measurements. Two independent channels can measure and display two device parameters, such as transmission and

reflection response, in a variety of formats including complex impedance, SWR, and delay, on rectangular, polar or Smith-chart displays. The output of the NA was connected to one of the electrodes of the SAW device. The signal received by the opposite electrode after a delay time τ is fed into the output of the network analyzer. The network analyzer measures the phase ϕ and total attenuation L_{DB} of the received signal relative to its output signal. Both quantities were read out and stored in a personal computer, which also controlled the network analyzer to alternately perform measurements at the different frequencies.

3.5 Calibration procedures

3.5.1 Thickness calibrations

3.5.1.1 Transducer thickness calibration

One factor that limits the performance of surface acoustic wave devices is the loading of the surface wave by the metal transducer electrodes and this is particularly important on weak coupling materials such as ST-cut quartz used for the SSBW mode. Hence, particular attention was paid to the electrode thickness. The electrode thickness was measured by using a Veeco Dektak 3 Surface Analysis System with an accuracy of 5%.

3.5.1.2 Polymer thickness

SAW devices were spin-coated with a polymer layer both for wave-guiding and for testing the device sensitivity to deposited layers. The polymer layer thickness was measured by using a Veeco Dektak 3 Surface Analysis System. Although the spin-coating process ensures excellent flatness and uniformity, a small error on the calibration is inevitable. The impact of guiding layer thickness will be further discussed in chapter 4.

3.5.2 Amplitude and phase measurement calibrations

3.5.2.1 Continuous wave system

The HP 8712ET network analyser gives direct readings in phase and amplitude in degrees and dB, respectively. The data was monitored and collected via a Labview program via a GPIB bus.

3.5.2.2 Pulse mode system

The amplitude calibration was carried out by placing a set of known attenuators into the signal path after the SAW device. The reduction in amplitude due to the sensing experiment could be compared to the equivalent attenuation in dB. Calibrations were carried out at the start of each biosensing experiment. A set of six attenuators with fixed attenuation were used: 2.9 dB, 5.9 dB, 8.9 dB, 12.9 dB, 17dB and the change in mean values from the boxcar were recorded; several attenuators were cascaded to provide higher attenuation of the signal. Attenuator values were then tabulated with mean values from the boxcar, and a best-fit conversion was extracted. By employing a polynomial series (see Fig. 3.6 (a) and (b)), an estimation of the coefficients for the polynomial series was found.

To provide a simple phase calibration for the pulse mode system prior to the sensing experiments, an experiment was devised using solutions of 3,350 molecular weight poly (ethylene glycol) (PEG) at different concentrations in the following sequence (in gram per litre); 34.4, 68.8, 103.2, 137.6, 172.0, 206.4, 240.8 and 275.2. Fig. 3.7 (a) and Fig. 3.7(b) show the CW and pulse system amplitude and phase measurements for this sequence, respectively; it should be noted that the graphs are for two distinct experiments. The PEG solutions and deionised water were alternately pumped over the device surface. The initial baseline signal with deionised water changed rapidly when replaced by the PEG solutions. When deionised water is once again pumped over the device surface, the signal returns to its

original value, showing that the PEG is fully removed. This sequence was repeated many times and shown to produce repeatable changes in phase and amplitude using the pulse mode system and the continuous mode system. The two methods were found to be in agreement to within 10%.

3.6 Summary

In this chapter, SAW sensor design considerations and their fabrication technique have been presented. Procedures for elastic mass, visco-elastic mass and liquid loading sensing on SH-SAW sensors has been developed, and will be applied to the investigation of the sensitivity of Love wave devices (chapter 4). The network analyser is the interrogation method most widely used for SAW sensors, particularly for bio (chemical) sensing applications. However, this technique is limited by its execution speed. This chapter developed and provided an overview of the capabilities of a new pulse mode system. The pulse mode system would provide a fast, selective and highly sensitive technique, and would allow rapid reactions to be observed. In chapter 5, Love wave liquid and bio (sensing) will give a rigorous experimental base for the comparison between the two techniques. The pulse mode system is a highly dispersive time-domain method and chapter 5 will also investigate the effect of dispersion on the Love wave mass sensitivity by group and phase velocity measurements.
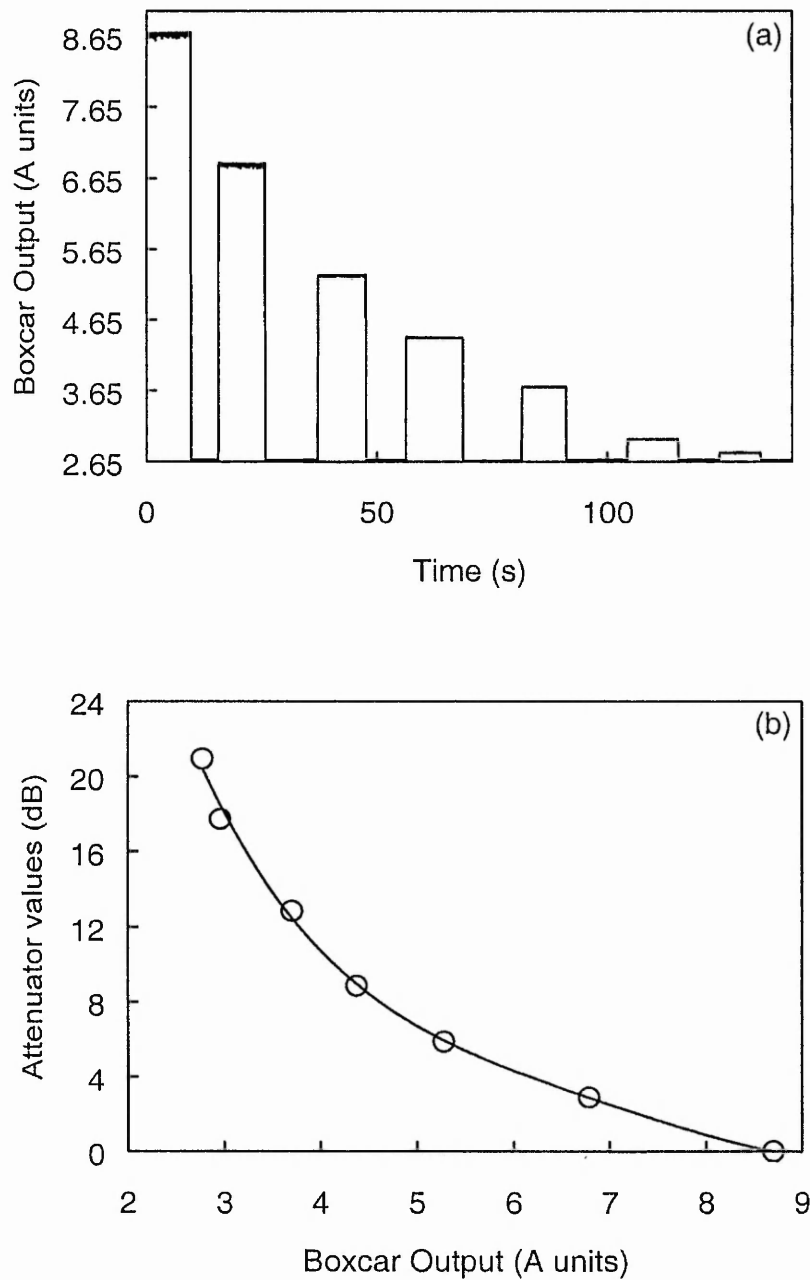
Fig. 3.6 The calibration converts the analogue output of the boxcar into acoustic attenuation. In (a), the graph shows seven calibration points for the single transit signal when cascading the four attenuators in several combinations. The solid line in (b) is the logarithmic power series fit to approximate the course of the calibration points.
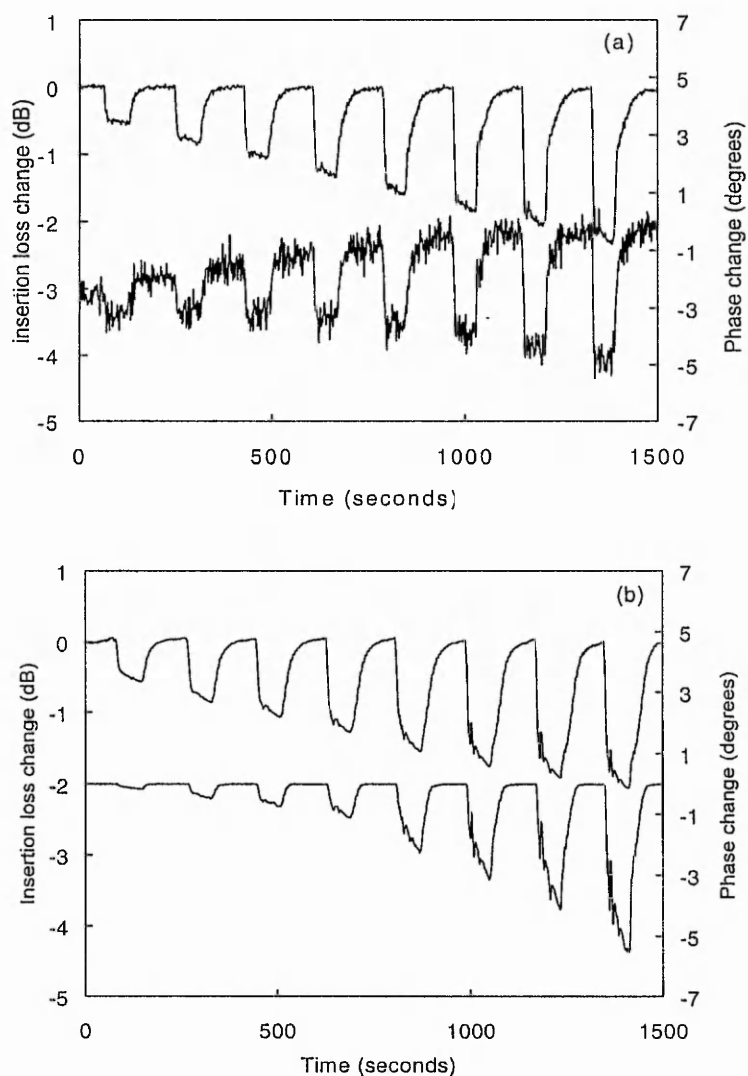
Fig. 3.7 Change in insertion loss (upper line) and in phase (lower line) for a sequence of different concentrations of 3.350 molecular weight poly(ethylene glycol) solutions by using (a) a 8712ET network analyzer and (b) the pulse mode system.

CHAPTER 4

LOVE WAVE MASS SENSITIVITY

CHAPTER 4
LOVE WAVE MASS SENSITIVITY

This chapter initially considers the effect of guiding layer thickness on Love waves produced from both the fundamental and third harmonic of an SSBW mode on quartz. The guiding layer thickness is taken through a large range so that multiple Love wave modes can be investigated. Subsequently, the equivalent experiments on lithium tantalate are presented to allow a comparison of the differences in Love waves generated from a SH-SAW mode. The chapter then considers the insertion loss mass sensitivity of quartz based Love wave devices with a focus on using multiple Love wave modes. Results are reported for ideal mass layers of gold and tin, solid viscoelastic layers of soft-baked photoresist and solutions of poly(ethylene glycol) with a range of molecular weights.

4.1 Resonant conditions for Love wave guiding layer thickness

4.1.1 Surface skimming bulk waves (SSBWs) on ST-cut quartz

The devices used in this chapter consisted of split finger (double-double) interdigital transducer (IDT) design. Devices were fabricated on ST-cut quartz with propagation orthogonal to the crystalline x-axis, which is known to support a surface skimming bulk wave (SSBW), and designed to resonate at fundamental frequency of 110 MHz (devices 2) and 313 MHz (devices 3). With an appropriate IDT metallization thickness, devices of design 3 also resonates at the third harmonic (330 MHz and 939 MHz respectively) [1]. Coating the SSBW device with a suitable overlayer allows a Love wave to be excited at either the fundamental or third harmonic frequency. The guiding layer consisted of spin-coated S1813 resist

(MicroElectr. Shipley) diluted into 2-EEA. After deposition, the resist films were hard-baked at 130ºC for 30 min to ensure extra hardness of the film. The insertion loss and resonant frequency of the devices were measured using an Agilent 8712ET network analyser, and plotted against the dimensionless parameter $z=d/\lambda_{IDT}$, where d is the film thickness and λ_{IDT} is the transducers wavelength. In fig. 4.1 a), the frequency spectrums of the device are showed at z=0 (solid line) and z=0.025 (dotted line). At z=0.025, the Love wave is recognizable by the frequency shift and the change in insertion loss. The transducers wavelength for devices 2 and 3 at the fundamental frequency was $\lambda_{IDT}=45$ µm, and $\lambda_{IDT}=16$ µm, respectively.

In fig 4.2 b), insertion loss (circles) and resonant frequency (triangles) are shown as a function of z for devices 2, resonating at the fundamental frequency of 110 MHz; the insertion loss is the change from the loss for the uncoated device. A wave-guiding amplification effect can clearly be seen with an initially improved signal. The lowest insertion loss, due to the guiding effect occurs at z=0.025. Beyond this thickness, the insertion loss increases (worse signal). However, the frequency also continues to decrease with increasing overlayer thickness until at z=0.06 a clear suppression of the signal is observed corresponding to both a large frequency decrease and a substantial loss. This pattern is further repeated in a periodic manner and four clear minima in the loss and frequency were observed before the noise became too large. The average z between two successive minima was 0.12 corresponding to an overlayer thickness $d \sim 5.4$ µm and the thickness for the first minimum was 2.7 µm.

In fig. 4.2, insertion loss (circles) and resonant frequency (triangles) as a function of z for the harmonic of devices 2 operating at 330 MHz are shown. The dimensionless parameter z is now calculated with $\lambda_{IDT}=15$ µm as the device was operating at three times the fundamental frequency. Assuming the intrinsic shear acoustic speed of the overlayer is independent of the frequency, the acoustic wavelength in the overlayer will also be one third that occurring when the device is operated at the fundamental frequency. Hence,

by plotting the loss and the operating frequency as a function of z, the minima in fig. 4.2 and 4.1 b) should match.

a)

b)

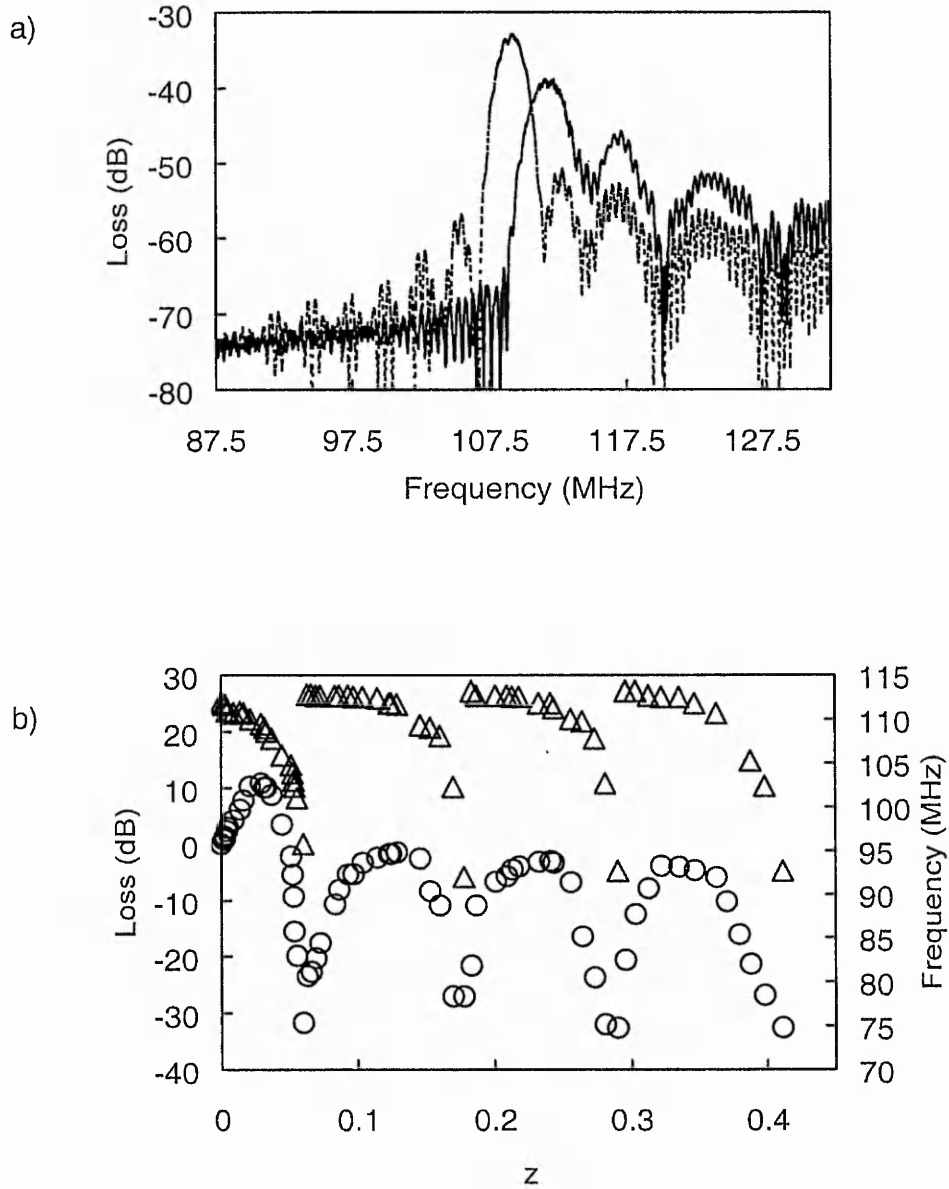**Fig. 4.1**   a) Spectrums of device 2 taken at z=0 (solid line) and z=0.025 (dotted line) respectively, b) Insertion loss (circles) and resonant frequency (triangles) for a device operated at the fundamental frequency 110 MHz as a function of z.

This is reflected in fig. 4.2 in the positions of the minima and the initial amplification which now occurs at $z=0.022$, i.e an overlayer thickness d of 0.35 μm. The periodic pattern in the frequency shift is clearly observable with a period in z of 0.12, which is identical to that of the fundamental. A series of related maxima and minima can also be observed in the loss although the exact shape is different to that observed at the fundamental frequency.

Devices 3 were designed to resonate at a fundamental frequency of 313 MHz ($\lambda_{IDT}=16$ μm). After optimisation of the IDT thickness, they also operated at the third harmonic at a frequency of 936 MHz ($\lambda_{IDT}=5.3$ μm). Devices 3 were subsequently coated with S1813 resist diluted into 2-EEA. Fig. 4.3 shows the loss (circles) and resonant frequency (triangles) as a function of the dimensionless parameter $z=d/\lambda_{IDT}$, where d is the overlayer thickness and λ_{IDT} is the transducers wavelength, for operation at the fundamental frequency of 309 MHz. A series of four resonant patterns was observed, with minima periods of $z=0.12$ consistent with those observed for devices 2 in fig. 4.1 b) and 4.2. In fig. 4.4, at the 936 MHz third harmonic, the amplification due to the guiding effect was found with a maximum in the transmission (better signal) at $z=0.025$, corresponding to an overlayer thickness of $d \sim 0.13$ μm. However, due to high noise level and strong attenuation, no further minima were obtained at the third harmonic.

The solution of the dispersion equation from Love wave theory [2] predicts a series of modes with the first Love wave mode corresponding to a displacement with an antinode at the top surface of the layer and a single node located in the substrate close to the interface with the overlayer. The next higher order mode also has an antinode at the overlayer surface, but two nodes with one located within the layer and one located in the substrate close to the interface with the overlayer. Subsequent higher order modes introduce additional nodes within the overlayer. Equating the period in the overlayer thickness to one half of an acoustic wavelength gives an estimated acoustic speed in the overlayer of 1150 m s^{-1}, which is consistent with shear acoustic speeds in most of the polymers [3].
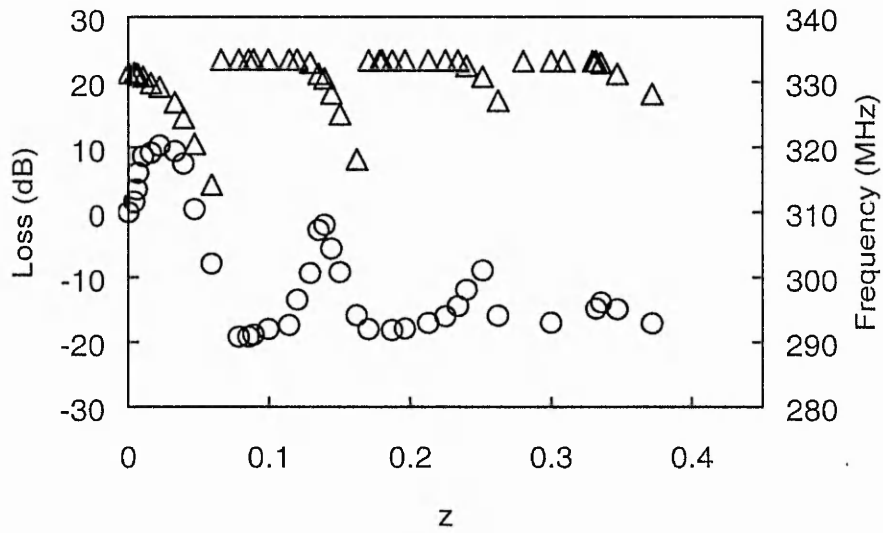
Fig. 4.2   Insertion loss (circles) and resonant frequency (triangles) for a device operated at the third harmonic frequency 330 MHz as a function of z.
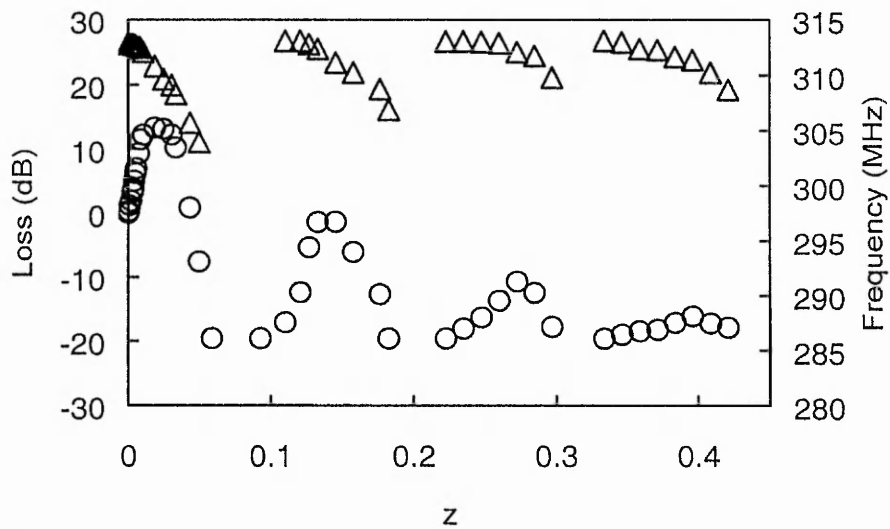
Fig. 4.3   Insertion loss (circles) and resonant frequency (triangles) for a device operated at the fundamental frequency 313 MHz as a function of z.
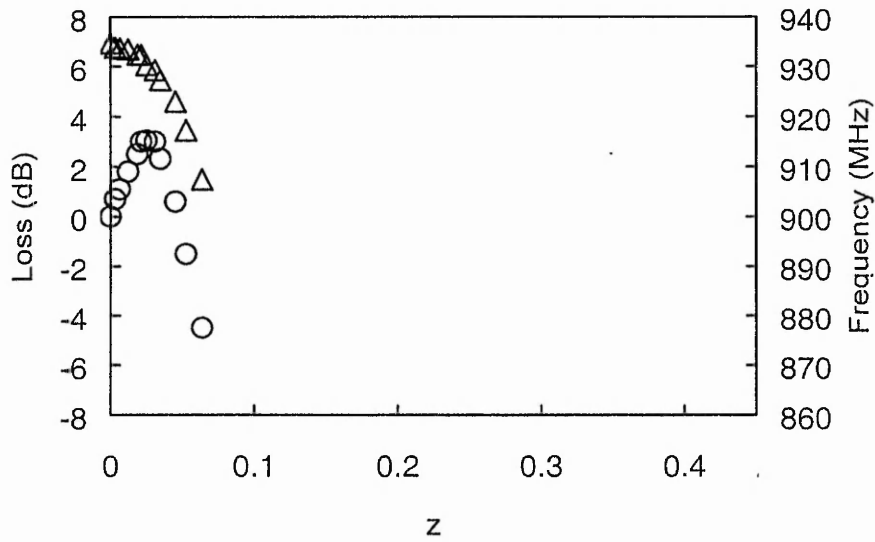
Fig. 4.4   Insertion loss (circles) and resonant frequency (triangles) for a device operated at the third harmonic frequency 936 MHz as a function of z.

Section 2.4 gave theoretical computations about the normalized layer thickness at which the next higher order mode is expected. However those transitions were plotted against a wave-guide layer thickness normalized to the wavelength of the shear wave in the layer, namely λ_l. If we re-define the x axis in fig. 4.1 b) and 4.2 as d/λ_l, the sharp transition are experimentally found to occur at $d/\lambda_l \sim 0.25$, 0.79 and 1.30 for the first, second and third Love mode, in good agreement with theoretical prediction giving sharp transitions at 0.25, 0.75 and 1.25. The deviation is within the error in the wave-guide layer thickness calibration.

The insertion loss behaviour indicated by fig. 4.1 b) is not accurately predicted by Love wave theory. The Love wave theory does not predict any substantial signal improvement when the shear wave is converted into a Love wave. However, the Love wave theory is valid for pure shear waves or pseudo pure shear waves as Bleustein-Gulyaev waves or Leaky-SH-SAWs [4]. In this experiment, a surface skimming bulk wave (SSBW) has been converted into a Love wave. Although considered as a shear wave, the SSBW is launched with

an angle from the emitting transducer, which means that the maximum power from the radiation pattern is not received by the detecting IDT [5,6]. Initially, as an increasing fraction of the wave is trapped inside the waveguide, the power transmission to the detecting IDT is improved and, despite the intrinsic loss of the polymer, the loss is decreasing. By further increasing the wave-guide layer thickness, substrate motion is reduced and once the wave is fully localised into the guiding layer, the damping of the polymer is expected to become effective and the loss to increase. The difference between the shape of the insertion loss curves in fig. 4.1 b) and fig. 4.2 is probably the result of the resonating pattern of a second acoustic mode with an acoustic velocity close to that of the SSBW. As a consequence, at the fundamental, this second mode has its peak in the SSBW bandwidth. However, at the third harmonic a smaller bandwidth allows the discrimination of the two modes.

Later in this thesis, this mode is identified as a shear horizontal acoustic plate mode (SH-APM). The resonating patterns suggest that acoustic plate modes can be guided in a similar fashion as the Love wave. ST-cut quartz with propagation orthogonal to the crystalline x-axis supporting a SSBW was used. The observed insertion loss behaviour with systematic increasing polymer overlayer, which was not predicted by the Love wave theory, motivated a study of LiTaO$_3$, which possesses a pure SH-SAW mode in addition to an SSBW mode.

4.1.2 Leaky SH-SAWs and SSBWs on 36° YX-LiTaO$_3$

Surface skimming bulk waves (SSBWs) and leaky SH-SAWs both propagate on 36° rotated Y-cut X propagating Lithium Tantalate (36YX.LT, LiTaO$_3$) [7]. In this crystalline direction the two modes exhibit a very close phase velocities with 4160 m s^{-1} and 4212 m s^{-1} for the SSBW and leaky SH-SAW, respectively. The leaky SH-SAW mode is converted into an SSBW when the propagation surface is free whereas it propagates as a leaky SH-SAW when the propagation surface is metallised. The SH-SAW that propagates on the metallised surface is affected by the mechanical properties

of the adjacent liquid. On the other hand, the SH-SAW that propagates on the free surface is affected by both the mechanical and electrical properties of the adjacent liquid [8-11].

Quartz has a relatively small piezoelectric coupling coefficient and as a result a number of workers have produced Love-wave devices using materials with greater coupling strength, such as lithium tantalate. Freudenberg *et al* reported the use of a SiO_2 guiding layer on 36° rotated Y-cut X propagating $LiTaO_3$ [12] and Barie *et al* coated a $LiTaO_3$ device with a series of polymethylsiloxane co-polymers, resulting in reversible, reproducible signals and high long-term stability [13]. Love wave devices fabricated on a $LiTaO_3$ substrate have also been applied as biochemical sensors in liquid. Low level detection at high frequency was achieved by Welsh *et al* [14] and, more recently, by Josse [15] and Bender [16]. In sensor based work, there appears to have been little explicit recognition of the existence of both an SSBW and a SH-SAW mode or of possible differences in Love waves generated from these modes.

Devices of design 2 were fabricated on lithium tantalate. The basic SAW device supports the excitation of SSBW and leaky-type shear-horizontal modes by the IDTs with a center frequency f_o at around 92 MHz and an insertion loss of approximately 22 dB. Guiding layers consisting of S1813 photoresist (Shipley MicroElec. Europe) were spun at 4000 rot/min and cross-linked during 1 hour at 200 $^\circ$C. A 0.10 μm layer consisting of a titanium flash and a gold capping layer was deposited on the path length to discriminate the two modes excited by the IDT. Fig. 4.5 shows the frequency spectrums of the device for an unmetallised propagation surface (solid line) and a metallised path (dotted line). When the path is metallised, the minimum loss was found at a frequency ~ 800 kHz higher than for the unmetallised path. This frequency shift demonstrates the conversion from SSBW to Leaky SH-SAW. By applying successive cross-linked S1813 photoresist polymer coatings on top of both a SSBW and leaky SH-SAW propagating on a 36YX.LT device, the minimum loss exhibited at the corresponding frequency of operation of each mode could be measured.

Fig. 4.6 a) and b) show the experimental results for the insertion loss change and frequency shift with increasing polymer layers on the LiTaO$_3$. The Love wave effect can be seen clearly for the SSBW mode (circles) with a reduction in frequency with increasing over-layer thickness. An initial reduction in the insertion loss is followed for thicker layers by a rapid increase in insertion loss with a sharp transition at z=0.08. By further increasing the guiding layer thickness a resonance pattern in frequency and insertion loss are also observed. The results for the resonant conditions of leaky SH-SAW mode are shown by the diamonds. The solid lines are included only as a guide to identify the data. The leaky SH-SAW mode does not exhibit the initial decrease in insertion loss observed with the SSBW mode. For this mode the insertion loss remains roughly constant before decreasing at approximately z=0.06 with a sharp transition at z=0.08. The phase velocities of the modes on the 36XY.LT are predicted to be similar on that crystalline direction [7]. Indeed, up to z=0.08 in fig. 4.6 b) there is little difference between the leaky SH-SAW mode and the SSBW mode. However, at the greater thickness the two modes can be distinguished by a small separation in operating frequency, showing that the leaky SH-SAW exhibits a slightly higher phase velocity than the SSBW when operating under thick guiding layers.

The initially constant insertion loss with increasing guiding layer thickness of the guided Leaky SH-SAW mode is consistent with Love wave theory although the initial decrease in insertion loss of the guided SSBW is not predicted. The leaky SH-SAW and SSBW mode are both considered as shear waves, the key difference between the two modes being in the propagation characteristics where the SSBW is launched at an angle of a few degrees to the surface [1,5-6], whereas the leaky SH-SAW propagates parallel to the surface. Thus, the deviation from expected Love wave behaviour for the insertion loss under thin wave-guiding layers on quartz, appears to be a consequence of the Love wave being generated from the SSBW mode.

For sensor applications this difference offers a possible new sensor parameter. The sensor parameters used in sensing experiments are the

change in resonant frequency (QCM) or the change in phase (SAW), resulting from mass deposition onto the device surface or a change in the liquid environment adjacent to the device surface. The observed changes in insertion loss with guiding layer thickness suggest that the insertion loss might itself be a useful sensor parameter to indicate changes in the surface state of a Love wave type device.

In section 4.1, higher order modes of Love wave were obtained by systematically increasing the wave-guide thickness. Those modes are characterized by a clear resonance in the frequency and insertion loss patterns. In section 2.4 theoretical results predict that the mass sensitivity is a function of the wave-guide layer thickness and of the mode order. Mass sensitivity of Love wave higher order modes to elastic, visco-elastic via insertion loss, and mass sensitivity of Love wave higher order modes to viscous loading via insertion loss and phase are presented in the next section.
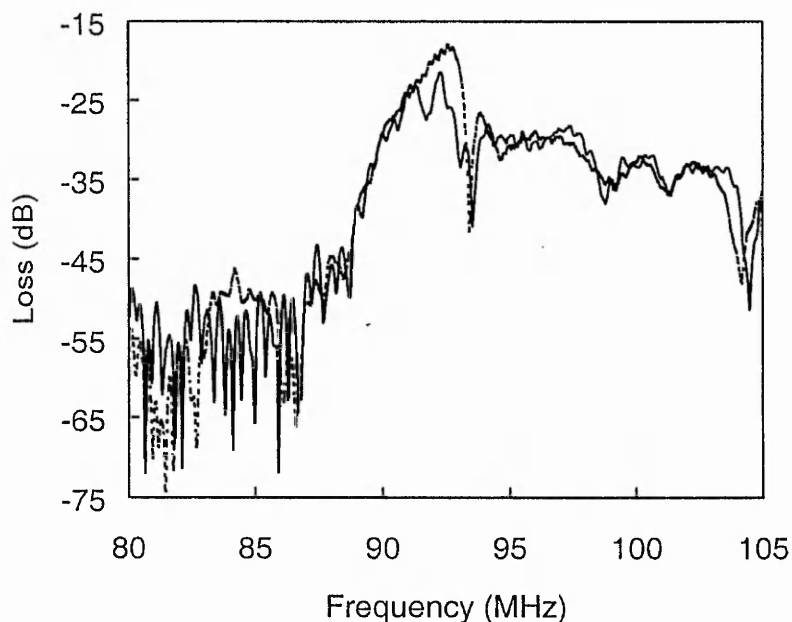

Fig. 4.5   a) Spectrums of device 2 on 36YX.LT, resonating at ~ 92 MHz when the propagation surface is left unmetallised (SSBW, solid line) and metallised with a thin layer of metal (Leaky SH-SAW, dotted line).
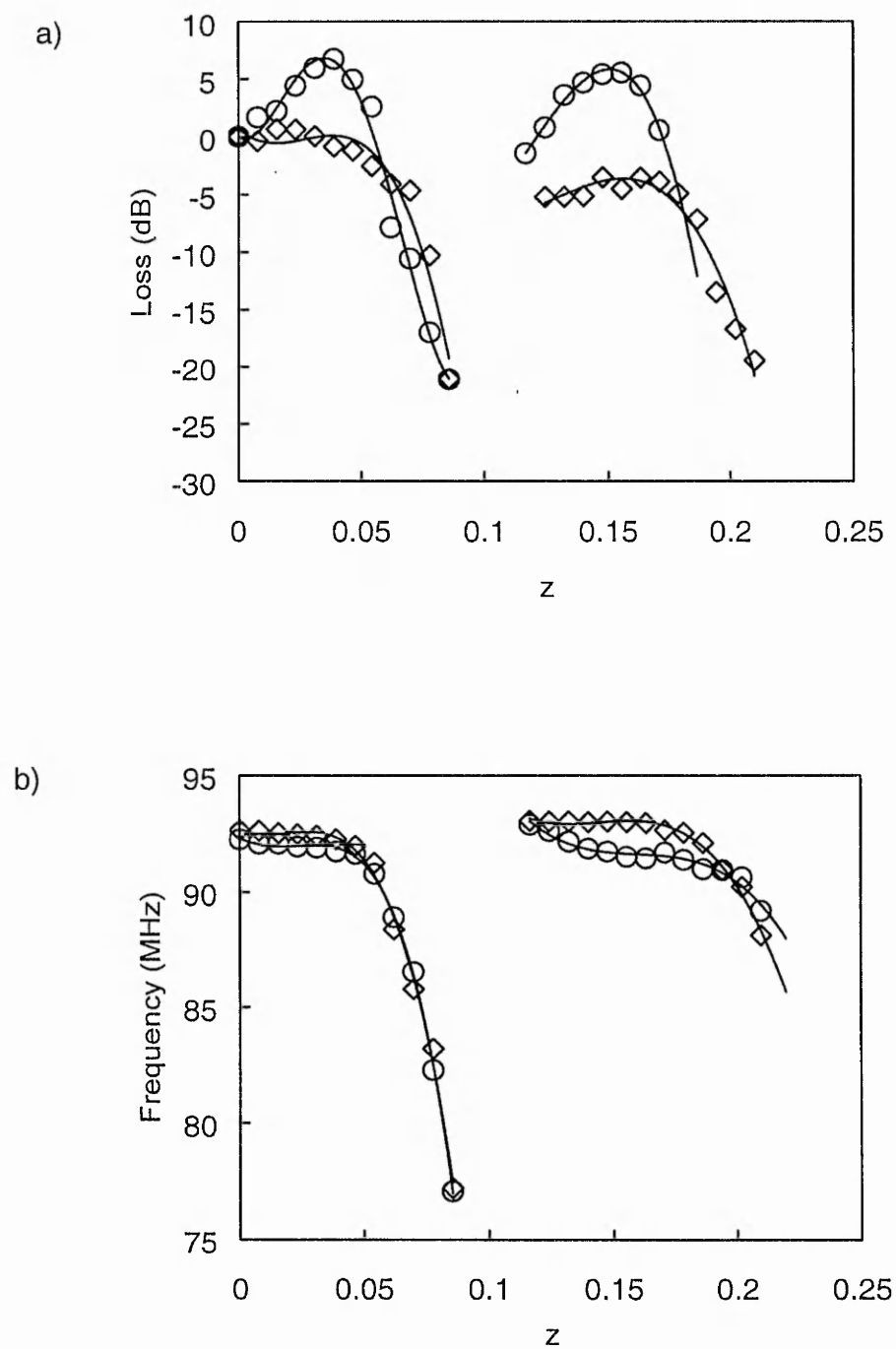
a)

b)

Fig. 4.6   Change in loss (a) and in frequency (b) as a function of z for leaky SH-SAW (diamonds) and SSBW (circles) on 36 YX.LT.

4.2 Experimental study of Love wave mass and liquid sensitivity

As in the previous section, devices 2 were employed and guiding layers consisting of S1813 photoresist (Shipley MicroElec.) diluted in 2-ethoxyehtyl acetate (2-EEA, Aldrich) were spun across the whole device at 4000 rot/min and cross-linked during 1 hour at 200 °C. A range of guiding layer thickness up to 12 microns was obtained.

The mass loading sensitivity in air was determined by evaporating thin gold and tin films on the propagation path and measuring the insertion loss exhibited by the signal at the corresponding fixed resonant frequency. Evaporated gold and tin film thicknesses up to 350 nm were obtained. The viscous loading sensitivity of the Love wave sensors was measured by the change in insertion loss from water at fixed frequency as liquid was passed over the device surface by using a flow cell system which isolates the SAW path from the IDTs. Liquid was passed through the flow cell at a rate of 5 ml/min. Poly (ethylene glycol) (PEG) solutions were prepared by dilution in deionised water. The 3350 and 10000 molecular weight PEG were obtained from Sigma and the 20000 molecular weight PEG was obtained from BDH. Solution viscosity was measured by using a Haake VT 181 viscometer system.

By applying successive cross-linked S1813 photoresist polymer coatings on top of a SSBW propagating ST-cut quartz device, the minimum loss exhibited at the corresponding frequency of operation of each mode was measured. Fig. 4.7 shows the experimental results of the frequency shift (triangles) and insertion loss change (circles) in air plotted versus the dimensionless parameter z defined as $z = d/\lambda_{IDT}$, where d is guiding layer thickness and λ_{IDT} is the transducer wavelength. The Love wave effect can be seen clearly for the SSBW mode with an initial reduction in the loss and a reducing frequency of operation with increasing over-layer thickness. For thicker layers, the loss increases rapidly and the frequency decreases with a sharp transition at $z \sim 0.04$. By further increasing the guiding layer thickness a

resonance pattern in frequency and insertion loss corresponding to the second Love wave mode is also observed. A minimum insertion loss is observed at z ~ 0.12 with a sharp transition at z ~ 0.13. A second resonance pattern corresponding to the third Love wave mode is observed with a minimum insertion loss at z ~ 0.22 and a sharp transition at z ~ 0.23.
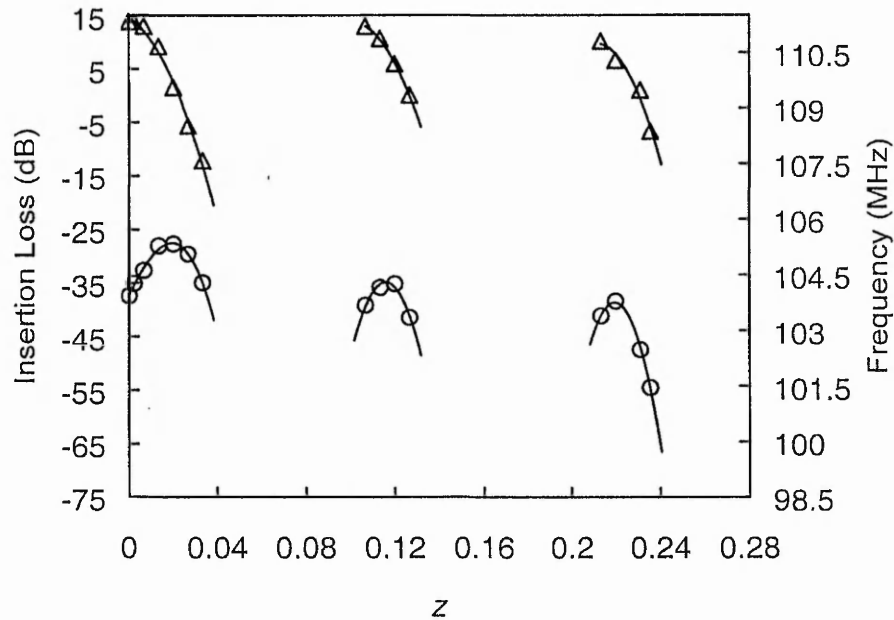
Fig. 4.7   Change in insertion loss (circles) and in operating frequency (triangles) for a 110 MHz device on ST-cut quartz as a function of z.

Polymer materials such as PMMA can have significant attenuation for shear wave propagation (section 1.2.7). It is then anticipated that for thick guiding layers, the insertion loss should significantly increase. This is preceded by an initial improvement in insertion loss because the substrate (ST-cut quartz) was chosen to use an SSBW mode. An optimised sensor involves choosing a wave-guide thickness as a compromise between sensitivity in phase velocity and an acceptable insertion loss. With a large insertion loss, the sensor cannot operate. Fig. 4.7 shows that a relatively

strong Love wave can re-occur as the guiding layer is further increased. These correspond to higher order Love wave modes [2]. The phase velocity mass sensitivity can be understood from the slope of the dispersion curves [17]. In a simple interpretation, any surface deposited mass can be viewed as increasing the guiding layer thickness and so moving the operating point of the Love wave further down the curve. For high mass sensitivity a large change in phase velocity is desired for a small surface deposited mass and this corresponds to a large slope in the relevant dispersion curve. In analogy to the phase velocity mass sensitivity, the sensitivity in insertion loss to mass deposition can also be viewed as related to the slope of the insertion loss curve with normalised guiding layer thickness. From fig. 4.7, the insertion loss slowly decreases until it peaks at $z \sim 0.02$ and, subsequently increases. Thus, good insertion loss mass sensitivity occurs with opposite signs either side of the peak at $z \sim 0.03$.

In the simple view of liquid sensitivity for the thickness shear mode quartz crystal microbalance, the motion of the crystal in a liquid entrains an interfacial mass layer (section 2.3.5). Thus, whilst the sensitivity of the Love wave devices has been discussed using a surface deposited mass analogy to the guiding layer mass, it is also possible that the sensitivity in insertion loss in liquid media will increase with larger thicknesses of the guiding layer. In both cases, sensitivity is expected to be larger if the operating thickness of the wave-guiding layer is chosen to correspond to a larger slope on the dispersion curve.

4.2.1 Elastic mass sensing

Love wave devices of design 2 were fabricated with wave-guiding layer thicknesses corresponding to the operating points z=0, 0.006, 0.013, 0.02, 0.027 (first Love mode), 0.106, 0.113, 0.12, 0.127 (second Love mode) and 0.21, 0.213 and 0.227 (third Love mode). These were tested for mass sensitivity in air by initially evaporating gold films on the propagation path. The area coated with gold was 28 mm^2 and the path length coated with gold was 4

mm. The insertion loss was measured at fixed frequency for film thicknesses up to 350 nm. The mass of gold films was calculated and the change in insertion loss was plotted against the mass of gold (in ng). Figures 4.8 a), b) and c) show the effect of gold mass loading for the first, second and third Love mode respectively. In fig. 4.8 a), at z=0, corresponding to a bare device, an initial improvement of the signal is observed with a maximum insertion loss change for a mass of gold of 600 ng. By further increasing the mass loading, the insertion loss decreases with a smooth slope. Signal improvement with the deposition of gold is observed for operating points up to 0.13. For z > 0.13, the insertion loss systematically decreases (signal damping) with gold mass loading and the slope of the curves becomes steeper, showing an increasing sensitivity to the gold mass loading. The metal coating process was repeated for the second and third Love mode (fig. 4.8 b) and fig. 4.8 c), respectively). In fig. 4.8 b), the second Love mode shows some initial signal improvement at z=0.106, 0.113 and 0.12 with a minimum insertion loss (signal improvement) at 580 ng, 375 ng and 160 ng of evaporated gold respectively. At z=0.127, a systematic decrease of the insertion loss was found. In fig. 4.8 c), the third Love mode shows some guiding effect for z=0.22 and 0.213 and a systematic decrease of the insertion loss for z=0.227.

Thus, initial signal improvement preceding the attenuation of the signal in air was found as the Love wave device was loaded with gold films corresponding to a guiding effect comparable to the polymer wave-guide coating. In this experiment, the gold layers are thick enough to act as guiding layers and, as predicted, the sensitivity of the devices to gold coating increases with the wave-guide thickness. Furthermore, figs 4.8 b) and 4.8 c) show that the second and third Love modes have substantial sensitivity to gold coating and are comparable to the first Love mode mass sensitivity.

Fig. 4.8   Change in insertion loss at the a) first, b) second and c) third Love mode versus mass of evaporated gold for increasing z. a) circles:0, diamonds: 0.006, triangles: 0.013, squares: 0.02, stars: 0.027; b) circles: 0.106, diamonds: 0.113, triangles: 0.12, squares: 0.127; c) circles: 0.213, diamonds: 0.22, triangles: 0.227.

As a comparison, an identical series of experiments was conducted to test the mass loading sensitivity of the Love modes to the deposition of tin. Fig. 4.9 a), b) and c) show the effect of tin deposition (in ng) on the propagation path of the Love wave devices to the insertion loss for the first, second and third Love modes respectively. The observed behaviour is very similar to that with gold coating. An identical guiding effect was observed for the first, second and third Love modes and sharp transitions corresponding to maximum sensitivity were found for devices operating at $z=0.027$ for the first Love mode, $z=0.127$ for the second Love mode and $z=0.227$ for the third Love mode.

In this section, it has been shown that in analogy to the phase velocity mass sensitivity, the sensitivity in insertion loss to mass deposition is related to the slope of the insertion loss curve with normalised guiding layer thickness (fig. 4.7). In addition, it has been shown that metal deposition sensing with Love wave devices can also be achieved with higher order modes by extending the wave-guide thickness and that higher order Love wave modes exhibit substantial sensitivity to mass loading. Love wave sensor sensitivity has already been quoted elsewhere for the first Love mode by a number of authors [18-25]. In this work, a guiding effect has been demonstrated for the first three Love modes by using thin layers of gold and tin coatings and this could be extended to a large range of metals. Furthermore, the interpretation of the dispersion curve suggests the metal layer on top of the two layers system (substrate plus wave-guide) can be viewed as the extension of the second wave-guide layer as well as the perturbation layer for thin and moderate thicknesses.
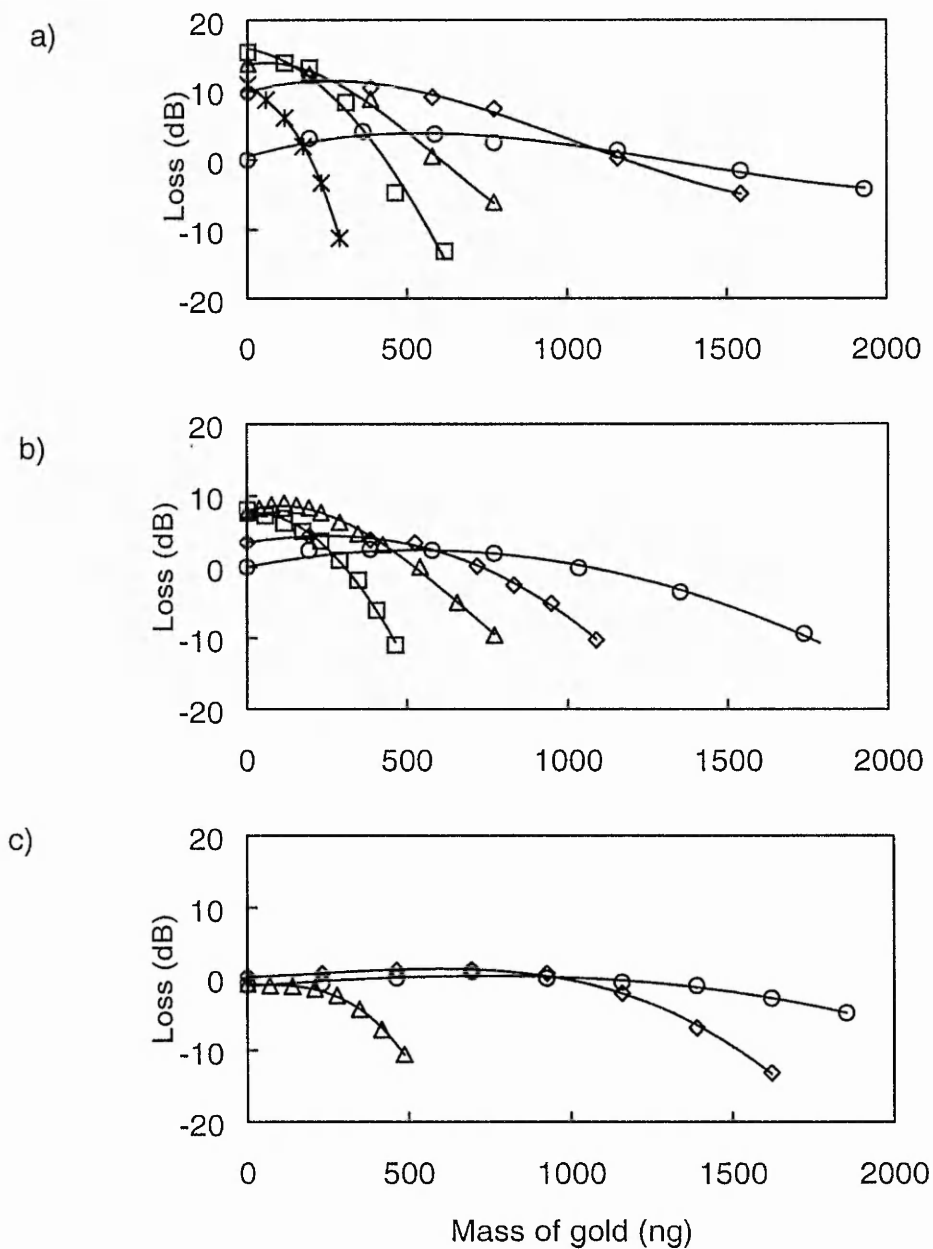
a)
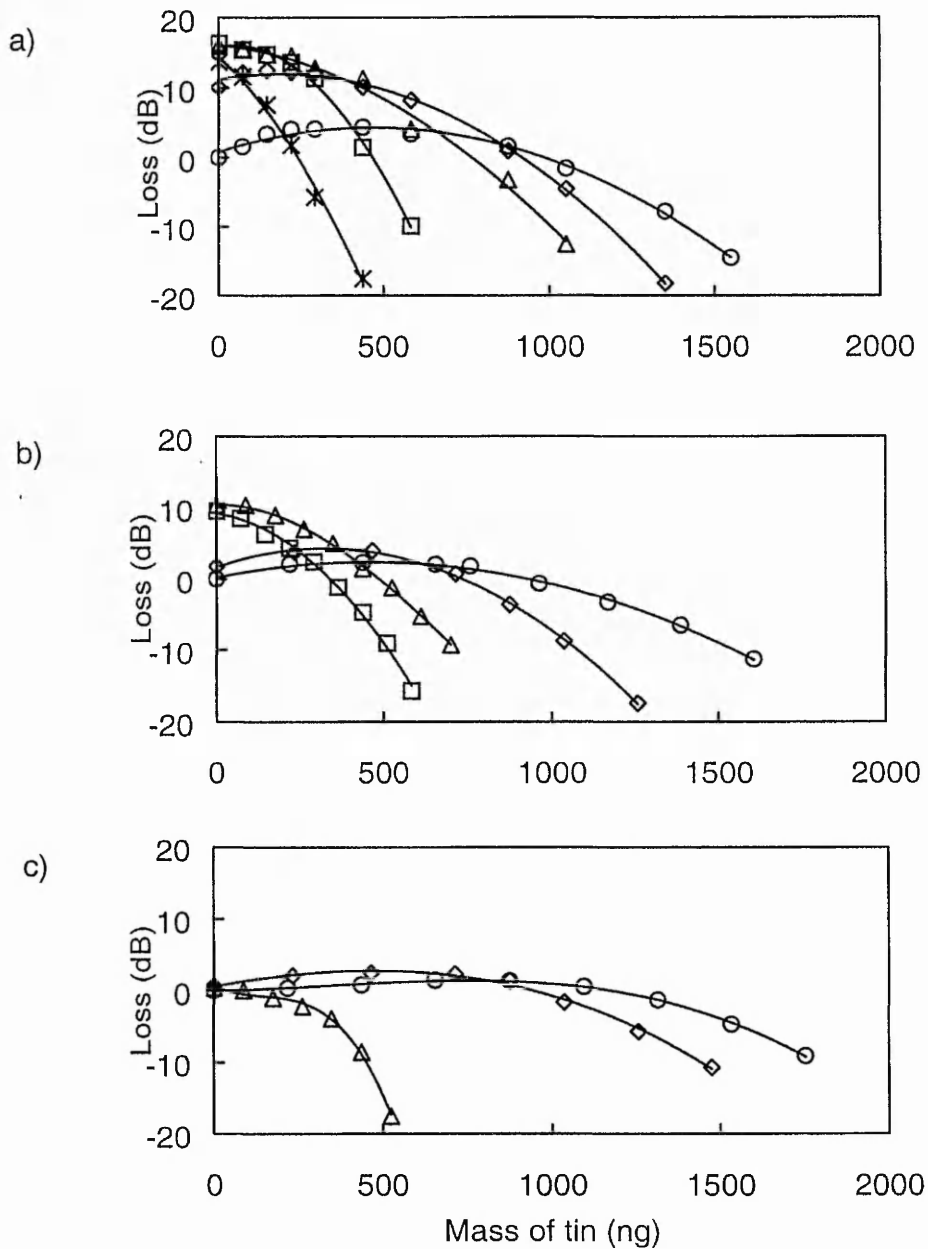
b)

c)

Mass of tin (ng)

Fig. 4.9   Change in insertion loss at the a) first, b) second and c) third Love mode versus mass of evaporated tin for increasing z. a) circles:0, diamonds: 0.006, triangles: 0.013, squares: 0.02, starts: 0.027; b) circles: 0.106, diamonds: 0.113, triangles: 0.12, squares: 0.127; c) circles: 0.213, diamonds: 0.22, triangles: 0.227.

4.2.2 Visco-elastic mass sensing

A simple extension of the results in section 4.2.1 is to test for mass sensitivity in air to polymer layers by spin-coating S1813 photo-resist on the propagation path, but then only softbaking the layer. The Love wave devices in section 4.2.1 fabricated from design 2, fabricated with hard-baked photoresist layers corresponding to the operating points z=0, 0.006, 0.013, 0.02, 0.027 (first Love mode), 0.106, 0.113, 0.12, 0.127 (second Love mode), 0.22, 0.213 and 0.227 (third Love mode) were used in these experiments. The mass loading photoresist layers were softbaked at 100º C during 15 min and the area coated with photoresist was 28 mm^2. Softbaking leaves the polymer with some viscoelasticity.

The mass of the resist films was calculated and the change in insertion loss was plotted against the mass of resist (in ng). Fig. 4.10 a), b) and c), show the effect of resist mass loading for the first, second and third Love modes, respectively. As for gold and tin deposition, the resist coating on the path length produces a substantial guiding effect. Maximum change in insertion loss for a given deposited resist mass is high when the operating point z is chosen to be at the point of steepest slope of the insertion loss dispersion curve where the guiding layer losses start to dominate the Love wave. The second and third Love modes also exhibit similar guiding effects with the deposition of resist although the initial signal improvement preceding the attenuation of the signal is less for higher order modes. Nonetheless, the second and third Love modes show substantial sensitivity to resist coating and are comparable to the first Love mode mass sensitivity.

In the approximation that the material being sensed is elastic mass with shear acoustic velocity similar to that of the guiding layer, then it has been predicted in chapter 2 that the maximum change in insertion loss for a given deposited mass will be high when the operating point is chosen to be at the point of steepest slope of the insertion loss dispersion curve.

a)

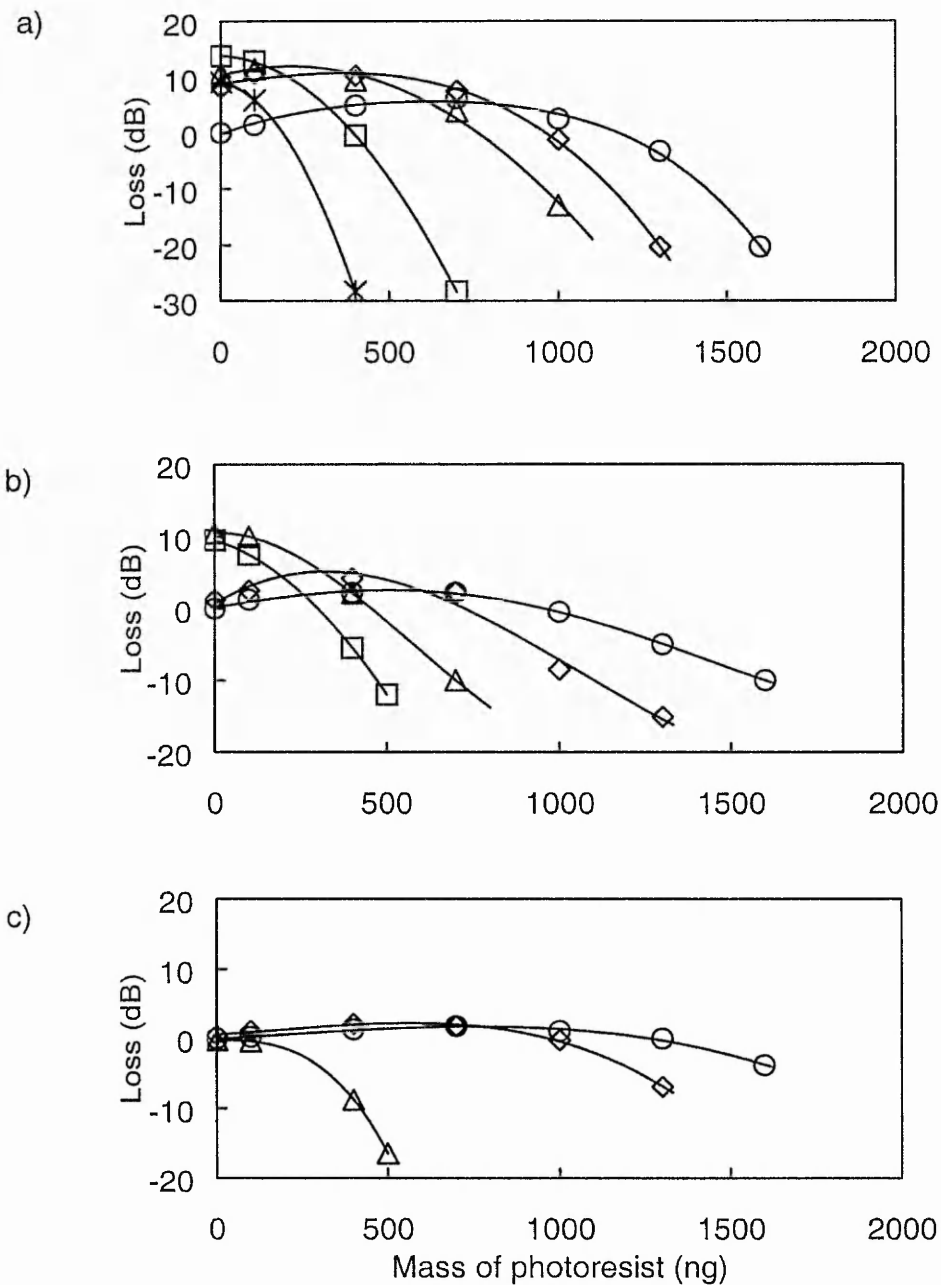
b)

c)

Mass of photoresist (ng)

Fig. 4.10   Change in insertion loss at the a) first, b) second and c) third
Love mode versus mass of spin-coated soft-baked resist for
increasing z. a) circles:0, diamonds: 0.006, triangles: 0.013,
squares: 0.02, starts: 0.027; b) circles: 0.106, diamonds:
0.113, triangles: 0.12, squares: 0.127; c) circles: 0.213,
diamonds: 0.22, triangles: 0.227.

Theoretically, for an elastic mass layer, insertion loss can be a highly sensitive parameter because the elastic mass can convert the wave from having a low loss to a high loss via the transfer of the wave displacement from the substrate (low loss material) to the guiding layer (high loss material) [2,4,17]. In section 4.2.1 and 4.2.2, it has been shown that insertion loss is sensitive to deposited solid layers whether they are elastic or viscoelastic and that there is no absolute requirement for the deposited mass itself to be viscoelastic. The logical extension of these ideas is to the effect of the wave-guide operating point on the dispersion curve to the sensitivity of Love devices towards liquid loading and this is considered in the next section.

4.2.3 Liquid sensing

4.2.3.1 Insertion loss

A series of liquid sensing experiments was applied to the Love wave device for several values of the guiding layer thickness d, thus setting the operating point z on the dispersion curves in fig. 4.1 b). At each guiding layer thickness, the device was exposed to deionised water through a flow cell with a continuous flow system. The effect of the flow cell and of the water loading on insertion loss are indicated by the solid line with squares and solid lines with diamonds respectively in fig. 4.11, solid lines with circles represent the effect of polymer coating in air. From fig. 4.11, it is apparent that the flow cell produces increasing damping of the wave with increasing wave-guide thickness for each mode. However, reasonable insertion loss is maintained up to $z=0.027$. Liquid loading also produces damping of the wave, as an increasing fraction of the signal is lost with increasing guiding layer thickness. For thin layers of wave-guide ($z < 0.02$), water loading has little effect on insertion loss. However, for $z > 0.02$, a rapid decrease in insertion loss is observed and a sharp transition is reached at $z=0.027$ indicating an increase in insertion loss sensitivity in water compared to air. From fig. 4.11, the effect of the flow cell and the water is observed to decrease with higher order Love

wave modes confirming that mass sensitivity is a function of mode order. The first Love mode to have significant damping at, for example $z \sim 0.02$, whilst the second and third Love mode are localized into the guiding layer, the insertion loss would be expected to saturate [4].
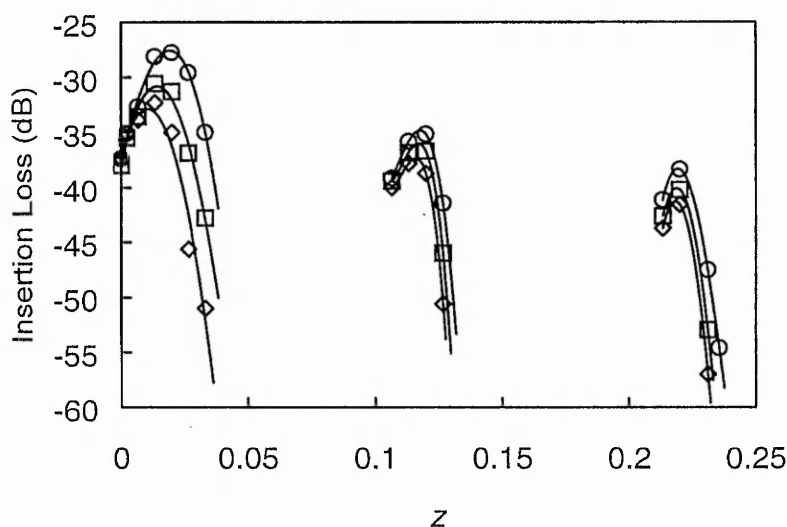
Fig. 4.11   Effect of flow cell (squares) and water (diamonds) on the insertion loss of Love wave modes from air (circles).

To further investigate the sensitivity of the Love wave device with different guiding layer thickness, fourteen solutions of 3350 molecular weight PEG with increasing densities (34.4, 68.8, 103.2, 137.6, 172.0, 206.4, 240.8, 275.2, 309.6, 344, 378.4, 412.2, 447.4 and 481.6 g l^{-1}) in a successive order of viscosity were prepared. The viscosity range of the solutions was 0.02–0.22 Poise for the PEG 3350 solutions. Solutions were then passed over the surface of the device. The Love wave devices tested for viscous loading are identical to those used for mass loading effect (fig. 4.7). The signal loss as a function of weight of solute was first investigated by using solutions loaded with PEG 3350. In fig. 4.12 a) the sensitivity in insertion loss of the Love wave devices for the first Love mode to PEG 3350 solutions from water is shown. A general way to illustrate the amplitude/viscosity relationship is by plotting the

square root density-normalized amplitude change of the wave ($IL/\sqrt{\rho}$) versus the square root of the viscosity of the liquid ($\sqrt{\eta}$) [26]. In fig. 4.12 a), the change in insertion loss is systematically increasing (damping of the wave) with the density of the solutions. When solutions of low viscosity are applied ($\eta<0.08$ Poise), $IL/\sqrt{\rho}$ shows a linear relationship with $\sqrt{\eta}$. The effect of the above viscous-liquid interactions results in acoustic energy being dissipated in the fluid and is measured as an increase in acoustic losses (Newtonian fluid). However, beyond this value, the graph indicates that $IL/\sqrt{\rho}$ tends to reach an asymptotic value. At these high viscosities, the fluid exhibits a frequency-dependent mechanical behaviour, is varying from viscous liquid state to an elastic solid and is known as Maxwellian fluid. In this case the oscillation period of the wave in the fluid becomes smaller that the liquid relaxation time, the liquid molecules cannot follow the induced oscillation and the losses saturate. Fig. 4.12 a) also shows that the change in insertion loss increases with the wave-guide thickness as previously predicted; maximum sensitivity was found at the operating point z=0.027. Fig. 4.12 b) and 4.12 c) show the effect of PEG 3350 viscous loading on the insertion loss for the second and third Love modes. At the second and third Love modes, the device exhibits saturation values in $IL/\sqrt{\rho}$ which are about half and third respectively (at z=0.127 and z=0.227) those observed at the first Love mode (at z=0.027). Liquid sensing at the second and third Love mode is then possible and sensitivity in viscous loading is comparable within a factor of 2 and 3 with the first Love mode. Saturation in acoustic losses was also found at higher order modes at each operating point.

4.2.3.2 Phase

Simultaneously with the insertion loss data, phase changes were measured under the same experimental conditions as previous section. Fractional change in phase velocity can be calculated from changes in phase [26,27].
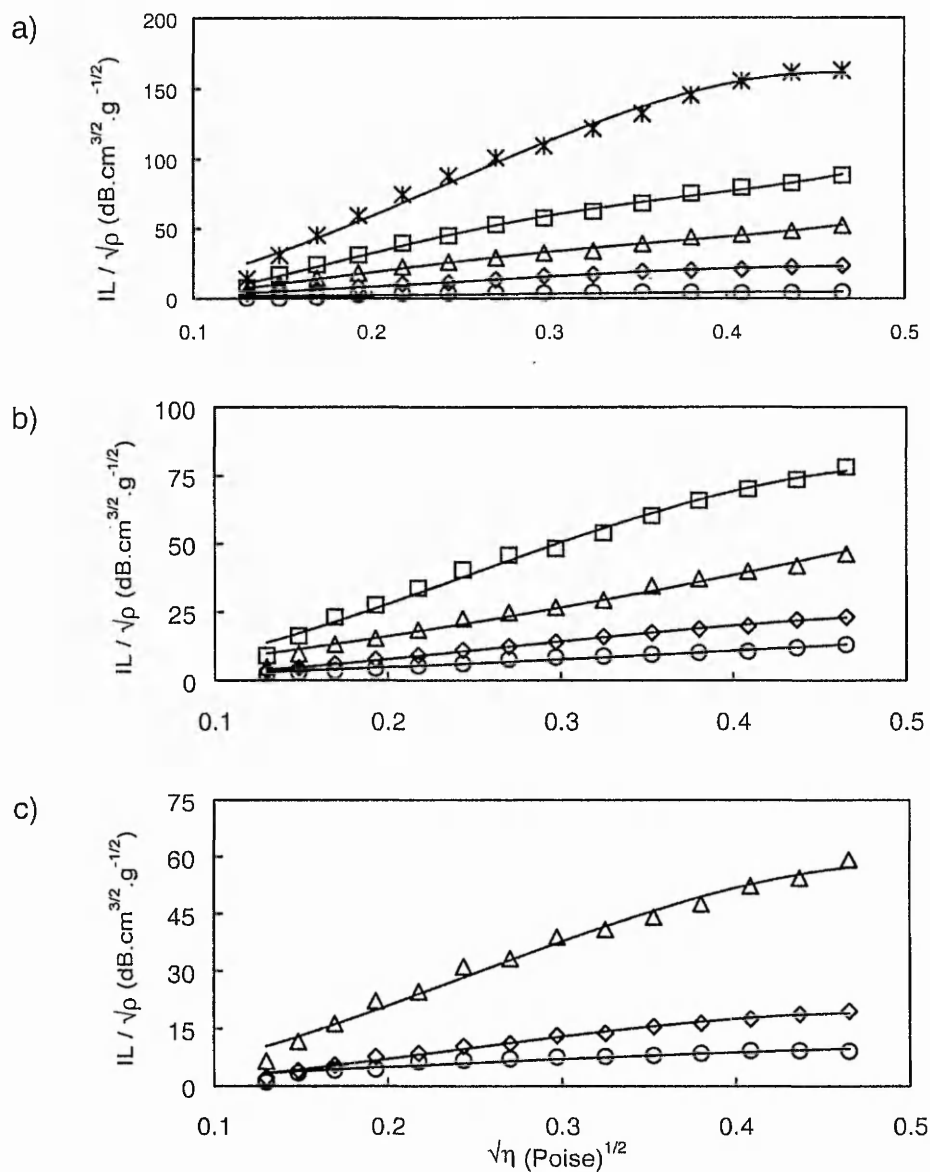
Fig. 4.12   Change in insertion loss from water normalized to the square root of the solutions density versus the square root of the solutions viscosity at the a) first, b) second and c) third Love mode with increasing z. a) circles:0, diamonds: 0.006, triangles: 0.013, squares: 0.02, stars: 0.027; b) circles: 0.106, diamonds: 0.113, triangles: 0.12, squares: 0.127; c) circles: 0.213, diamonds: 0.22, triangles: 0.227- by using PEG 3350.

These changes can then be plotted as a function of the relative density-viscosity product of the solutions [26], $\sqrt{(\rho_{PEG}\eta_{PEG})}-\sqrt{(\rho_w\eta_w)}$, which extracts the contribution of the polymer (subscript PEG) from the contribution of the water (subscript w). Fig. 4.13 a), b) and c) show the fractional change in phase velocity ($\Delta V_p/V_p$), where ΔV_p is calculated using the phase change at resonant frequency and V_p is the unloaded phase velocity for the guiding layer thickness used, versus $\sqrt{(\rho_{PEG}\eta_{PEG})}-\sqrt{(\rho_w\eta_w)}$ for the first, second and third Love mode respectively, for various normalized guiding layer thickness, noted z. As for the insertion loss, the linear initial increase in $\Delta V_p/V_p$ characterizes the Newtonian region and the saturation region characterizes the Maxwellian region. In fig. 4.13 a), fractional changes in phase velocity increase with increasing $\sqrt{(\rho_{PEG}\eta_{PEG})}-\sqrt{(\rho_w\eta_w)}$ as the mass loading becomes more important. Furthermore, by working on a single mode, thicker waveguide layers induce larger deviations and, thus higher mass sensitivity. However, as expected, fractional changes in phase velocity become less important when working with higher order modes. In fig. 4.13 a), b) and c), a saturation region appears when $\sqrt{(\rho_{PEG}\eta_{PEG})}-\sqrt{(\rho_w\eta_w)} \sim 4$ kg.s^{-1}.m^{-2}, when the fluid is regarded more as a solid by the Love wave sensor (Maxwellian fluid). This value also represents the limit of the Newtonian regime region. At the second and third Love modes, the device exhibits saturation values in $\Delta V_p/V_p$ which are about half and third respectively those observed at the first Love mode. Similarly to the insertion loss, liquid sensing at the second and third Love mode by using phase measurements is possible and sensitivity in viscous loading is comparable within a factor of 2 and 3 with the first Love mode.
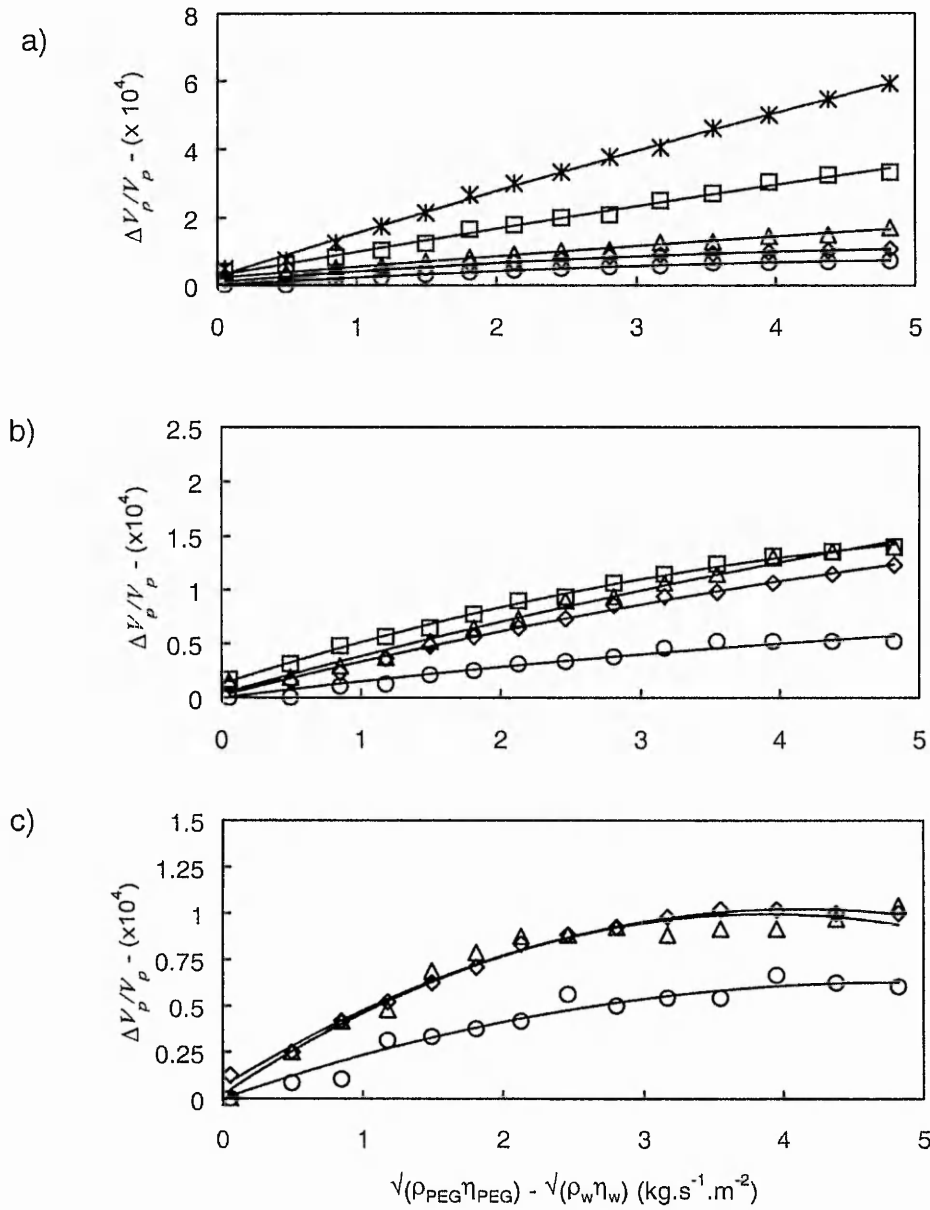
Fig. 4.13   Fractional change in phase velocity from water versus the difference between the square root of the density-viscosity product of the PEG solutions and the water at the a) first, b) second and c) third Love mode with increasing z. a) circles:0, diamonds: 0.006, triangles: 0.013, squares: 0.02, stars: 0.027; b) circles: 0.106, diamonds: 0.113, triangles: 0.12, squares: 0.127; c) circles: 0.213, diamonds: 0.22, triangles: 0.227- by using PEG 3350.

Higher molecular weight of PEG was also investigated by using PEG 10000 and 20000. Fourteen solutions were prepared for each molecular weight at the same concentrations as with PEG 3350. Results for insertion loss and phase are showed in Appendix C. The viscosity range was 0.02 - 0.92 Poise for the PEG 10000 and 0.025 - 3.15 Poise for the PEG 20000. Higher molecular weight PEG allowed the Maxwellian regime to be more pronounced as the viscosity range was increased. However, changes in the acoustic signal response were found similar to those reported in this section.

It has been shown that sensitivity to viscous loading of higher order modes via insertion loss are comparable to the first Love wave mode without completely sacrificing signal strength. Sensing operations at the second and third Love modes have been achieved and higher order modes could be used. By extending the wave-guide thickness, the capabilities of the Love wave sensors can be extended to a larger range of (bio) chemical applications [28-32] whilst still retaining relatively high sensitivity compared to acoustic plate mode or quartz crystal microbalance sensors. The results also show sensitivity in insertion loss can be expected and that high sensitivity in both phase and insertion loss can be obtained with reasonable signal amplitude.

110 MHz Love wave acoustic sensors based on a polymer/ST-cut quartz structure and 92 MHz Love wave acoustic wave sensors on a polymer coated 36 YX.LT have been fabricated, which allowed clearly to distinguish between a SSBW and a leaky SH-SAW derived Love wave sensor. The 110 MHz Love wave sensors on ST-cut quartz were operated as mass, visco-elastic and viscous loading sensors. The polymer wave-guide was extended to allow sensing operations at the second and third Love modes to be achieved. Mass sensitivity to the deposition of evaporated metals, of sensing material of the same type as the guiding layer and to applications of viscous liquids was investigated as a function of the acoustic losses for the first, second and third Love modes. Thin metal and viscoelastic coatings were found to act as small perturbations whereas thick depositions behave as the

extension of the wave-guide layer. The viscous loading of liquids causes systematic damping of the wave. Changes in insertion loss normalized to the square root of the solution density and fractional change in phase velocity were found to be proportional to the square root of the solution viscosity for a small range of viscosities, $\eta < 0.08$ Poise, and tends to saturate at higher viscosities for such devices. Viscous loading mass sensitivity in insertion loss and phase velocity for higher order Love modes were found to be within a factor of 2 or 3 comparable to the first Love mode. It is concluded that sensing operations at higher order Love modes is possible and could be used for liquid phase applications such as (bio) chemical sensors.

References

[1] F. Martin, Electr. Lett., **38** (16) (2002), 941.

[2] G. McHale, M. I. Newton, F. Martin, J. Appl. Phys., **91** (2002), 5735.

[3] G. W. C. Kaye. T. H. Laby, Tables of Physical and chemical constants, Longman Ed., (1973), ISBN 0582463262.

[4] G. McHale, M. I. Newton, F. Martin, J. Appl. Phys, Accepted (Oct 2002).

[5] T. I. Browning, D. J. Gunton, M. F. Lewis, C. O. Newton, Ultrasonics, 12 (1974), 115.

[6] M. F. Lewis, Electr. Lett., **17** (1981), 819.

[7] K. Y. Hashimoto, Springer-Verlag 2000, ISBN 3-540-67232-X.

[8] J. Kondoh, Y. Matsui, S. Shiokawa, The 7th Int. Conf. Sensors and Actuators (1997), 534.

[9] J. Kondoh, S. Hayashi, S. Shiokawa, Jpn. J. Appl. Phys., **40** (2001), 3713.

[10] J. Kondoh, S. Shiokawa, Jpn. J. Appl. Phys, **33** (1994), 3095.

[11] J. Kondoh, S. Shiokawa, Sensors and Actuators B, **13-14** (1993), 429.

[12] J. Freudenberg, M. Von Schickfus, S. Hunklinger, Sensors and Actuators B, **76** (2001), 147.

[13] N. Barie, M. Rapp, H. J. Ache, Sensors and Actuators B, **46** (1998), 97.

[14] W. Welsh, C. Klein, R. M. Oksuzoglu, M. Von Schickfus, S. Hunklinger, Sensors and Actuators A, **62** (1997), 562.

[15] F. Josse, F. Bender, R. W. Cernosek, Anal. Chem, **73** (2001), 5937.

[16] F. Bender, R. W. Cernosek, F. Josse, Electr. Lett., **36** (2000), 1672.

[17] G. McHale, M. I. Newton, F. Martin, J. Appl. Phys., **91** (2002), 9701.

[18] G. L Harding, Smart. Mater. Struct., **6** (1997).

[19] B. Jakoby, M J Vellekoop, Sensors and Actuators A, **678** (1998).

[20] G. L Harding, Sensors and Actuators A, **88** (2001).

[21] G. L. Harding, Sensors and Actuators A, **65** (2000).

[22] G. L. Harding, J. Du, P. R. Dencher, D. Barnett, E. Howe, Sensors and Actuators A, **61** (1997), 279.

[23] J. Du, G L Harding, Sensors and Actuators A, **56** (1996), 211.

[24] F. Herrmann, S. Buttenbach, Physica status solidi, pss/RRN-98-045, (2000).

[25] G. Kovacs, Proc. IEEE Ultrasonics Symp. Tucson, AZ, USA (1992).

[26] A. J. Ricco, S. J. Martin, Appl. Phys. Lett., **50** (1987), 1474.

[27] R. W. White, P. J. Wicher, S. W. Wenzel, E. T. Zellers, IEEE Trans. Ultrason. Ferro. Freq. Contr , **34** (1987), 162.

[28] E. Gizeli, N. Goddard, C. Lowe, Sensors and Actuators B, **6** (1992) 131.

[29] E. Gizeli, M Liley, C. R. Lowe, H Vogel, Anal. Chem, **69** (1997), 4808.

[30] M. Weiss, Anal.Chem, **70** (1998), 2881.

[31] C. Zimmermann, D. Rebiere, C. Dejous, J. Pistre, E. Chastaing, R. Planade, Sensors and Actuators B, **3735** (2001), 1-9.

[32] F. Josse, F. Bender, R. Cernosek, Anal. Chem., **73** (2001), 5937.

CHAPTER 5

PULSE MODE

OPERATION

CHAPTER 5
PULSE MODE OPERATION

In Chapter 3, a pulse mode system was developed for the measurement of phase and amplitude of Love wave signals as an alternative to using a network analyzer. The first half of this chapter reports the detection capabilities of this pulse mode system in a model biosensing experiment consisting of the deposition and removal of vesicles from the device surface. The second half of the chapter focuses on the issue of inherent dispersion of Love wave sensors and the relationship between group and phase velocity applied to Love wave sensors.

5.1 Pulse mode measurements of vesicle deposition and removal

The pulse mode system is an alternative method to the relatively slow network analyser, which uses a continuous wave method of measurements. The pulsed technique has been previously utilised by number of authors. Pulsed techniques providing short-lived continuous waves were first investigated by Mason [1] in the 1950's, followed by Maxwell [2] in the 1980's, and more recently by Rodahl *et al* [3]. Shear SAW pulsed analysis for determining SAW interactions with liquids were first reported by McHale *et al* [4], a shear horizontal SAW pulsed method was reported by Chung *et al* [5] and, for sensing applications, simultaneously developed and reported by Newton *et al* [6] and Stevenson *et al* [7]. The Love wave devices used in model biosensing experiment of this chapter were a 110 MHz split-finger IDT design patterned on a ST-cut quartz crystal, with propagation orthogonal to the crystalline x-axis (design 2). The guiding layer consisted of spun S1813 resist, cross-linked at 200 °C for 1 hour. Prior to the sensing, the surface was made hydrophilic by treatment with a sol-gel derived silica coating. The hydrophilic surface preparation presents a rough surface, which induces

absorption of a vesicle layer. A solution consisting of 1 ml of 5.8 M HCl mixed with 5 drops of ortho-silicate (Aldrich) was prepared. The device was spin-coated, for each layer at 4000 rpm during 35 s, with 5 drops of pure ortho-silicate and then 5 drops of the HCl-ortho-silicate mixture. The surface was finally washed with deionised water. A silicone gasket was used to isolate the propagation path from the IDTs and liquid was passed through the flow cell at a rate of 5 ml min^{-1} for the calibration experiment and 0.5 ml min^{-1} for the biosensing.

A model biosensing experiment was devised to test out the detection capabilities of the pulse mode system. The model is sketched in fig. 5.1. In fig. 5.2 a), the changes in insertion loss and phase as a function of time for a model biosensing experiment with the CW system are presented. The device was initially immersed into a buffer solution, phosphate buffered saline (PBS), which was then followed, at t=150 s, by the deposition of 0.2 mg ml^{-1} of vesicles of palmitoyl-oleoyl-sn-glycerophosphocholine (POPC) in PBS. The vesicle layer was then removed at t=500 s, by a detergent, t-octyl-phenoxypolyethoxyethanol (Triton) at 0.1(v/v) % in PBS. The signal is observed to return to its original value, indicating that the POPC was readily rinsed off. It was followed by a second sequence of POPC deposition at t=1150 s and removal at t=1550 s. The rapid transition in insertion loss and phase is typical of the POPC removal process as the addition of detergent disrupts the adsorbed vesicles and has been already reported [8]. The hydrophilic surface preparation presents a rough surface, which induces absorption of vesicle layer resulting in a large signal change, which is expected for the formation of a visco-elastic layer. Fig. 5.2 b) shows the equivalent experiment using the pulse mode system. In this case, the first deposition of POPC in PBS was at t=0 s, the removal was at t=350 s and this was followed by a second sequence of POPC deposition at t=850 s and removal at t=1250 s. The sampling rate of the pulse mode system was chosen to be 86 measurements per minute in common with the CW system. However, the maximum sampling rate of the pulse mode system is much faster and only

limited by the GPIB transfer rate; the use of a fast A/D converter would allow several hundreds measurements to be made each minute.

SH-SAW device

SH-SAW with waveguide

Surface preparation with Silicate

sol-gel

Deposition of a lipid monolayer in PBS

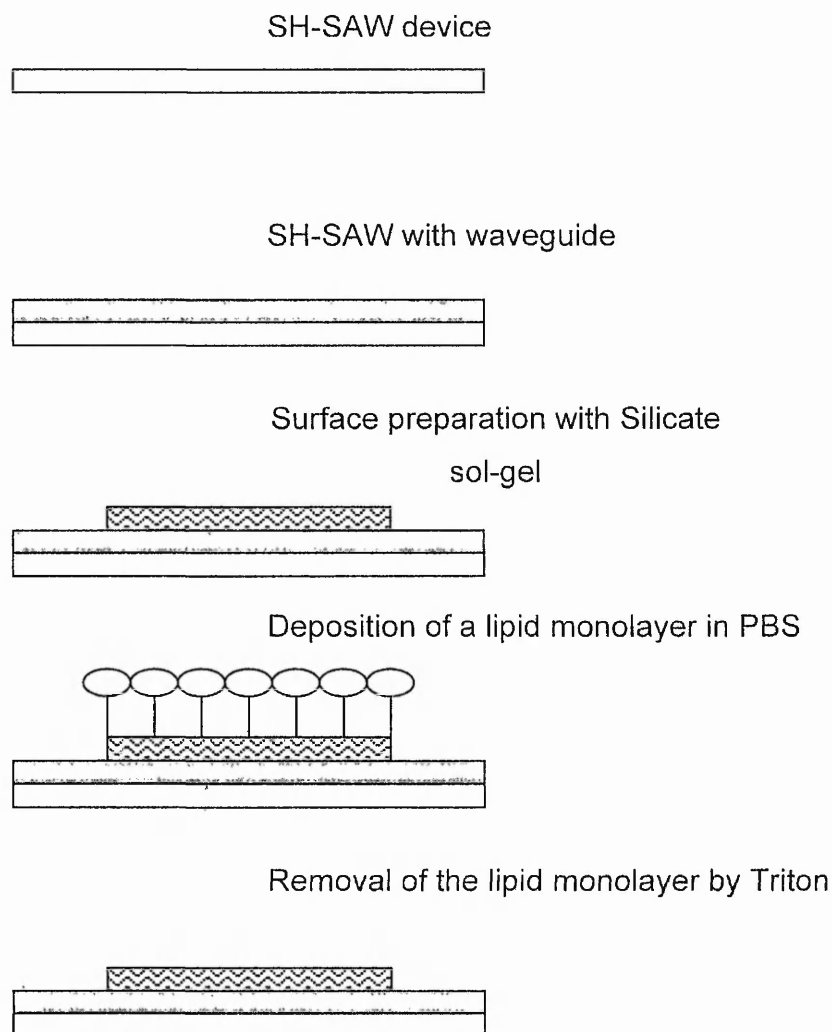Removal of the lipid monolayer by Triton

Fig. 5.1   Schematic representation of the deposition and removal of lipids on a Love wave sensor.
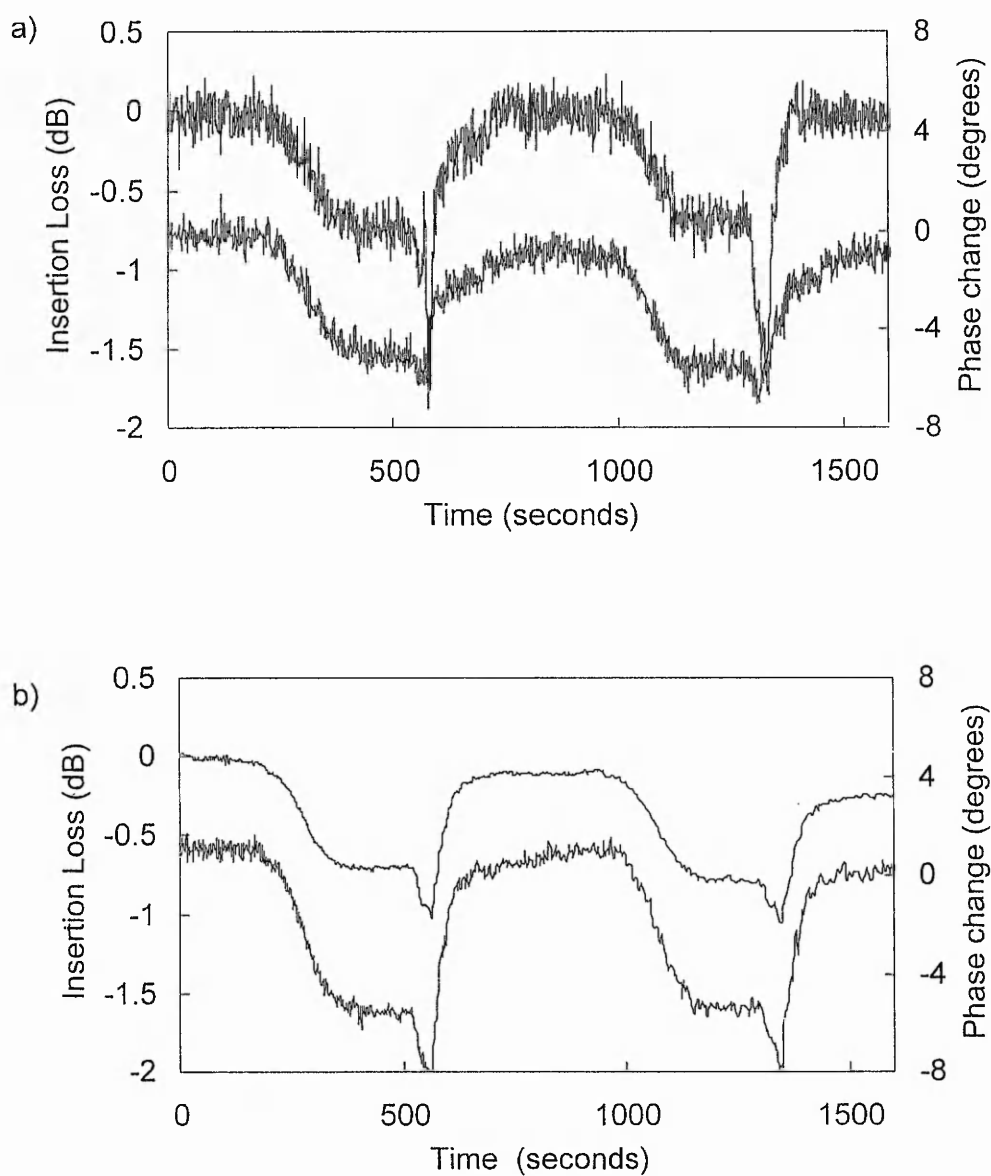
Fig. 5.2   Change in insertion loss (upper line) and in phase (lower line) for two cycles of deposition and removal of POPC by using a) the 8712 ET network analyzer and b) the pulse mode system.

The results in fig. 5.2 would tend to contradict those obtained by Stevenson *et al* [7]. Stevenson showed there is a significant difference in the magnitude of the response given by network analyser and by their pulse mode system. However, in the system in fig. 5.2, the measurement of amplitude results from sitting the boxcar gate on the peak signal rather than making a power measurement of the entire pulse. Stevenson also used a higher frequency range possibly giving a larger difference between phase and group velocities, the substrate also possibly giving highly non-linear modes.

5.2 Experimental study of Love wave sensor response by phase and group velocity measurements

Both experimental and modelling results (sections 2.4 and 2.5) [9-18] show that, for a particular polymer, the sensitivity to mass loading initially increases with the over-layer thickness and then exhibits an optimum sensitivity at the maximum slope of the dispersion curve. This change in sensitivity mirrors the dependence of the phase velocity on the normalized guiding layer thickness evident in the dispersion curve (see fig. 2.14).

The optimum mass sensitivity can be evaluated by experimentally determining the dispersion curve, but this method requires the device to undergo a coating calibration process over a large range of thickness. However, in a pulse mode experiment, the pulse contains a range of frequencies, or equivalently normalized guiding layer thicknesses, and therefore effectively samples a small region of the dispersion curve. Thus, a pulse mode experiment offers a possible method of determining the sensitivity of a given Love wave device without requiring a coating procedure. In addition, the group velocity itself may provide an alternative sensor parameter.

5.2.1 Theoretical relationship between mass sensitivity and group and phase velocity

In section 2.5, a new method of evaluating the mass sensitivity for guided SH-SAW devices based upon measurement of the phase and group velocity was predicted. The sensitivity to mass deposition, S_m defined as the fractional change in phase velocity divided by the mass per unit area, for guided SH-SAW devices was shown to be a function of the phase and group velocities, V and V_g, and the guiding layer thickness, d, and density, ρ_l (Eq. 56 in section 2.5),

$$S_m = \frac{1}{\rho_l d}\left(1 - \frac{V}{V_g}\right) = \frac{1}{\rho_l d}\left(\frac{V_g - V}{V_g}\right)$$

The mass sensitivity is therefore the fractional deviation of the phase velocity from the group velocity divided by the mass per unit area due to the guiding layer. Fig. 5.3 shows the calculated Love wave (first, second and third modes) phase speed curves (solid line) for an infinitely thick substrate with shear speed and density of $V_s = 5060$ m s^{-1} and $\rho_s = 2655$ kg m^{-3}, corresponding to a ST-cut quartz substrate supporting a SSBW, covered by a guiding layer of arbitrary thickness with shear speed $V_l = 1100$ m s^{-1} and density $\rho_l = 2800$ kg m^{-3}, corresponding to the hard-baked S1813 polymer. The horizontal axis is the guiding layer thickness normalised by the intrinsic shear wavelength of the layer $\lambda_l = V_l/f$, where f is the operating frequency of the device. The dotted curves in fig. 5.3 show the corresponding group velocity curves. The maximum slope of the group velocity with normalised guiding layer thickness is steeper than that of the phase speed. By analogy to the definition of phase velocity mass sensitivity, a definition of the mass sensitivity based on the group velocity can be introduced (from Eq. 57 in section 2.5),

$$S_m^{\ g} = \left(\frac{d \log_e V_g}{dm_l} \right)_{d=d_0} = \frac{f_0}{\rho_l V_l} \left(\frac{d \log_e V_g}{dh} \right)_{h=h_0}$$

where $h=d/\lambda_l=df/V_l$ so that a change in guiding layer thickness, d, is equivalent to a change in operating frequency f, m_l is the mass of the layer and the subscript zero implies values of the various quantities at the operating point of the dispersion curve.
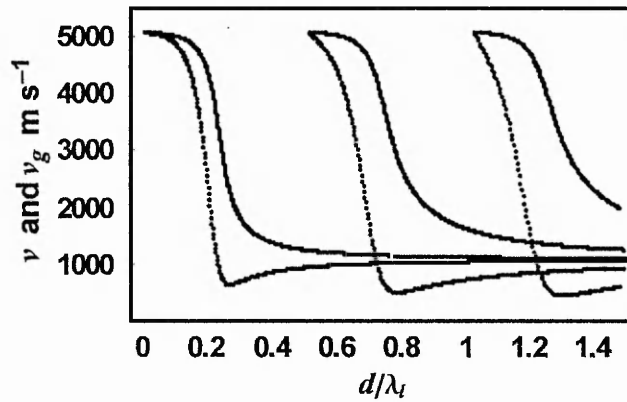
Fig. 5.3   Calculated Love wave (first, second and third modes) phase velocity curves (solid line) for an infinitely thick substrate. The dotted curves show the corresponding group velocity curves.

From comparing the curves in fig. 5.3, it can be noted that this group velocity mass sensitivity, $S_m^{\ g}$, may be larger than the mass sensitivity, S_m, defined using the phase velocity. Whilst this theoretical work related to sensing surface deposited mass, it is also likely that the group velocity defined mass sensitivity of guided SH-SAW (i.e Love wave) devices, when operating in liquid media, may exhibit enhanced sensitivity.

In the remainder of this chapter, the sensitivity of group velocity, phase velocity and insertion loss of a Love wave device to the deposition of a guiding layer and to exposure to a viscoelastic polymer is considered.

5.2.2 Group and phase velocity changes with guiding layer thickness

To investigate the sensitivity of phase and group time delays to liquid loading as a function of guiding layer thickness it was first necessary to characterize changes in these parameters in air. Love wave delay-line devices were designed and fabricated for operation at centre frequency of 110 MHz (from design 2). The guiding layer consisted of spin coated Shipley S1813 photoresist was subsequently hardbaked at 200 °C during 1 hour. A Hewlett Packard 8712ET network analyzer was used to measure the phase, insertion loss and group time delays of the output signal with respect to a reference signal.

Fig. 5.4 shows the effect of the deposition of the photoresist guiding layer on the phase velocity (V_p, solid line with diamonds), the group velocity (V_g, solid line with circles) and the insertion loss (IL, solid line with triangles). Frequency (f) and the group time delay (T_g) were measured at the minimum insertion loss of the signal and plotted against the dimensionless parameter z defined as $z = d/\lambda_{IDT}$, where d is guiding layer thickness and λ_{IDT} is the transducer wavelength. Table 5.1 summarizes the change in resonant frequency, insertion loss, group time delay, group velocity, phase velocity as a function of the guiding layer thickness and the dimensionless parameter z.

The guiding effect of the layer can be seen from the initial reduction in insertion loss and phase velocity with increasing z. These are characteristic features of Love waves generated from SSBWs. A less negative figure for the insertion loss represents more signal transmitted across the delay line and an improved insertion loss. The lowest insertion loss, due to the guiding effect, occurs at $z = 0.02$. Beyond this point, the insertion loss increases and the phase velocity further reduces. The group velocity, as predicted, initially follows the relationship for a constant group speed equal to that of the substrate phase speed and then shows increasing dispersion, which becomes strong after $z = 0.03$. For devices with guiding layers, the group velocity always remains less than the phase velocity.
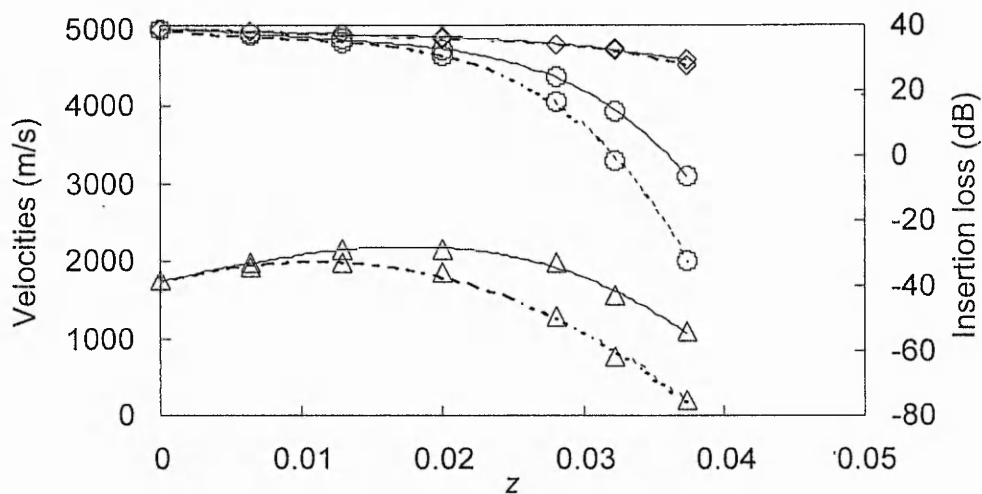
Fig. 5.4   Effect of the deposition of guiding layer to phase velocity (diamonds), group velocity (circles) and to the insertion loss (triangles) in air versus z. The dotted curves show the effect of water loading on phase velocity, group velocity and insertion loss.

d (µm)	z	f (MHz)	IL (dB)	T_g (µs)	V_p (m s^{-1})	V_g (m s^{-1})
0	0	111.334	-38.34	1800	5010.03	5000.00
0.29	0.006	110.538	-33.03	1820	4974.21	4945.05
0.58	0.0128	109.912	-28.8	1850	4946.04	4864.86
0.9	0.02	108.687	-28.66	1900	4890.92	4736.84
1.26	0.028	106.95	-33.22	2050	4812.75	4390.25
1.45	0.032	105.442	-42.76	2280	4744.89	3947.37

Table 5.1   Change in Love wave sensor parameters as a function of guiding layer thickness (d).

The group and phase velocity mass sensitivities can be understood from the slope of the dispersion curves. In a simple interpretation, any surface deposited mass can be viewed as increasing the guiding layer thickness and so moving the operating point of the Love wave further down the curve. For

high mass sensitivity a large change in phase or group velocity is desired for a small surface deposited mass and this corresponds to a large slope in the relevant dispersion curve.

5.2.3 Group and phase velocity changes with liquid loading

A series of liquid sensing experiments were performed using the Love wave device for several values of the guiding layer thickness d, thus setting the operating point z to different locations on the curves in fig. 5.4. At each guiding layer thickness, the device was exposed to deionised water through a flow cell with a continuous flow system. The effect of this water loading on phase and group velocities and insertion loss is indicated by the dotted lines in fig. 5.4; the dotted curve for the phase velocity is virtually indistinguishable from the corresponding solid curve. From fig. 5.4, it is apparent that the liquid loading produces damping of the wave, as an increasing fraction of the signal is lost with increasing guiding layer thickness. Phase velocity was also observed to decrease, although not visibly so on the scale of fig. 5.4, and group time delay increased indicating that the liquid loading reduces the group velocity of the Love wave. For thin layers of wave-guide ($z < 0.02$), water loading has little effect on phase and group velocity. However, for $z > 0.03$, a rapid decrease in group velocity can be observed with a sharper change at $z=0.032$ indicating an increase in sensitivity in group velocity in water compared to air; in contrast the phase velocity shows relatively small changes for the thicker guiding layers. To further investigate the liquid phase sensitivity of the Love wave device with different guiding layer thickness, six solutions of PEG with increasing densities (80, 160, 240, 320, 400 and 480 g l^{-1}) in a successive order of viscosity (the viscosity range of the solutions was 7–310 mPa s) were then passed over the surface of the device. The guiding layer thickness corresponded to increasing z of 0, 0.006, 0.0128, 0.02, 0.028 and 0.032, respectively. In the case of the SSBW propagation, phase change and group time delay are related to density, but only over a limited range. For high density, the viscosity of the solutions needs to be taken in account because

the phase speed sensitivity for shear acoustic wave devices is expected to be proportional to the square root of the viscosity-density product [19].

In fig. 5.5 a) and b) the fractional change in phase velocity (noted $\Delta V_p/V_p$) is plotted against $\sqrt{(\rho_{PEG}\eta_{PEG})}-\sqrt{(\rho_w\eta_w)}$, where the square roots are of the solution product density-viscosity of the PEG solutions and the deionised water solution respectively. The difference in phase velocities in water and PEG, ΔV_p, is calculated using the phase change at resonant frequency and V_p is the unloaded phase velocity for the guiding layer thickness used (see table 5.1). The solid curves in figs. 5.5 are best-fit straight lines and this indicates that the square root dependence on the viscosity-density product is obeyed. It should be noted that the phase shift caused by the initial exposure to the water is greater than would be expected from the $\sqrt{(\rho_w\eta_w)}$ dependence alone. Repeating the experiment such that the initial exposure of the device surface was to PEG rather than water also gave a similar initial phase shift and using the difference in phase velocities in figs. 5.5 effectively cancels a baseline contribution to the response. Fig. 5.6, shows the fractional change in the group velocity, $\Delta V_g/V_g$, where ΔV_g was calculated from the changes in the group time delay for PEG compared to water. In figs. 5.5 and 5.6, group velocity and phase velocity both decrease with increasing wave-guide thickness and exhibit a linear relationship with $\sqrt{(\rho_{PEG}\eta_{PEG})}-\sqrt{(\rho_w\eta_w)}$, over the range considered. As an absolute comparison of the sensitivities to liquids, the change in phase velocity for the highest viscosity PEG solution in fig. 5.5 at a guiding layer thickness corresponding to z=0.032 is 15 m s^{-1}, whereas the group velocity change from figs. 5.5 is 785 m s^{-1}. Although a zero sensitivity in group time delay was found in the case of a bare device, sensitivity in group velocity for devices with guiding layers were found to be substantially larger than in phase velocity. The sensitivity of the Love wave sensor to liquid loading for different guiding layer thicknesses is quantified in fig. 5.7 by plotting the slope of the best-fit straight lines from figs. 5.5 and 5.6. Fig. 5.7 shows that sensitivity in phase velocity (diamonds) is significantly less than the sensitivity in group velocity (circles). Group velocity mass sensitivity increases rapidly with z and the sharp transition at the operating point z=0.032

indicates operation at high sensitivity in viscous liquid. In principle, higher sensitivity may occur for slightly larger guiding layer thickness, but for the devices used in this work this would involve unacceptable reduction in signal strength. This attenuation in signal also accounts for the fact that experimentally the thick guiding layer limit was not obtained for the first Love wave mode where fig. 5.3 predicts a reduction in sensitivity.

In this section, it has been shown that dispersion in guided acoustic wave sensors is an important property when they are used for mass or liquid sensing. The Love wave is a system with strong dispersion and this is intrinsically related to high mass sensitivity for such sensors. A formula giving the phase and group velocity mass sensitivity for deposition of rigidly coupled elastic mass has been considered. This idea has been experimentally extended to viscous liquid loading with poly(ethylene glycol) solutions by using a Love wave device. Group velocity mass sensitivity was found to provide significant enhancement over the phase velocity mass sensitivity at thin and moderate guiding layer thicknesses.
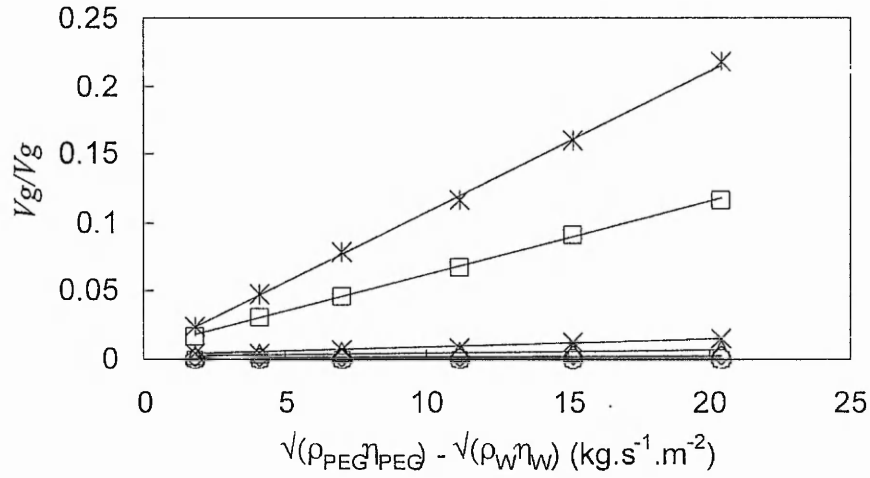
Fig. 5.5 a)   Fractional change in group velocity versus the square root of viscosity-density product of the solutions for increasing operating point $z=d/\lambda_{IDT}$ (circles: $z=0$, diamonds: $z=0.006$, triangles: $z=0.0128$, crosses: $z=0.02$, squares: $z=0.028$, stars: $z=0.032$).

Fig. 5.5 b)   Fractional change in group velocity versus the square root of viscosity-density product of the solutions for increasing operating point $z=d/\lambda_{IDT}$ (circles: $z=0$, diamonds: $z=0.006$, triangles: $z=0.0128$, crosses: $z=0.02$) - zoom from Fig. 5.5 a)

Fig. 5.6   Fractional change in phase velocity versus the square root of density-viscosity product of the solutions for increasing operating point z (circles: $z=0$, diamonds: $z=0.006$, triangles: $z=0.0128$, crosses: $z=0.02$, squares: $z=0.028$, stars: $z=0.032$).

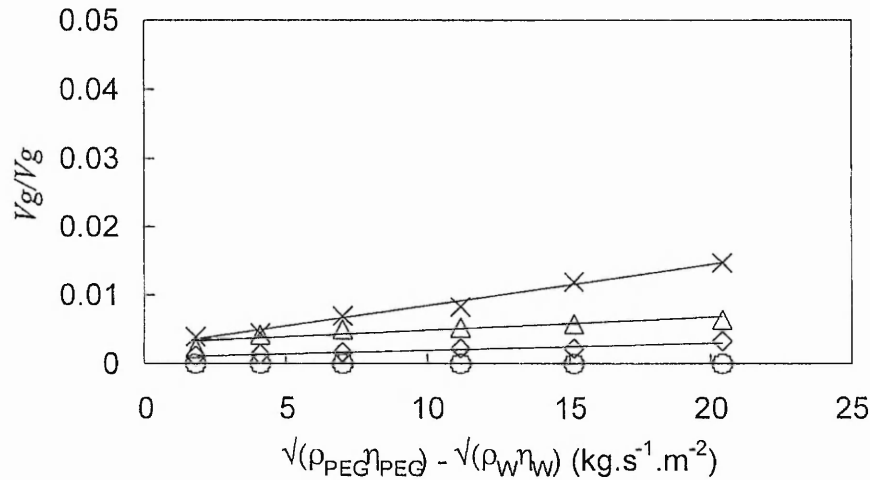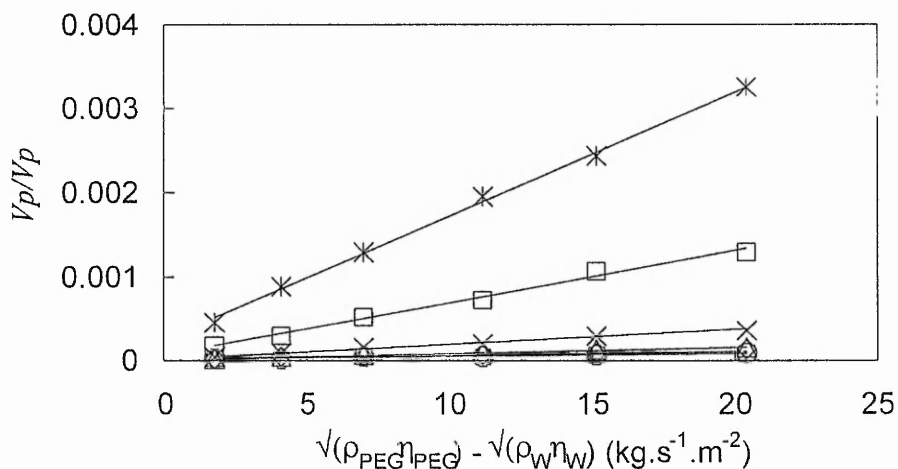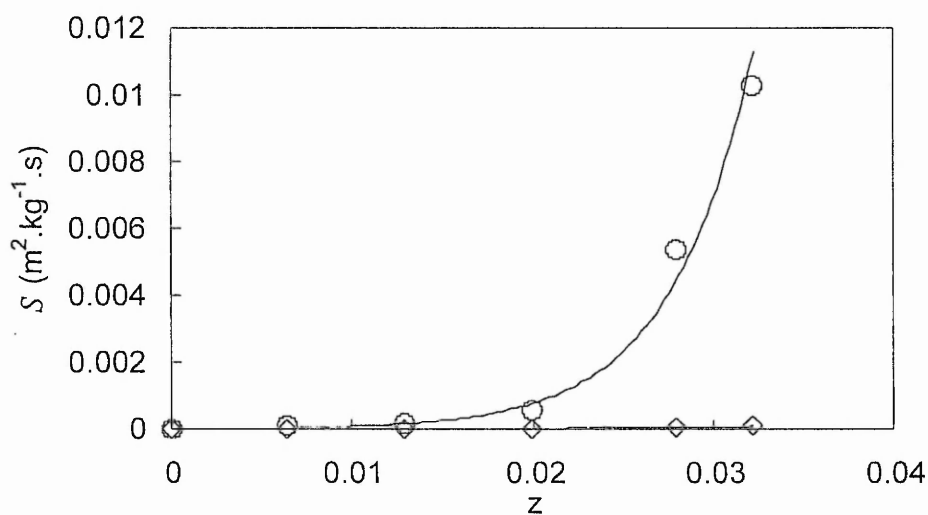**Fig. 5.7**   Gradient of the curves in fig 5.5 and 5.6 (noted S) as a function of z for group velocity (circles) and phase velocity (diamonds).

References

[1] W. P. Mason, Piezoelectric crystals and their application to ultrasonics, Van Nostrand, N. Y., 1950.

[2] B. W. Maxfield, A. Kuramoto, J. K. Hulbert, Mater. Eval., 1987, **45** (10), 1166.

[3] M. Rodahl, F. Hook, C. Frederiksson, C. A. Keller, A. Krozer, P. Brzezinski, M. Voinova, B. Kasemo, Faraday Discuss., 1997, **107**, 229.

[4] G. McHale, M. I. Newton, M. K. Banerjee, S. M. Rowan, Faraday Discuss., 1997, **107**, 15.

[5] R. Chung, R. A. McGill, IEEE Inter. Freq. Contr. Symp., (1998), 634.

[6] M. I. Newton, G. McHale, F. Martin, E. Gizeli, K. A. Melzak, The Analyst, 2001, **126**.

[7] A. C. Stevenson, H. M. Mehta, R. S. Sethi, L. E. Cheran, M. Thompson, I. Davies, C. R. Lowe, The Analyst, 2001, **126**.

[8] K. A. Melzak, E. Gizeli, J. of Colloid and int. sc., (2002), 246.

[9] B. Jakoby, M. J. Vellekoop, Sensors and Actuators A, **68** (1998), 275.

[9] F. Hermann, D. Haan, S. Buttgenbach, Appl. Phys. Lett., **74** (1999), 3410.

[10] G. Kovacs, A. Venema, Appl. Phys. Lett., **61** (1992), 639.

[11] B. Jakoby, M. J. Vellekoop, Ferroelectr. Freq. Control, **45** (1998), 1293.

[12] B. Jakoby, G. M. Ismael, M. P. Byfiled, M. J. Vellekoop, Sensors and Actuators A, **65** (1998), 93.

[13] L. G. Harding, J. Du, Smart. Mater. Struct., **6** (1997), 716.

[14] M.I Newton, G. McHale, F. Martin, E. Gizeli, K. A. Melzak, European Physics Letters, **58** (6) (2002), 818.

[15] M.I Newton, G. McHale, F. Martin, J. Appl. Phys., **91** (2002), 5735.

[16] G. McHale, M.I Newton, F. Martin, J. Appl. Phys., **91** (2002), 9701.

[17] G. McHale, F. Martin, M.I Newton, J. Appl. Phys., (Accepted for publication October 2002).

[18] G. McHale, M. I. Newton, F. Martin, K. A. Melzak, E. Gizeli, Appl. Phys. Lett., **79** (2001), 3542.

[19] A. J. Ricco, S. J. Martin, Appl. Phys. Lett., 50 (1987), 1474.

CHAPTER 6
CONCLUSION AND FUTURE DEVELOPMENTS

CHAPTER 6

CONCLUSION AND FUTURE DEVELOPMENTS

6.1 Conclusion

Bio-sensing applications require high mass sensitivity, which is not provided by a QCM operating at 5-10 MHz. Increasing the operating frequency of the QCM to develop higher mass sensitivity would require thinner crystals, which thus become fragile. In gaseous environments, various bulk modes, Rayleigh waves and Lamb modes have been applied successfully. However, in a liquid environment longitudinal bulk modes and Rayleigh waves suffer from strong radiation losses into the liquid. Therefore, acoustic shear modes, which do not couple elastically to a liquid, are utilized: shear bulk modes, acoustic plate modes and Love modes. It has been shown that a properly designed Love wave sensor is very promising for bio (chemical) sensing in liquids because of its high sensitivity. The use of a waveguide allows the wave to be localized towards the surface and so maximise the sensitivity of the surface to mass attachment from the liquid phase. Traditional Love waves are supported by a semi-infinite thickness substrate and the displacement decays rapidly with depth. In sensor work, they have been regarded as distinct from the acoustic plate modes whereby the substrate is finite and determines a plate resonance.

In chapter 2, a relationship between the slope of the Love wave dispersion curve and the phase velocity mass sensitivity has been derived and a physical interpretation given. Maximum mass sensitivity corresponds to the steepest point on the dispersion curve and so high dispersion. This has consequences for the conversion of fractional changes in phase velocity to fractional changes in frequency, because the group velocity is not equal to the

phase velocity. These theoretical ideas have been considered experimentally in chapters 4 and 5. Chapter 2 has also shown that on a finite thickness substrate there exist generalizations of acoustic plate modes to layer guided acoustic plate modes. Higher order Love waves have been shown to be continuations of these layer guided acoustic plate modes. It has been suggested that layer guided acoustic plate modes combine the advantages of high mass sensitivity with the ability to operate using transducers located on the opposite face to the sensing surface. Furthermore, we showed that dispersion in acoustic wave sensors is an intrinsic and important property when they are used for mass sensing. Dispersion is particularly strong in Love wave sensors and those sensors use this characteristic to produce high mass sensitivity. A formula relating the difference in group and phase velocities to the mass sensitivity has been derived and this formula is applicable to both Love wave and other acoustic wave sensors. Those derivations suggest that the group velocity may be a good sensor parameter. Whilst the theoretical work presented in this chapter was performed in support of the thesis, rather than being the topic of the thesis, it does represent a significant contribution and advance within the subject.

Chapter 3 presented the experimental developments supporting the results of chapters 4 and 5. Whilst much of this chapter was routine, the development of the pulse mode arrangement for Love wave measurements was a new contribution to biosensing. Observation of fast dynamic reactions requires the use of a fast interrogation system. Standard systems employing continuous wave systems, such as the network analyzer, measure a signal that contains unwanted edge reflections and triple transit echoes. The pulse mode system, with its time-of-flight resolved information, was able to identify spurious reflections, discriminate between different acoustic modes and could be used to optimise the sensitivity of devices. The basic calibration of the pulse mode system using liquid solutions was presented in chapter 3 with the use of the pulse mode system for a study of vesicle deposition presented later in chapter 5.

In chapter 4, resonant conditions for higher order Love wave modes have been observed by systematically increasing the waveguide thickness. Data was presented for both phase velocity and insertion loss and it was shown that the trend in insertion loss of a Love wave device on quartz was not accurately predicted by Love wave theory. A comparative study of Love waves generated from surface skimming bulk wave and shear horizontal modes on lithium tantalate demonstrated that the reduction in insertion loss initially observed with thin guiding layers on quartz was due to wave guiding of the surface skimming bulk wave. Subsequently, a study of the insertion loss sensitivity to elastic, visco-elastic and viscous loading of the Love wave higher order modes was presented. This chapter concluded by showing that the insertion loss can be a useful sensor parameter for studying not only liquid-phase response, but also mass deposition response. Viscous loading mass sensitivity in insertion loss and phase for higher order Love modes were found to be within a factor of 2 or 3 comparable to the first Love mode. Therefore, sensing using higher order Love wave modes is possible and is suitable for liquid phase applications such as (bio) chemical sensors. This should enable alternative polymer materials producing thicker guiding layers to be considered for use with Love wave devices. The observation of multiple Love wave modes and the development of the concept of insertion loss sensitivity, particularly to the deposition of elastic mass, are significant and new results of this thesis.

Chapter 5 focused on the use of pulsed RF techniques within Love wave sensing. In the initial part of the chapter, the pulse mode amplitude and phase measurement system developed in chapter 3 was applied to a model biosensing experiment. The system was shown to be capable of monitoring the deposition and removal of vesicles with low noise and a high sampling rate. Phase and insertion loss information were obtained and low-level species detection achieved (200 μg ml^{-1}) by using the pulse excitation technique. In this section 2.5, we showed that dispersion in acoustic wave sensors is an intrinsic and important property when they are used for mass sensing. Love wave sensors use dispersion to produce high mass sensitivity

and the group velocity was shown to be an important sensing parameter in chapter 2.5. In chapter 5, by using a continuous wave system, Love wave mass sensitivity from group and phase velocities measurements has been investigated for visco-elastic sensing and liquid loading. Results have been confirmed by using the pulse mode system and it's been concluded that both systems produce intrinsic dispersion. Furthermore, group velocity exhibits a higher mass sensitivity than the phase velocity. It's been also suggested that the group velocity could be used for a direct estimation of the mass sensitivity of Love wave sensors and other acoustic wave sensors. The development and testing of this new pulse mode system, the experimental investigation of the group velocity related mass sensitivity represent a significant achievement in this thesis.

6.2 Future developments

The results presented in this thesis open new directions for future work. Three points of interest can be seen:

1. **Experimental demonstration of layer guided acoustic plate modes**
    Fig. 6.1, 6.2 show preliminary experimental results for the dispersion curve of a 25 MHz surface skimming bulk wave (SSBW) mode device with the mode converted to a Love wave by a photoresist layer deposited by spin-coating. The basic uncoated SSBW device was fabricated with propagation orthogonal to the x-axis of a thinned (250 μm) ST-cut quartz substrate. The mask used to produce the device was not specifically designed for studying acoustic plate modes. However, thinning of the substrate did enable the plate modes to be observed and the shift in resonant frequency with guiding layer thickness to be evaluated, although the insertion loss was too high for direct evaluation of the sensor response. The frequency spectrum of

the device is shown in Fig. 6.1, where the SSBW resonates at ~ 25 MHz and 9 plate modes are observed at higher frequencies.
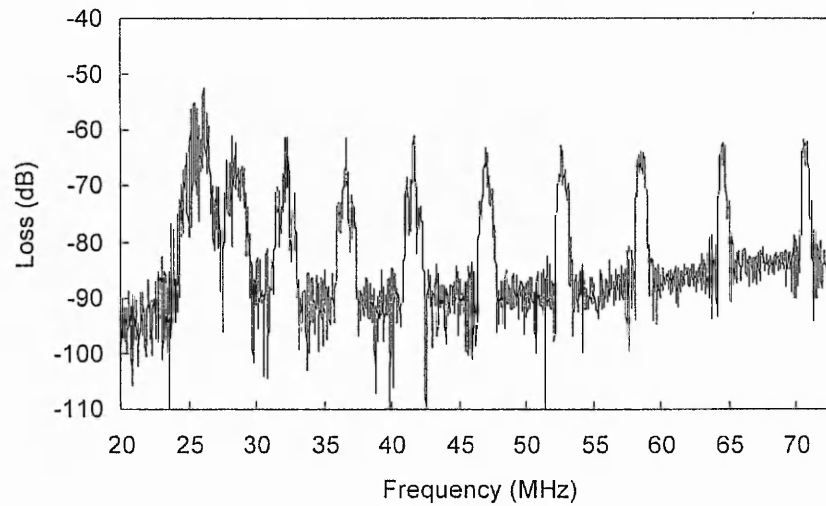
Fig. 6.1   Spectrum of a 25 MHz SSBW device on 250 μm thick ST-cut quartz substrate. 9 plate modes can be distinguished.

In fig. 6.2, the horizontal axis shows the guiding layer thickness scaled by the frequency of operation and shear speed in the layer ratio ($d.f/V_l$). Each successive plate mode is indicated by open circles and the Love wave modes, three in total, are indicated by open squares. Fig. 6.2 a) shows the results when the transducers face is coated, 6.2 b) when the face opposite to the transducers is coated (open circles and open squares for the layer guided SH-APM and the Love wave respectively). 6.2 c) shows the results when the transducers face is coated only (open circles and open squares for the layer guided SH-APM and the Love wave respectively) and when, subsequently, the opposite is coated only (solid circles and solid squares for the layer guided SH-APM and the Love wave respectively). These results tend to confirm the predicted generalizations of Love wave theory (section 2.4) and the experimental results in section 4.1.

a)

b)

c)
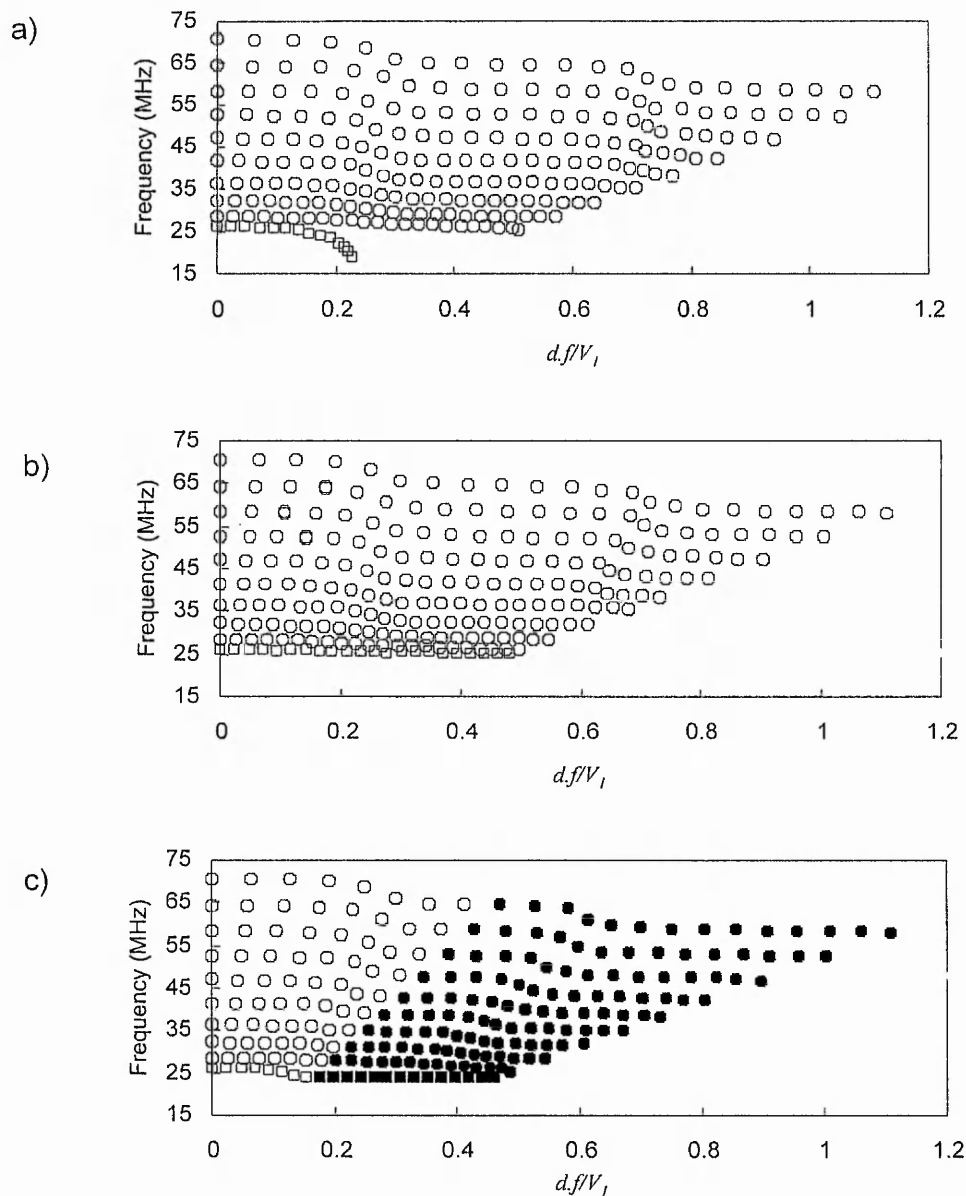
Fig. 6.2   Operating frequency as a function of normalized wave-guide thickness. In a) and b) cascading layer guided plate modes are indicated by open circles and the Love wave by open squares. In c), cascading layer guided plate modes and the Love are indicated by open circles and open squares respectively when the sensor is coated on the transducers face only and in solid circles and solid squares when the sensor is coated on the opposite face only.

This new class of acoustic wave sensors is very promising as they would combine the high sensitivity of Love wave devices with the ability of shear horizontal acoustic plate mode sensors to operate in the liquid-phase without immersion of the face containing the transducers. Future work could examine the effect of new designs on the excitation of acoustic plate modes and layer guided acoustic plate mode and their direct application as mass and liquid sensors.

2.   High frequency operation of Love wave devices

Higher fundamental frequency operation for SAW devices can be achieved by fabricating IDTs with a smaller period. The maximum Love wave mass sensitivity for the phase velocity then requires a correspondingly thinner film to maintain the operating point on the dispersion curve for the first Love mode at the maximum slope. In this case, the mass sensitivity, defined using the phase velocity, scales directly with frequency. In SAW device design, higher fundamental frequency requires smaller finger widths in the IDTs and this presents fabrication problems. The alternative used in this thesis was to design IDTs that can work at harmonic frequencies. Increasing the frequency to the higher harmonic can place the operating point on a lower point of the dispersion curve. Alternatively, it may produce a jump in the Love wave mode and hence convert the operating point from a high slope on the first mode to a substantially smaller slope on the second mode. Although the wave-guiding effect has been demonstrated at 940 MHz (section 4.1) by operating at the third harmonic, the low signal level did not allow direct application as a mass or liquid sensor. Further work would include examining the impact of frequency on the mass sensitivity of Love wave sensors by fabricating Giga-Hertz range Love wave sensors by using sub-micron technology. In principle, it would also be possible to create a sensor that could be hopped between the first four Love modes by using a double-double finger IDT design with unequal finger-gap widths. Such a device could be operated at

frequencies of f, $3f$, $5f$ and $7f$, and so permit more information about the probed visco-elasticity to be extracted.

3.   **Group velocity**

Measurements of the propagation time delay of a pulse do not give the phase velocity as the group velocity is not equal to the phase velocity. In a pulse experiment (or by group time delay measurement using a network analyser), the high slope in the dispersion curve means the speed of each frequency component in the pulse differs significantly. This has a significant impact on the phase velocity measurement by the pulse excitation system. Achieving significant accuracy in group time delay was found to be difficult. However group velocity proved to show enhanced sensitivity to liquid loading compared to the phase velocity (sections 2.5 and 5.2) and it may therefore be of value to develop a sensor configuration based on changes in group velocity. In addition, the formula using group velocity to determine phase velocity mass sensitivity could be extended to a wide range of other acoustic wave sensors, for example to the QCM by considering the zero thickness limit of a polymer layer. Further work could include examining the effect of dispersion and group velocity on surface transverse wave sensors and layer guided acoustic plate mode sensors.

APPENDIX A

APPENDIX A
LAYER GUIDED SHEAR HORIZONTALLY POLARISED ACOUSTIC PLATE MODES

The following appendix describes the mathematical developments of section 2.4. These developments are directly extracted from the paper entitled "Layer guided shear horizontally polarised acoustic plate modes" and published by G. McHale, M. I. Newton and F. Martin in Journal of Applied Physics, (**91**, (2002), 5735-5744).

A.1 Theoretical Formulation

Consider waves motion in an isotropic and non-piezoelectric material of density ρ and with Lamé constants λ and μ. The displacements, u_j, are then described by the equation of motion,

$$\rho \frac{\partial^2 u_j}{\partial t^2} = (\lambda + \mu) \frac{\partial S_{ii}}{\partial x_j} + \mu \underline{\nabla}^2 u_j \tag{1}$$

where the Einstein summation convention has been used and the strain tensor, S_{ij}, is defined as,

$$S_{ij} = \frac{1}{2} \left(\frac{\partial u_i}{\partial x_j} + \frac{\partial u_j}{\partial x_i} \right) \tag{2}$$

The boundary conditions on any solution require consideration of the stress tensor, T_{ij}, which can be written in the form,

$$T_{ij} = \lambda \delta_{ij} S_{kk} + 2\mu S_{ij} \tag{3}$$

In the combined Love wave and SH-APM problem, we consider a substrate of thickness, w, with a density ρ_s and Lamé constants λ_s and μ_s overlayed by a uniform mass layer of thickness, d, and with a density ρ_l and Lamé constants λ_l and μ_l. In analogy to Love wave theory, the uniform mass overlayer will also be referred to as the guiding layer. The upper surface of the substrate is taken to be in the (x_1, x_2) plane and located at $x_3 = 0$ (fig. A.1). The solutions of the equation of motion are chosen to have a propagation along the x_1 axis with displacements in the x_2 direction of the sagittal plane (x_2, x_3). They must also satisfy the boundary conditions that both $\underline{u}$ and the T_{i3} component of the stress tensor are continuous at the interface between the substrate and layer and that the T_{i3} component of the stress tensor vanishes at the free surfaces of the substrate and layer at $x_3 = -w$ and $x_3 = d$, respectively. In order to preserve the notational similarity with the Love wave problem, a solution for the equation of motion is sought by using displacements in the layer, $\underline{u}_l$, and the substrate, $\underline{u}_s$, of

$$\underline{u}_l = (0,1,0)\left[A_l e^{-j\Gamma_l x_3} + B_l e^{j\Gamma_l x_3}\right]e^{j(\omega t - k_1 x_1)} \tag{4}$$

and

$$\underline{u}_s = (0,1,0)\left[C_s e^{\Gamma_s x_3} + D_s e^{-\Gamma_s x_3}\right]e^{j(\omega t - k_1 x_1)} \tag{5}$$

where ω is the angular frequency and the wave vector is $k_1 = (\omega/V)$ where V is the phase speed of the solution. A_l, B_l, C_s and D_s are constants determined by the boundary conditions.
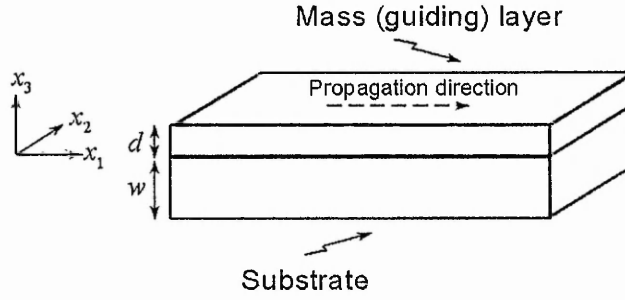
Figure A.1: Definition of axes and propagation direction for shear horizontally polarized waves in a system of a finite substrate covered by a finite mass guiding layer; the displacement is in the x_2 direction.

A traditional Love wave solution occurs when the substrate thickness w $\rightarrow\infty$, the shear speed of the substrate, $V_s = (\mu_s/\rho_s)^{1/2}$, is greater than the shear speed of the layer, $V_l = (\mu_l/\rho_l)^{1/2}$, and the wave vector Γ_s is real, so that the solution, $\underline{u}_s$, decays with depth into the substrate. A traditional SH-APM solution occurs when $d \rightarrow 0$ and the wave vector Γ_s is purely imaginary, so that the solution, $\underline{u}_s$, may take on a standing wave (resonant) form. In the more general case under consideration here, both Γ_l and Γ_s may be complex rather than real. The use of the exponentials with a j factor in Eq. (4) and without a j factor in Eq. (5) is therefore purely to enable the similarity with the Love wave theory to be more readily noted. Substituting Eq. (4) into the equation of motion describing the substrate, i.e. Eq. (1) with the substrate parameters, gives the equation for the wave vector Γ_s,

$$\Gamma_s^2 = \omega^2\left(\frac{1}{V_2} - \frac{1}{V_s^2}\right)$$

(6)

Similarly substituting Eq. (5) into the equation of motion describing the layer, gives

$$\Gamma_l^2 = \omega_2\left(\frac{1}{V_l^2} - \frac{1}{V_2}\right) \tag{7}$$

To completely specify the problem the boundary conditions are imposed and this defines the constants A_l, B_l, C_s and D_s in Eqs. (4) and (5). The first boundary condition is continuity of the displacement at the interface between the substrate and the layer at $x_3=0$ and this gives,

$$A_l + B_l = C_s + D_s \tag{8}$$

The remaining conditions all relate to the Γ_{i3} component of the stress tensor, which for this system using the form of the solutions in Eqs. (4) and (5) can be written as,

$$\Gamma_{i3} = \delta_{i2}\mu\left(\frac{\partial u_2}{\partial x_3}\right) \tag{9}$$

The second boundary condition, continuity of T_{i3} at the substrate-layer interface, gives,

$$-A_l + B_l = -j(C_s + D_s)\xi \tag{10}$$

where ξ has been defined as,

$$\xi = \frac{\mu_s\Gamma_s}{\mu_l\Gamma_l} \tag{11}$$

The remaining two boundary conditions are continuity of stress at the two free surfaces at $x_3=d$ and $x_3=-w$, and these give the equations,

---

$$A_l \exp(-j\Gamma_l d) - B_l \exp(j\Gamma_l d) = 0 \tag{12}$$

and

$$C_s \exp(-\Gamma_s w) - B_s \exp(\Gamma_s w) = 0 \tag{13}$$

Solving the boundary conditions, Eqs (8), (10), (12) and (13), gives both a dispersion equation,

$$\tan(\Gamma_l d) = \xi \tanh(\Gamma_s w) \tag{14}$$

and the solutions for the displacements,

$$\underline{u}_l = (0,1,0) A \exp(-\Gamma_s w)\left[\cosh(\Gamma_s w)\cos(\Gamma_l x_3) + \xi \sinh(\Gamma_s w)\sin(\Gamma_l x_3)\right] e^{j(\omega t - k_1 x_1)} \tag{15}$$

and

$$\underline{u}_s = (0,1,0) A \exp(-\Gamma_s w)\cosh\left[\Gamma_s(x_3 + w)\right] e^{j(\omega t - k_1 x_1)} \tag{16}$$

where ξ is defined by Eq. (11) and A is a constant. Using the dispersion equation (Eq. (14)) the layer displacement may be re-written as,

$$\underline{u}_l = (0,1,0) A \exp(-\Gamma_s w)\cosh(\Gamma_s w)\left[\cos(\Gamma_l x_3) + \tan(\Gamma_l d)\sin(\Gamma_l x_3)\right] e^{j(\omega t - k_1 x_1)} \tag{17}$$

A.2 Structure of solutions

The dispersion equation (Eq. (14)) is highly non-linear, but can nonetheless be solved numerically and the phase speed obtained for the various possible modes for given substrate and layer depths with specific material properties (shear speeds, densities, etc). However, it is useful for matching the theory to Love wave and SH-APM theory to consider the

perturbation solutions for finite thickness substrates covered by mass layers of small thickness. Before performing a perturbation expansion, it is instructive to consider the structure of the dispersion equation and how it relates to Love waves and SH-APM's and to multiple modes.

a) Love waves

When Γ_s is real and positive and the substrate thickness $w \to \infty$, the dispersion equation (Eq. (14)) reduces to the dispersion equation for the Love wave case,

$$\tan(\Gamma_l d) = \xi \tag{18}$$

When Γ_s is real and positive, but w is finite we have a solution with a substrate displacement that decays with depth and which can therefore be regarded as a Love wave solution on a finite substrate. This finite substrate Love wave case contains multiple Love wave modes due to the $\tan(\Gamma_l d)$ term. At the start of each of these modes the conditions satisfied are,

$$\tan(\Gamma_l d) = 0 \tag{19}$$

and

$$\xi = \frac{\mu_s \Gamma_s}{\mu_l \Gamma_l} = 0 \tag{20}$$

so that the phase speed at the start of each mode is given from Eq. (6), using $\Gamma_s = 0$, as $V = V_s$ and the start of the multiple Love wave modes are given by $\Gamma_l d = n\pi$ where $n = 0, 1, 2, \ldots.$ As the thickness, d, of the guiding layer increases, the phase speed decreases non-linearly from a value equal to the shear speed of the substrate towards the value of the shear speed of the layer, V_l. The existence of multiple modes means that we can consider a perturbation expansion about the start of each mode, rather than simply about

---

a zero thickness mass layer. Essentially, the perturbation theory for higher Love wave modes starts at a finite guiding layer thickness and is a perturbation of the phase speed from the value of the substrate shear speed. A necessary part of the Love solution is that the phase speed is equal to or less than the phase speed of the substrate. It is this condition that guarantees Γ_s real and an exponential decay of the displacement with depth into the substrate.

b) SH-APM's

The dispersion equation (Eq. (14)) reduces to the dispersion equation for the SH-APM case when Γ_s is purely imaginary, the substrate thickness w is finite and the mass overlayer vanishes ($d{\to}0$). In this case, it is possible to write $\Gamma_s = jk_s$ with k_s real. The dispersion equation then requires either $\xi=0$ or a solution of the equation,

$$\tan(k_s w) = 0 \tag{21}$$

The possible solutions of Eq (21) are the different resonating modes of the SH-APM and are,

$$k_s = \frac{m\pi}{w}, \, m = 0, 1, 2, 3, .. \tag{22}$$

Substituting Eq (22) into Eq (6) gives the phase speed,

$$V_m = \frac{V_s}{\sqrt{1 - \left(\frac{m\pi V_s}{W\omega}\right)^2}} \tag{23}$$

where the subscript m has been added to the phase speed, V, to indicate its dependence on the mode number. Thus, the phase speeds of the SH-APM

modes are either equal to or greater than the shear speed of the substrate. It is this condition that guarantees Γ_s imaginary and a standing wave resonance in the substrate.

c) Love waves and Layer Guided APM's

In the case that a SH-APM occurs (i.e. Γ_s is purely imaginary), but a finite thickness mass overlayer exists, there will be a set of solutions to Eq (14) for every value of d. Moreover, as the overlayer thickness increases, the phase speed associated with each of these modes will decrease. For this reason, the $m=0$ SH-APM mode used in sensing, should not be regarded as a SH-APM mode at all. The slightest mass loading will lower its phase speed to below that of the substrate so that the wavevector in the substrate will change from imaginary to real and it will therefore become the first Love wave mode. Eq. (23) also shows that for any given frequency there is a maximum number of SH-APM modes, m_{max}, since the phase speed, V_m, must be finite,

$$m_{\max} = \frac{W\omega}{\pi V_s} \tag{24}$$

In the solution of the full dispersion equation (Eq. (14)), the guiding layer thickness and the phase speed can be chosen to simultaneously satisfy both the Love wave condition $\tan(\Gamma_l d)=0$ and the SH-APM condition $\tan(k_s w)=0$. The thickness, d_{nm}, and the phase speed, V_m, at which modes satisfies these conditions can be regarded as the start of a mode; this definition of the start of a mode is then consistent with the traditional view of the start of a Love wave mode. The thickness at which a mode starts is then given from Eq. (19) and Eq. (23) as,

$$\frac{d_{nm}}{\lambda_l} = \frac{n}{2\sqrt{1-\left(\dfrac{V_l}{V_m}\right)^2}} = \frac{n}{2\sqrt{1-\left(\dfrac{V_l}{V_s}\right)^2\left[1-\left(\dfrac{m\lambda_s}{2w}\right)^2\right]}} \tag{25}$$

where $n=0,1,2,3,\ldots$ labels the successive Love wave modes and $m=1,2,3,\ldots$ labels the acoustic plate modes associated with each Love wave mode. As the thickness of the guiding layer increases, the phase speed of each plate mode associated with a particular Love wave mode decreases until at some guiding layer thickness it attains the value of the next lower plate mode associated with the next higher order Love wave mode.

A.3 Perturbation Solutions

In the previous section the structure of the solutions to the dispersion equation (Eq. (14)) has been discussed and the similarities with Love waves and SH-APM's has been illustrated. In addition, the effect on Love waves of a finite thickness substrate and on SH-APM's of a guiding layer has also been highlighted. In order to convincingly demonstrate that the theoretical formulation does encompass traditional Love waves and SH-APM's, perturbation theory is used in this section to obtain the limiting case of small mass loading whose results are known in the literature. Consider a perturbation, Δd, of the guiding layer thickness, d, from $d=0$ for the $n=0$ Love wave and associated SH-APM's. The phase speed of the unperturbed case of no guiding layer is known and given by Eq. (23) and this perturbation will result in a decrease in the phase speed of the mode. The perturbation $d=0 \rightarrow d=\Delta d$ will cause changes in the phase speed and the wavevectors and we can therefore write $\Gamma_l{}^0 \rightarrow \Gamma_l{}^0 + \Delta\Gamma_l$, $\Gamma_s{}^0 \rightarrow \Gamma_s{}^0 + \Delta\Gamma_s$ and $\xi^0 \rightarrow \xi^0 + \Delta\xi$ where the superscript zero indicates the values of the quantities when $d=0$. The dispersion equation (Eq. (14)) can then be written,

$$\tan(\Gamma_l{}^0 \Delta d) \approx \frac{(\xi_0 + \Delta\xi)\tanh(\Delta\Gamma_s w) + \Delta\xi\tanh(\Gamma_s{}^0 w)}{1 + \tanh(\Gamma_s{}^0 w)\tanh(\Delta\Gamma_s w)} \tag{26}$$

Further approximation depends on whether the mode being perturbed is a Love wave ($\xi^0 = 0$) or one of the associated $m>0$ SH-APM's ($\tanh(\Gamma_s{}^0 w)=0$, but $\xi^0 \neq 0$).

---

a) Love wave case

The $n=0$ Love wave case satisfies $\xi^o=0$ and this requires $\Gamma_s^o=0$ so that, from Eq. (6), $V^o=V_s$. Eq. (26) reduces to,

$$\tan(\Gamma_l^o\Delta d)\approx\Delta\xi\tanh(\Delta\Gamma_s w) \qquad (27)$$

Considering the definition of ξ (Eq. (20)) the perturbation $\Delta\xi$ can be written in terms of the wavevectors and their perturbations,

$$\Delta\xi\approx\frac{\mu_s\Delta\Gamma_s}{\mu_l\Gamma_l^o} \qquad (28)$$

The perturbation in Γ_s arises from the perturbation to the phase speed and is given from Eq. (6) as,

$$\Delta\Gamma_s\approx\frac{\omega}{V_s}\sqrt{\frac{-2\Delta V}{V_s}} \qquad (29)$$

Eq (27) therefore becomes,

$$\tan(\Gamma_l^o\Delta d)\approx\frac{\mu_s\omega}{\mu_l V_s\Gamma_l^o}\sqrt{\frac{-2\Delta V}{V_s}}\tanh\left(\frac{\omega w}{V_s}\sqrt{\frac{-2\Delta V}{V_s}}\right) \qquad (30)$$

where

$$\Gamma_l^o=\omega\sqrt{\frac{1}{V_l^2}-\frac{1}{V_s^2}} \qquad (31)$$

The left-hand side of Eq. (30) is similar in form to that used in acoustic load impedance models of quartz crystal microbalances. In QCM models, the acoustic load, Z_L, on the crystal due to a thin mass layer is

$Z_L=j(\mu_l/V_l)\tan(\omega\Delta d/V_l)$ and the periodicity in this causes shear wave resonances[10-12]. To first order in the mass layer thickness Eq. (30) becomes,

$$\Delta d \approx \frac{\mu_s V_s \sqrt{\dfrac{-2\Delta V}{v_s}}}{\mu_l\omega\left(\dfrac{V_s^2}{V_l^2}-1\right)}\tanh\left(\frac{\omega w}{V_s}\sqrt{\frac{-2\Delta V}{V_s}}\right) \qquad (32)$$

The result in Eq. (32) gives the perturbation in the phase speed due to the presence of a small mass layer acting as a wave-guide on a finite thickness substrate. The traditional Love wave assumes an infinitely thick substrate and this can be obtained by taking the limit $w\rightarrow\infty$, so that the tanh() term tends to unity. This gives,

$$\frac{\Delta V}{V_s} \approx -\frac{1}{2}\left[\frac{\mu_l\left(\dfrac{V_s^2}{V_l^2}-1\right)\omega\Delta d}{\mu_s V_s}\right]^2 \qquad (33)$$

Thus, a thin mass layer acting as a Love wave guide on an infinite thickness substrate generates a fractional shift in the phase speed proportional to the square of the product of the frequency and mass thickness (or frequency and mass per unit area). In many practical situations the substrate phase velocity is much larger than the layer phase speed and Eq. (33) can be further simplified.

b) SH-APM with $m=0$

In this sub-section a perturbation expansion is used for the $m=0$ SH-APM and a result identical to that existing in the literature is obtained. It is then shown that this result is in error due to the perturbation being about a singular point which means that a perturbed $m=0$ SH-APM mode becomes a

Love wave rather than remaining as a SH-APM. The zeroth order plate mode is given by a finite thickness substrate with $\Gamma_s = jk_s$ and $k_s w = 0$. This necessarily means it also satisfies the Love wave condition for the unperturbed system of $\xi^0 = 0$ and, from Eq. (6), the unperturbed phase speed is V_s. The perturbation expansion of the dispersion equation (Eq. (14)) follows the finite thickness substrate Love wave case and Eqs (30)-(32) are obtained. However, in the SH-APM case the substrate thickness remains finite and we expand the tanh() term on the right hand side of Eq. (30),

$$\frac{\Delta V}{V_s} \approx \frac{-\mu_l V_s}{2\mu_s w \omega} \sqrt{\frac{V_s^2}{V_l^2} - 1} \tan\left(\sqrt{\frac{V_s^2}{V_l^2} - 1} \frac{\omega \Delta d}{V_s} \right) \tag{34}$$

Again, Eq (30) has been used initially, rather than going directly to Eq. (33), in order to preserve the similarity in form to acoustic impedance models of QCM's. Expanding in small layer thickness gives,

$$\frac{\Delta V}{V_s} \approx \frac{-\mu_l}{2\mu_s} \left(\frac{V_s^2}{V_l^2} - 1 \right) \frac{\Delta d}{w} \tag{35}$$

which can be re-written using $V_s = (\mu_s/\rho_s)^{1/2}$ and $V_l = (\mu_l/\rho_l)^{1/2}$. In the approximation that $(V_s/V_l)^2 \gg 1$, Eq. (35) reduces to,

$$\frac{\Delta V}{V_s} \approx \frac{-\rho_l \Delta d}{2\rho w_s} \tag{36}$$

which is precisely the result given by Martin *et al* for the sensitivity of the SH-APM mode 0 to small mass perturbations. However, we argue that the above calculation is in fact in error due to the perturbation being singular. The problem arises because the predicted velocity shift is negative and this must reduce the phase speed to a value below that of the substrate. However, in this case Eq. (6) predicts that Γ_s^2 will be positive and so the assumption that

---

$\Gamma_s = jk_s$ with k_s real can no longer be valid. In effect, when the phase speed of the $m=0$ SH-APM is perturbed by a mass layer of shear speed lower than the substrates, the solution necessarily converts into a Love wave.

c) SH-APM with $m>0$

The higher order SH-APM's associated with the Love wave do not suffer the same difficulty as the $m=0$ SH-APM. In this case, the unperturbed solution has $\tanh(\Gamma_s^o w)=0$ with $\Gamma_s^o = jk_s^o$ and k_s^o real, but with $\xi^o \neq 0$. Thus, the unperturbed phase speed V_m^o of the mth mode is not equal to the shear speed of the substrate V_s and it is possible to perturb the phase speed without breaking the assumption that k_s is real and so retain a SH-APM mode. In the $m>0$ SH-APM case, Eq. (26) reduces to,

$$\tan(\Gamma_l^o \Delta d) \approx \xi^o \tanh(\Delta \Gamma_s w) \qquad (37)$$

and Eq. (6) gives,

$$\Delta \Gamma_s \approx \frac{-\omega^2}{V_s} \frac{\Delta V}{V_m^3} \qquad (38)$$

Thus, the equivalent of Eq. (30) is,

$$\tan(\Gamma_l^o \Delta d) \approx \frac{\mu_s \omega}{\mu_l V_m \Gamma_l^o} \sqrt{\frac{V_m^2}{V_s^2}-1} \tan\left(\frac{\omega w}{V_m \sqrt{\frac{V_m^2}{V_s^2}-1}} \left(\frac{-\Delta V}{V_m} \right) \right) \qquad (39)$$

where Γ_l^o is given by

$$\Gamma_l^o = \omega \sqrt{\frac{1}{V_l^2}-\frac{1}{V_m^2}} \qquad (40)$$

Significant differences between Eq. (30) describing Love waves and Eq. (39) describing SH-APM's include the replacement of the $\tanh(\ )$ on the right-hand

Appendix A

side by a tan( ) term, the replacement of the $(-2\Delta V/V_s)^{1/2}$ by $(-\Delta V/V_m)$ in the argument of the tan( ) and the lack of a pre-factor involving the perturbation to the phase speed. A further difference is the presence of a $(V_m^2/V_s^2-1)^{1/2}$ as a pre-factor to the tan( ) and in the denominator of the argument of the tan( ). This factor is responsible for the difficulties with the m=0 SH-APM mode because when m=0 the unperturbed phase speed, V_m, is equal to the substrate phase speed, V_s, and the factor vanishes, thus giving a singularity in the argument of the tan( ) term. However, if this singularity is formally ignored and the tan( ) is expanded to first order, the factor from the argument cancels with the factor in the pre-factor and an apparent result for the perturbation to the phase speed can be obtained. We believe this formal perturbation result for the m=0 SH-APM mode is invalid and that, in fact, the mode becomes a Love wave with the perturbation to the phase speed described by Eq. (30).

For the m>0 SH-APM modes, Eq. (39) can be written to first order in Δd as,

$$\Delta d \approx \frac{\mu_s V_m \sqrt{\frac{V_m^2}{V_s^2}-1}}{\mu_l \omega \left(\frac{V_m^2}{V_l^2}-1\right)} \tan\left(\frac{\omega w}{V_m\sqrt{\frac{V_m^2}{V_s^2}-1}}\left(\frac{-\Delta V}{V_m}\right)\right) \tag{40}$$

and expanding to first order in ΔV gives,

$$\frac{\Delta V}{V_m} \approx \frac{-\mu_l}{\mu_s}\left(\frac{V_m^2}{V_l^2}-1\right)\frac{\Delta d}{w} \tag{41}$$

which is a factor of two greater than Eq. (35). Eq. (23) can be used to evaluate the mode speed V_m from the substrate speed and thickness and the operating frequency. In the case that the unperturbed SH-APM modes are close in phase speed to the substrate phase speed, i.e. $V_m \approx V_s$, and the

substrate speed is much greater than the layer phase speed, i.e. $V_m^2 >> V_l^2$, Eq. (41) can be reduced to,

$$\frac{\Delta V}{V_s} \approx \frac{-\rho_l \Delta d}{\rho_s w} \qquad (42)$$

APPENDIX B

APPENDIX B
THEORETICAL MASS SENSITIVITY OF LOVE WAVE AND LAYER GUIDED ACOUSTIC PLATE MODES

The following appendix describes the mathematical developments of section 2.4.3. These developments are directly extracted from the paper entitled "Theoretical mass sensitivity of Love wave and layer guided acoustic plate modes" and published by G. McHale, M. I. Newton and F. Martin in Journal of Applied Physics, (**91** (2002), 9701-9712.).

B.1 Theoretical Formulation

Consider wave motion in an isotropic and non-piezoelectric material of density ρ and with Lamé constants λ and μ. The displacements, u_j, are then described by the equation of motion,

$$\rho \frac{\partial^2 u_j}{\partial t^2} = (\lambda + \mu) \frac{\partial S_{ii}}{\partial x_j} + \mu \underline{\nabla}^2 u_j \tag{1}$$

where the Einstein summation convention has been used and the strain tensor, S_{ij}, is defined as,

$$S_{ij} = \frac{1}{2} \left(\frac{\partial u_i}{\partial x_j} + \frac{\partial u_j}{\partial x_i} \right) \tag{2}$$

The boundary conditions on any solution require consideration of the stress tensor, T_{ij}, which can be written in the form,

$$T_{ij} = \lambda \delta_{ij} S_{kk} + 2\mu S_{ij} \tag{3}$$

The upper surface of the substrate is taken to be in the (x_1,x_2) plane and located at $x_3=0$ (fig. B.1). The solutions of the equation of motion are chosen to have a propagation along the x_1 axis with displacements in the x_2 direction of the sagittal plane (x_2,x_3). They must also satisfy the boundary conditions on the displacements $\underline{u}$ and the T_{i3} component of the stress tensors. These must both be continuous at the interfaces between the substrate and guiding layer, and between the guiding layer and perturbing mass layer. The T_{i3} component of the stress tensors must also vanish at the free surfaces of the substrate and the perturbing mass layer at $x_3=-w$ and $x_3=(d+h)$, respectively.

In order to preserve the notational similarity with the Love wave problem, a solution for the equation of motion is sought by using displacements in the guiding layer, $\underline{u}_l$, the substrate, $\underline{u}_s$, and the perturbing mass layer, $\underline{u}_p$, of

$$\underline{u}_l = (0,1,0)\left[A_l e^{-j\Gamma_l x_3} + B_l e^{j\Gamma_l x_3}\right]e^{j(\omega t - k_1 x_1)} \tag{4}$$

$$\underline{u}_s = (0,1,0)\left[C_s e^{-\Gamma_s x_3} + D_s e^{\Gamma_s x_3}\right]e^{j(\omega t - k_1 x_1)} \tag{5}$$

$$\underline{u}_p = (0,1,0)\left[E_p e^{-j\Gamma_p x_3} + F_p e^{j\Gamma_p x_3}\right]e^{j(\omega t - k_1 x_1)} \tag{6}$$

where ω is the angular frequency and the wave vector is $k_l=(\omega/V)$ where V is the phase speed of the solution. A_l, B_l, C_s, D_s, E_p, F_p, are constants determined by the boundary conditions.
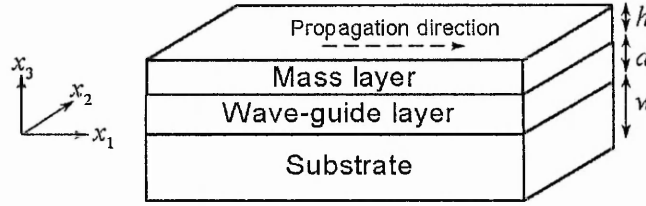
Figure B.1: Definition of axes and propagation direction for shear horizontally polarised waves in a three-layer system; the displacement is in the x_2 direction.

A traditional Love wave solution occurs when the substrate thickness w $\rightarrow\infty$, the shear speed of the substrate, $V_s = (\mu_s/\rho_s)^{1/2}$, is greater than the shear speed of the layer, $V_l = (\mu_l/\rho_l)^{1/2}$, and the wave vector Γ_s is real, so that the substrate displacement, $\underline{u}_s$, decays with depth. A traditional SH-APM solution occurs when w is finite, $d \rightarrow 0$ and the wave vector Γ_s is purely imaginary, so that the solution, $\underline{u}_s$, may take on a standing wave (resonant) form. In the more general case under consideration here, both Γ_l and Γ_s may be complex rather than real and no restriction to real is placed upon Γ_p. The use of the exponentials with a j factor in Eq. (4) and without a j factor in Eq. (5) is therefore purely to enable the similarity with the Love wave theory to be more readily noted. The choice of the exponential with a j factor in Eq. (6) is to emphasise the notational similarity with the guiding layer. One particularly simple limit of the theory is to regard the perturbing mass layer as nothing more than an extension of the guiding layer itself, by setting the material properties to the same values.

Substituting Eq. (4) into the equation of motion describing the layers, i.e. Eq. (1) with the relevant layer parameters, gives the equations for the wave vectors Γ_s, Γ_l, and Γ_p,

---

$$\Gamma_s^2 = \omega^2 \left(\frac{1}{V^2} - \frac{1}{V_s^2} \right) \tag{7}$$

$$\Gamma_l^2 = \omega^2 \left(\frac{1}{V_l^2} - \frac{1}{V^2} \right) \tag{8}$$

$$\Gamma_p^2 = \omega^2 \left(\frac{1}{V_p^2} - \frac{1}{V^2} \right) \tag{9}$$

To completely specify the problem the boundary conditions are imposed and this defines the constants A_l, B_l, C_s, D_s, E_p and F_p in Eqs. (4)–(6). The first type of boundary condition is continuity of the displacements at the interfaces between the layers and these give,

$$A_l + B_l = C_s + D_s \tag{10}$$

$$A_l \exp(-j\Gamma_l d) + B_l \exp(j\Gamma_l d) = E_p \exp(-j\Gamma_p d) + F_p \exp(j\Gamma_p d) \tag{11}$$

The remaining conditions all relate to the T_{i3} component of the stress tensor, which for this system using the form of the solutions in Eqs. (4)-(6) can be written as,

$$T_{i3} = \delta_{i2} \mu \left(\frac{\partial u_2}{\partial x_3} \right) \tag{12}$$

The second type of boundary condition, continuity of T_{i3} at the substrate-layer interface, gives,

$$-A_l + B_l = j(C_s - D_s)\xi \tag{13}$$

and

$$-A_l \exp(-j\Gamma_l d) + B_l \exp(j\Gamma_l d) = [-E_p \exp(-j\Gamma_p d) + F_p \exp(j\Gamma_p d)]\xi_p \tag{14}$$

where ξ and ξ_p have been defined as,

$$\xi = \frac{\mu_s \Gamma_s}{\mu_l \Gamma_l} \qquad (15)$$

and

$$\xi_p = \frac{\mu_p \Gamma_p}{\mu_l \Gamma_l} \qquad (16)$$

The remaining two boundary conditions are vanishing of stress at the two free surfaces at $x_3 = (d+h)$ and $x_3 = -w$, and these give the equations,

$$E_p \exp(-j\Gamma_p(d+h)) - F_p \exp(j\Gamma_p(d+h)) = 0 \qquad (17)$$

and

$$C_s \exp(\Gamma_s w) - B_s \exp(-\Gamma_s w) = 0 \qquad (18)$$

The six boundary conditions, Eqs (10), (11), (13), (14), (17) and (18) define both a dispersion equation and the coefficients, A_l, B_l, C_s, D_s, E_p and F_p in the solutions for the displacements. After extensive algebraic manipulation we find the dispersion equation,

$$\tan(\Gamma_l d) = \xi \tanh(\Gamma_s w) - \xi_p \tan(\Gamma_p h)[1 + \xi \tan(\Gamma_l d)\tanh(\Gamma_s w)] \qquad (19)$$

The second term on the right hand side of Eq. (19), which involves $\xi_p \tan(\Gamma_p h)$, is due to the presence of the third, perturbing, mass layer. Setting the thickness, h, of the perturbing mass layer to zero recovers the dispersion equation for the two-layer system of a substrate with a guiding layer. When the substrate thickness $w \rightarrow \infty$ with Γ_s real, so that the $\tanh(\Gamma_s w) \rightarrow 1$, Eq. (19) gives the limit of a traditional Love wave perturbed by an arbitrary thickness

perturbing mass layer. The layer guided SH-APM's correspond to $\Gamma_s=jk_s$ where k_s is real.

B.2 Perturbation Theory

When operated as a sensor, a Love wave device has a finite thickness wave-guiding layer; it is the finite thickness, which is responsible for the high mass sensitivity. The presence of a finite thickness wave-guiding layer means that the wave speed for the Love waves is smaller than the substrate shear speed. Similarly, the wave speed for the layer guided SH-APM's are larger than the substrate shear speed. A third, thin perturbing, mass layer therefore acts about a particular operating point on the dispersion curve of the bare, two-layer, system defined by,

$$\tan(\Gamma_l^o d)=\xi_o\tanh(\Gamma_s^o w) \qquad (20)$$

where the superscripts on Γ_l^o and Γ_s^o indicate the wavevectors in Eqs (7)-(9) are given by a solution to Eq. (20) for $V=V_o\neq V_s$; the superscript on ξ^o indicates that Γ_l^o and Γ_s^o are used in Eq. (15). The solutions for this system have been discussed in detail in a previous report; it should be noted that the limit of a vanishing wave-guiding layer has to be handled carefully as this involves the conversion from layer guided acoustic plate modes with an imaginary wave-vector to Love waves with a real wave-vector.

Consider a perturbing third mass layer of thickness, $h=\Delta h$. This perturbation of the two-layer system will result in a decrease in the phase speed of the mode, irrespective of whether that mode is a Love wave or a layer guided SH-APM. The perturbation will cause changes in the phase speeds and the wave-vectors of the substrate and guiding layers and we can therefore write $\Gamma_l^o \to \Gamma_l^o+\Delta\Gamma_l$, $\Gamma_s^o \to \Gamma_s^o+\Delta\Gamma_s$ and $\xi^o\to\xi^o+\Delta\xi$ where the superscript zero indicates the values of the quantities when $\Delta h=0$ (i.e. solutions of Eq. (20)). The left hand side of the three-layer dispersion equation (Eq. (19)) can then be written,

$$\tan(\Gamma_l d)=\frac{\tan(\Gamma_l^o d)+\tan(\Delta\Gamma_l d)}{1-\tanh(\Gamma_l^o d)\tan(\Delta\Gamma_l d)} \tag{21}$$

The first term on the right hand side of the three-layer dispersion equation (Eq. (19)) can be written,

$$\xi\tanh(\Gamma_s w)=(\xi+\Delta\xi)\left[\frac{\tanh(\Gamma_s^o w)+\tanh(\Delta\Gamma_s w)}{1+\tanh(\Gamma_s^o w)\tanh(\Delta\Gamma_s w)}\right] \tag{22}$$

and the second term can be written to first order as,

$$\xi_p\tan(\Gamma_p h)\left[1+\xi\tan(\Gamma_l d)\tanh(\Gamma_s w)\right]\approx\xi_\beta\Gamma_\beta\Delta h\left[1+\xi_o\tan(\Gamma_l^o d)\tanh(\Gamma_s^o w)\right] \tag{23}$$

The expansion in $\Delta\xi$ can be written in terms of $\Delta\Gamma_l$ and $\Delta\Gamma_s$ using Eq. (15) and both of these quantities can be related to the change, ΔV, in the wave speed, V_o, using Eqs. (7) and (8). Performing these manipulations and grouping terms, we find that Eq. (19) gives the perturbation formula,

$$\frac{\Delta V}{V_o}\approx\left(1-\frac{V_p^2}{V_o^2}\right)\rho_p g(\omega,V_s,\rho_l,V_l,w,d)\Delta h \tag{24}$$

where the function g, is defined as,

$$g(\omega,v_s,\rho_l,V_l,w,d)=\frac{\frac{-\omega_2}{\rho_l\Gamma_l^o V_l^2}\left[1+\tan_2(\Gamma_l^o d)\right]}{\frac{\Gamma_l^o d}{\left(\frac{V_o^2}{V_l^2}-1\right)}\left[1+\tan_2(\Gamma_l^o d)\right]+\frac{\Gamma_s^o w}{\left(1-\frac{V_o^2}{V_s^2}\right)}\left[1-\tanh_2(\Gamma_s^o w)\right]+\tan(\Gamma_l^o d)\left[\frac{1}{\left(\frac{V_o^2}{V_l^2}-1\right)}+\xi_o\frac{1}{\left(1-\frac{V_o^2}{V_s^2}\right)}\right]} \tag{25}$$

This function g depends only on the operating frequency and properties of the substrate and wave-guiding layer. These formulae are only valid for perturbations about an operating point on the two-layer dispersion curve that

satisfies $V_o \neq V_s$ and $V_o \neq V_l$; It should be noted that due to the frequency dependence of Γ_l^o and Γ_s^o in the function, g, Eq. (24) does not, in general, predict a frequency-squared dependence for the fractional shift in phase speed. The function g determines the mass sensitivity of the sensor device,

$$\frac{\Delta V}{V_o} \approx -\frac{V_o}{4}\left(1 - \frac{V_p^2}{V_o^2}\right)\rho_p |U_2|^2 \Delta h \tag{26}$$

where U_2 is the normalized particle velocity displacement at the surface. The combination, $\rho_p \Delta h$, of the density and thickness of the perturbing mass layer gives the mass per unit surface area, Δm, and we can therefore re-write Eq. (24) as,

$$\frac{\Delta V}{V_o} \approx \left(1 - \frac{V_p^2}{V_o^2}\right)g(\omega, V_s, \rho_l, V_l, w, d)\Delta m \tag{27}$$

B.3 Mass Sensitivity from the Device Dispersion Curve

Experimentally, the significance of Eq. (24) and (25) is that if we can determine the sensitivity function, g, for any perturbing layer, then it is the same function for any other perturbing mass layer. Now consider a two-layer system and imagine creating a thin third layer of the same material as the wave-guiding layer. Writing $x=d$ and $\Delta h = \Delta x$, Eq. (24) becomes,

$$\frac{\Delta V}{V_o} \approx g(\omega, V_s, \rho_l, V_l, w, d)\left(1 - \frac{V_l^2}{V_o^2}\right)\rho_l \Delta x \tag{28}$$

where the subscript zero indicates the value of the phase speed at a thickness $x=d$. Making the third layer infinitesimally thin we may write the function, g, as,

$$g(\omega, V_s, \rho_l, V_l, w, d) = \frac{1}{V_o \rho_l (1 - V_l^2/V_o^2)} \left(\frac{dV}{dx} \right)_{x=d} \tag{29}$$

Thus, the sensitivity function involves the slope of the phase velocity dispersion curve with guiding layer thickness at the guiding layer thickness operating point. Using Eq. (29) we may simplify Eq (24) to,

$$\frac{\Delta V}{V_o} \approx \frac{\rho_p}{\rho_l} \left[\frac{1 - V_p^2/V_o^2}{1 - V_l^2/V_o^2} \right] \frac{1}{V_o} \left(\frac{dV}{dx} \right)_{x=d} \Delta h \tag{30}$$

and this may be further simplified if $V_p^2 << V_o^2$ and $V_l^2 << V_o^2$. Eq. (30) can be re-written using the perturbing mass $\Delta m = \rho_p \Delta h$. Equation (30) should be of particular use in developing wave-guide based acoustic wave sensors, because it enables the mass sensitivity of a prospective device to be assessed directly from the dispersion curve. Moreover, this dispersion curve can be determined either numerically or from experimentation by systematically increasing the thickness of the wave-guide layer. Whilst arguments based on perturbation theory have been used in deriving Eq. (30), the formula itself is for a perturbation on top of a wave-guide layer of arbitrary thickness rather than of a vanishing thickness. Defining a mass sensitivity function, S_m, we can write,

$$S_m = \lim_{\Delta m \to 0} \frac{1}{\Delta m} \left(\frac{\Delta V}{V_o} \right) = \frac{1}{\rho_l} \left[\frac{1 - V_p^2/V_o^2}{1 - V_l^2/V_o^2} \right] \frac{1}{v_o} \left(\frac{dV}{dx} \right)_{x=d} \tag{31}$$

or,

$$S_m = \frac{1}{\rho_l} \left[\frac{1 - V_p^2/V_o^2}{1 - V_l^2/V_o^2} \right] \left(\frac{d \log_e V}{dx} \right)_{x=d} \tag{32}$$

where the mass sensitivity function, S_m, is in units of $m^2 \, kg^{-1}$. Thus, the mass sensitivity of a Love wave or a layer-guided shear horizontally polarized acoustic plate mode device can be determined numerically from the dispersion curve. Whilst a relationship between the maximum slope in a dispersion curve and the maximum mass sensitivity for surface acoustic wave sensors has been remarked upon by some researchers, Eq. (32) gives it an explicit theoretical basis for Love waves and layer guided SH-APMs.

B.4 Mass Sensitivity and Frequency Dependence

In a two-layer system with a finite thickness substrate and finite thickness wave-guiding layer, the frequency enters the calculation of the wave-speed, V_o, through the two dimensionless combinations $d/\lambda_l = df/V_l$ and $w/\lambda_s = wf/V_s$. When the substrate is infinitely thick the layer guided plate modes are no longer possible and only Love waves can exist. Moreover, on such an infinite thickness substrate the phase speed for a Love wave depends on frequency only through the dimensionless combination of $z = d/\lambda_l = df/V_l$, so that a change in guiding-layer thickness, d, is equivalent to a change in operating frequency, f. Thus, Eq. (32) (or Eq. (31)) can be used to assess the change in sensitivity that will occur through a change in operating frequency, for a given mass perturbation, Δm, on a particular device. The dispersion curve can be plotted using the dimensionless variable, z, and the slope on this dispersion curve can be related to the slope in the dispersion curve when plotted against guiding layer thickness,

$$\left(\frac{dV}{dx}\right)_{x=x_0} = \frac{f_o}{V_l}\left(\frac{dV}{dz}\right)_{z=z_0} \qquad (33)$$

where the subscript o implies the values of the various quantities at the operating point of the dispersion curve. The mass sensitivity function, Eq. (32), then becomes,

$$S_m = \frac{1}{\rho_l}\left[\frac{1-V_p^2/V_o^2}{1-V_l^2/V_o^2}\right]\frac{f_o}{V_l}\left(\frac{d\log_e V}{dz}\right)_{z=z_0}$$ (34)

From Eq. (34), the mass sensitivity, S_2, at a frequency f_2 compared to the mass sensitivity, S_1, at a frequency f_1, is given by,

$$S_2 = \left[\frac{1-V_p^2/V_2^2}{1-V_p^2/V_1^2}\right]\left[\frac{1-V_l^2/V_1^2}{1-V_l^2/V_2^2}\right]\left[\frac{f_2}{f_1}\right]\left[\frac{\left(\frac{d\log_e V}{dz}\right)_{z=z_2}}{\left(\frac{d\log_e V}{dz}\right)_{z=z_1}}\right]S_1$$ (35)

It should be noted that Eq. (35) is valid whether or not the change in frequency leads to a Love wave of the same mode. In a harmonic type device design the frequency change would typically be a doubling or trebling and could therefore involve a change of Love wave mode.

APPENDIX C

APPENDIX C

LOVE WAVE LIQUID SENSING BY USING HIGH MOLECULAR WEIGHT PEG SOLUTIONS

Appendix C shows the liquid sensing data for the PEG with a molecular weight of 10000 and 20000. Those data include changes in insertion loss and fractional changes in phase velocity derived from phase changes, with respect to the density and viscosity of the solutions.
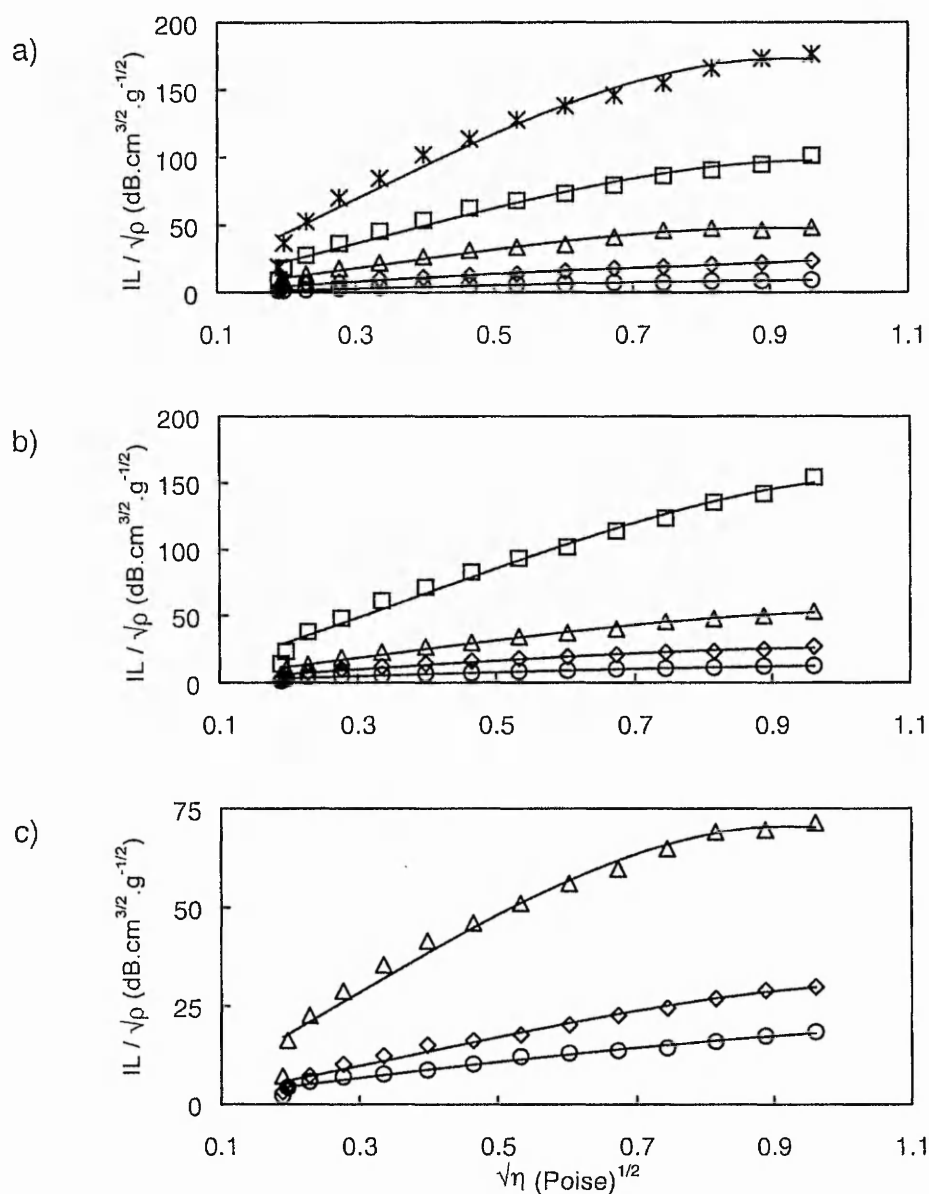
Fig. C1   Change in insertion loss from water normalized to the square root of the solutions density versus the square root of the solutions viscosity at the a) first, b) second and c) third Love mode with increasing z. a) circles:0, diamonds: 0.006, triangles: 0.013, squares: 0.02, starts: 0.027; b) circles: 0.106, diamonds: 0.113, triangles: 0.12, squares: 0.127; c) circles: 0.213, diamonds: 0.22, triangles: 0.227- by using PEG 10000.
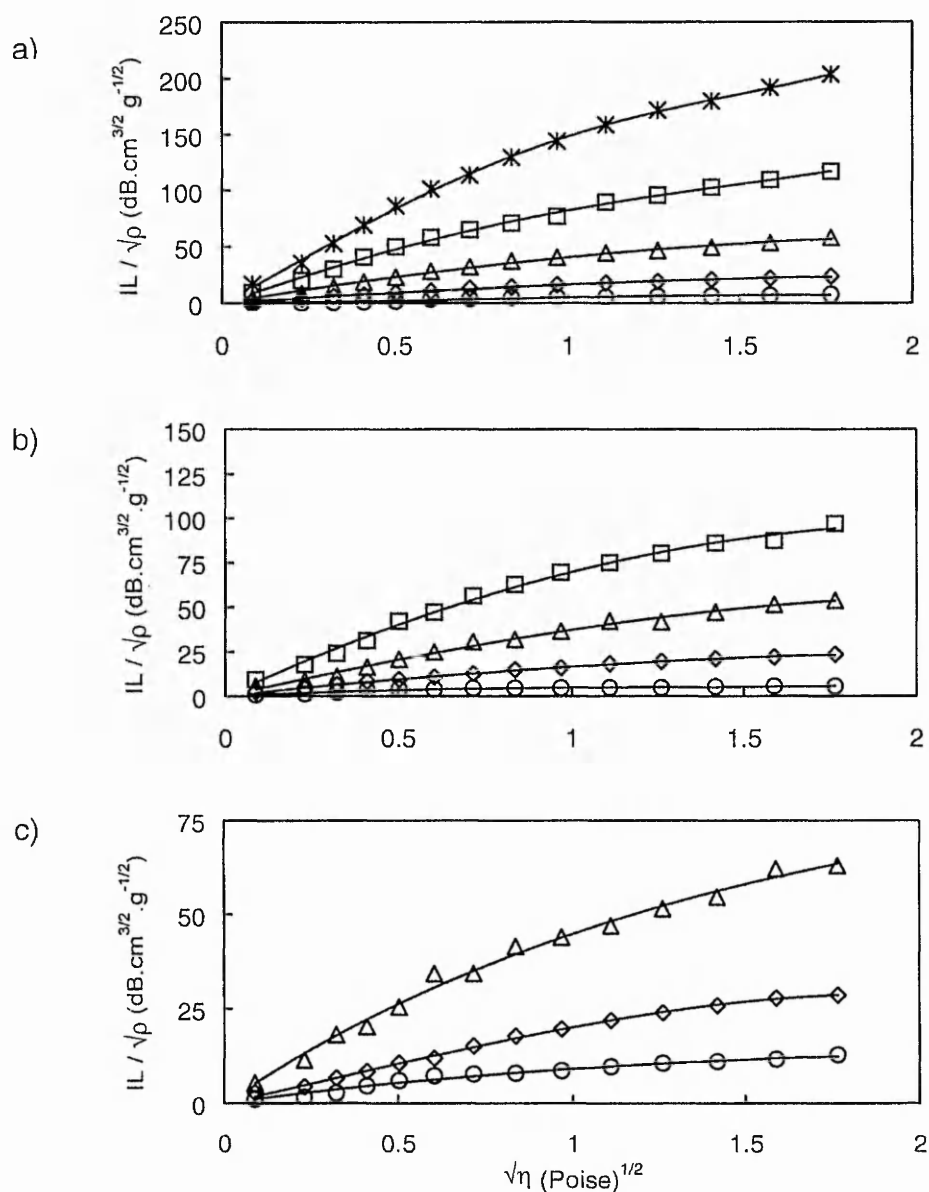
Fig. C2   Change in insertion loss from water normalized to the square root of the solutions density versus the square root of the solutions viscosity at the a) first, b) second and c) third Love mode with increasing z. a) circles:0, diamonds: 0.006, triangles: 0.013, squares: 0.02, stars: 0.027; b) circles: 0.106, diamonds: 0.113, triangles: 0.12, squares: 0.127; c) circles: 0.213, diamonds: 0.22, triangles: 0.227- by using PEG 20000.
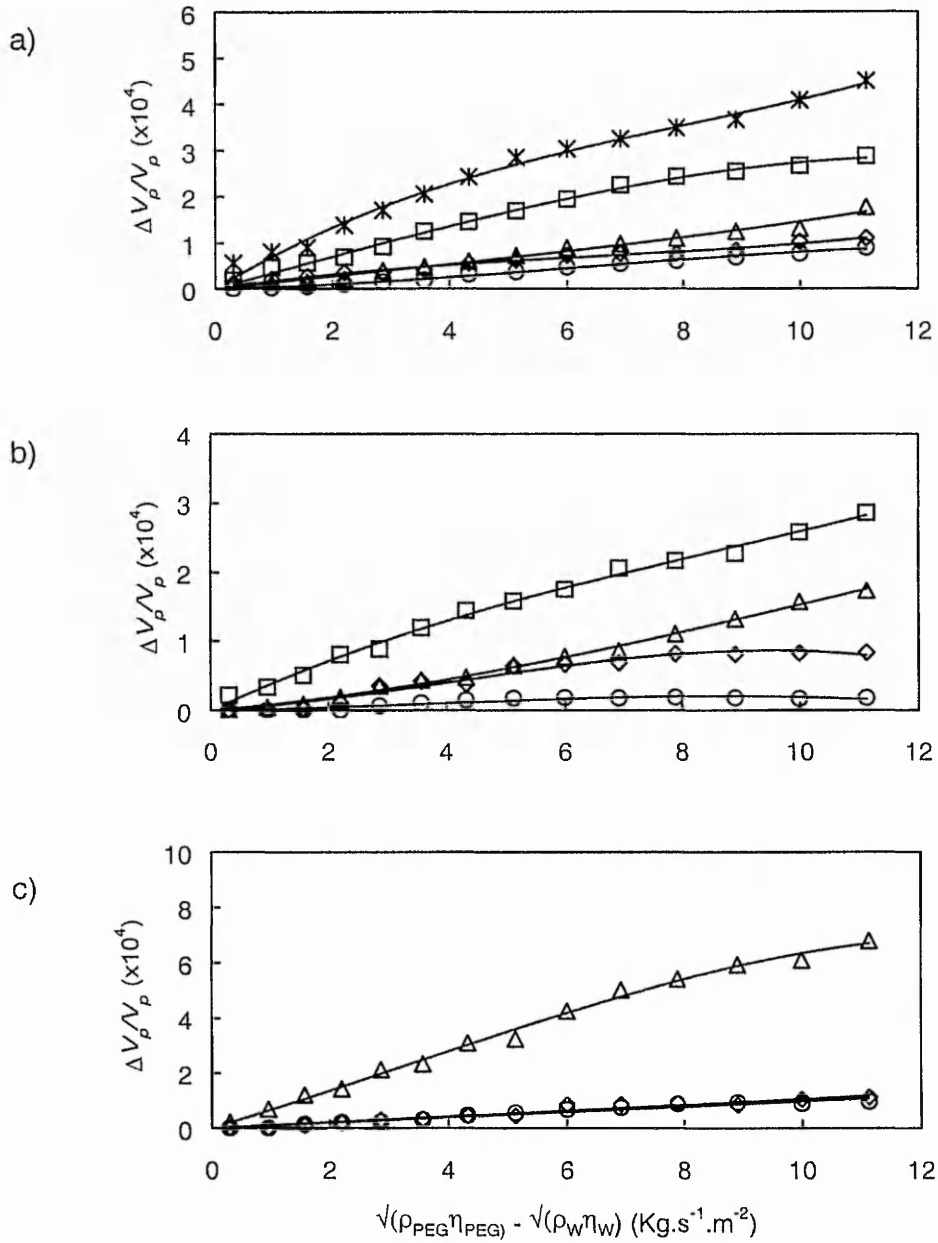
Fig. C3   Fractional change in phase velocity versus the difference between the density-viscosity product of the PEG and the water for the a) first, b) second and c) third Love mode with increasing z. a) circles:0, diamonds: 0.006, triangles: 0.013, squares: 0.02, starts: 0.027; b) circles: 0.106, diamonds: 0.113, triangles: 0.12, squares: 0.127; c) circles: 0.213, diamonds: 0.22, triangles: 0.227- by using PEG 10000.
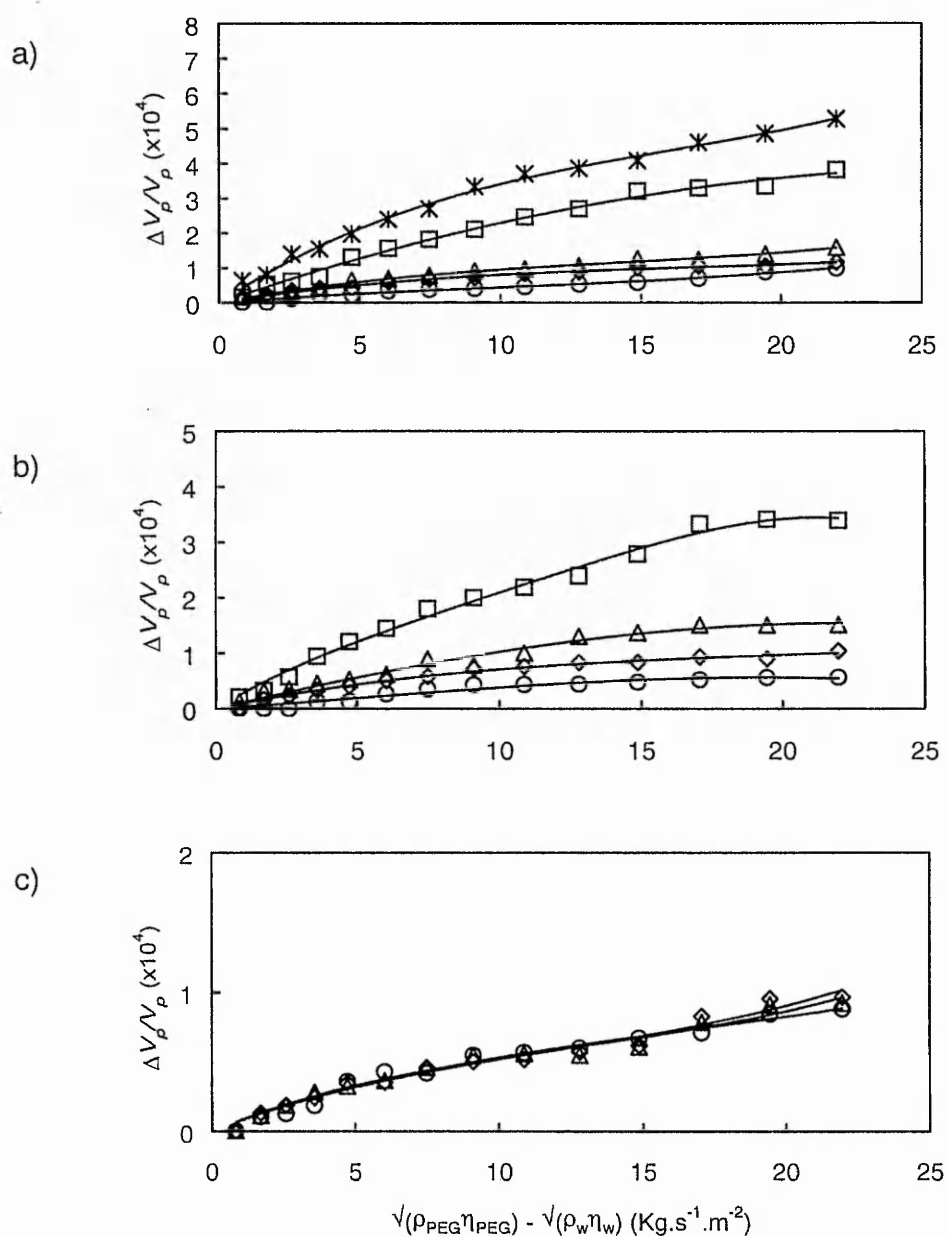
Fig. C4 Fractional change in phase velocity versus the difference between the density-viscosity product of the PEG and the water for the a) first, b) second and c) third Love mode with increasing z. a) circles:0, diamonds: 0.006, triangles: 0.013, squares: 0.02, starts: 0.027; b) circles: 0.106, diamonds: 0.113, triangles: 0.12, squares: 0.127; c) circles: 0.213, diamonds: 0.22, triangles: 0.227- by using PEG 20000.

Parts of this thesis have been published elsewhere:

"Harmonic Love wave devices for bio sensing applications", M.I Newton, F. Martin, K. Melzak, E. Gizeli and G. McHale, Electronics Letters, 2001, **37** (6), 340-341.

"Pulse mode operation of Love wave devices for bio sensing applications", M.I Newton, G. McHale, F. Martin, E. Gizeli and K. Melzak, The Analyst, 2001, 2107-2109.

"Resonant conditions for Love wave guiding layer thickness", G. McHale, M.I Newton, F. Martin, K. Melzak and E. Gizeli, Applied Physics Letters, 2002, **79** (23).

"Generalised Love waves", M.I Newton, G. McHale, F. Martin, E. Gizeli and K. Melzak, European Physics Letters, 2002, **58** (6), 818-822.

"Layer guided shear horizontally polarised acoustic plate modes", M.I Newton, G. McHale and F. Martin, Journal of Applied Physics, 2002, **91**, 5735-5744.

"Theoretical mass sensitivity in Love wave and layer guided shear horizontally polarised acoustic plate mode sensors", G. McHale, M.I Newton and F. Martin, Journal of Applied Physics, 2002, **91**, 9701-9712.

"Acoustic Determination of polymer molecular weights and rotation times", K. Melzak, F. Martin, M.I Newton, G. McHale and E. Gizeli, Journal of Polymer (B), 2002, **40** (14), 1490-1495.

"Propagation characteristics of harmonic surface skimming bulk waves on ST quartz", F. Martin, Electronics Letters, 2002, **38** (16), 941-942.

"Mass sensitivity of acoustic wave devices from group and phase velocity measurements", G. McHale, F. Martin and M.I Newton, Journal of Applied Physics, 2002, **92** (6), 3368-3373.

"Theoretical mass, liquid and polymer sensitivity of acoustic wave sensors with viscoelastic guiding layers", G. McHale, M. I. Newton, F. Martin, Journal of Applied Physics, 2003, **93** (1), 675-690.

"Pulse mode of SH-SAW system for biosensing applications", F. Martin, M. I. Newton, G. McHale, E. Gizeli, K. A. Melzak, Biosensors and Bioelectronics (Submitted Dec 2002).

"Experimental study of Love wave mass sensitivity by phase and group velocity measurements", F. Martin, G. McHale, M. I. Newton, IEEE sensors journal (Submitted July 2002).

"Love wave and layer guided shear horizontal acoustic plate mode sensors", G. McHale, M. I. Newton and F. Martin, Institute of Acoustics Spring Conference (2002), ISBN 1 90 1656 45 4/ISSN 0309-8117, Vol. 24, Part 2 (2002).

"Layer guided shear horizontal acoustic plate mode sensors", G. McHale, M. I. Newton, F. Martin, UFFC-FC Proceeding, New Orleans USA, May 2002.

"Layer guided shear acoustic plate mode sensor", M. I. Newton, G. McHale, F. Martin, Applied Physics Letters (Submitted Nov. 2002).